A STUDY OF THE GAMMA-RAYS ASSOCIATED

WITH THE INELASTIC SCATTERING OF NEUTRONS

by

Kathleen Allenby, B.Sc. (Physics)

Thesis submitted for the degree of Doctor of Philosophy,

in the Department of Physics,

University of Aston in Birmingham.

September, 1974.

ABSTRACT

An experimental spectrometer, capable of measuring differ-
ential cross-sections for production of gamma-rays from neutron
inelastic scattering, was available at the start of the project.
14 MeV neutrons were produced by the $T(d,n)He^4$ reaction. The
gamma-rays were detected by a heavily shielded NaI scintillator.
Time of flight discrimination, using the associated particle
technique, was used to eliminate background due to scattered
neutrons. The performance of this system was improved, by
achieving better time and energy resolution, resulting in an
increase in sensitivity of the system by a factor of 10. The
new system was then used to measure the differential cross-
sections for production of the 1·37 MeV gamma-ray from Mg^{24},
the 1·43 MeV gamma-ray from Cr^{52}, and the 0·84 MeV gamma-ray
from Fe^{56}, in the range of scattering angle 0° to 90°.

The direct interaction theory, in the form of the coupled
channels approximation, was used to predict these angular dis-
tributions. The programme INCH, written by A. D. Hill of Oxford,
was used in this work. This programme predicts the neutron
elastic and inelastic scattering differential cross-sections,
and was modified by the addition of a subroutine GAMMA, to cal-
culate the gamma-ray angular distributions. This was done by
finding the correlation function between gamma-rays and scattered
neutrons, and averaging over the neutron scattering angle. The
theoretical predictions were then compared with the experimental
results.

ACKNOWLEDGEMENTS

CONTENTS

5. EXPERIMENTAL AND THEORETICAL RESULTS

1. INTRODUCTION

The neutron, with its lack of electric charge, has been found to be a very powerful probe for the investigation of nuclear properties and forces. Without the complications of the Coulomb interaction, the calculations are simplified, and the absence of the Coulomb barrier means that neutrons of very low energy can take part in nuclear interactions.

One of the predominant modes of neutron interaction with nuclei in the range of incident energy 1 - 50 MeV is elastic or inelastic scattering. Elastic scattering does not affect the internal state of the nucleus but simply transfers momentum to the nucleus as a whole, in the laboratory system. Inelastic scattering involves the excitation of one of the higher states of the nucleus, and consequent loss to the emerging neutron of the corresponding amount of energy. The nucleus is thus left in an excited, and therefore unstable state. In some cases, decay by particle emission occurs, but the most common mode of de-excitation is by gamma-ray emission. The study of these gamma-rays provides a means of investigating the nuclear interactions and the structure of the nucleus.

At incident neutron energies of less than about 10 MeV, the neutron interactions with nuclei have been described by the compound nucleus theory first proposed by Bohr [1]. This theory describes the reaction as taking place in two distinct stages, the first of which is the formation of a compound system which survives long enough to be considered as a separate entity (10^{-16} - 10^{-18} sec). During this stage, the energy of the incident neutron and its binding energy is shared between all the nucleons by a series of

multiple collisions resulting in high excitation of the compound
system. Due to continued collisions, eventually all or part of
the incident energy is concentrated in a particle near the nuclear
surface, and this "evaporates". The compound system thus decays
by the emission of the particle concerned. It is assumed that the
probability of decay in a particular mode, or channel, does not
depend on the way the compound system was formed, but only on the
properties such as the spin and parity, of the compound system.
This theory has been found on many occasions to yield good fits
to experimental data [2 - 3]. For example, it is able to account
for the large capture cross-sections and narrowly spaced reson-
ances shown by nuclei under bombardment by neutrons of a few
MeV.

Considering the gamma-rays emitted in neutron inelastic
scattering, the shapes and anisotropies of the gamma-ray angular
distributions have a strong dependence on the properties of the
relevent nuclear levels, namely, the spin, parity and branching
ratios. It is thus possible in many cases to obtain unambiguous
values of these quantities by comparing experimental measurements
of angular distributions with theoretical predictions. For example,
Benjamin et al [4] have found the spin and parities of the levels
of the isotope Fe^{56}.

The compound nucleus theory, however, does not provide an
explanation of the diffraction structure, including strong forward
peaking, found experimentally for nucleon scattering at energies
as low as 6 MeV [5].

This phenomenon suggests the occurance of direct interactions,
which are assumed to take place within the time period taken by the

neutron to traverse the nucleus ($\sim 10^{-21}$ sec). There is thus no intermediate state formed. Direct interaction theory has successfully accounted for nucleon scattering at energies of 10 MeV and above. Due to the scarcity of experimental neutron data theoretical interest has first centred on proton work. Here the theory produces acceptable fits to experimentally measured angular distributions and polarizations of elastically and inelastically scattered medium energy protons [6 - 10]. The fits to the available neutron data are also good [6, 11, 12].

As mentioned above, work at lower incident neutron energies has been published on gamma-rays produced by neutron inelastic scattering. Compound nucleus theory has been used to predict the gamma-ray angular distributions. This work has been reviewed by Sheldon and Van Patter [13]. Up to the present time, however, no work on fitting the gamma-ray angular distributions produced by nucleon inelastic scattering at higher nucleon incident energies is known. It is therefore interesting to investigate the possibility of predicting gamma-ray angular distributions using direct reaction theory. If successful, this would provide an independent confirmation of the nucleon scattering results, which test the theoretical description of the reaction mechanism. This is one of the aims of the present work.

In the range of incident nucleon energy 10 to 20 MeV, it is uncertain which mechanism is dominant, and the reaction may possibly be best expressed as a mixture of the two [14]. 14 MeV, the incident neutron energy used in this work, is thus an interesting value at which to test the reaction mechanism. It is believed that the actual mechanism of the interaction is described exactly by neither of these theories, but rather that both are simplifi-

cations which concentrate on one aspect of the whole at the expense
of the rest. In recent years some progress has been made in deriving
a "unified" theory [15] in which both compound nucleus formation
and direct interaction appear as extreme cases although this theory
has not been used here.

Some work on the gamma-rays produced by 14 MeV neutron
reactions has been published. Investigation of the gamma-ray
spectra has been used to determine nuclear energy levels, and in
some cases, the parity of these levels [16]. Experimental measure-
ments of gamma-ray angular distributions have been made, [17 - 21]
and many measurements of the differential cross-section at 90°
have been published [22 - 24]. Since the measured angular dis-
tributions are usually anisotropic, it is not valid, as some
workers have done [25], to integrate the differential cross-section
measured at one angle, to obtain the total cross-section. Instead,
the whole distribution must be measured. Theoretical predictions
of the angular distributions, when compared with experiment, may
yield further information, but the extent of this must depend on
the accuracy with which the experimental data can be obtained.

This consideration leads to the first part of the research
project. An experimental spectrometer has been reported [17], and
was available to measure gamma-ray energy spectra produced at
various scattering angles by inelastic scattering of 14 MeV neutrons
produced by the d, T reaction. Time of flight discrimination was
used to separate gamma-rays from scattered neutrons, using the
associated particle technique. The gamma-rays were detected by a
NaI scintillator crystal. Detection of the associated alpha-
particles gave a measure of the incident neutron flux, so the
differential cross-sections for gamma-ray production could be

calculated.

The performance of the system was thus limited by both the time resolution and energy resolution available. For example measurement of a differential cross-section of the order of 50 mb/str. required approximately 20 hours machine time, and was achieved with an accuracy of the order of ± 13%. This was inferior to the performance reported by others, for example Stewart and Martin report an accuracy of about 10% [18].

Improvements in the available technology since the initial design meant that the system could probably be improved. For example, the time resolution, measured as the full width at half maximum of the gamma-ray peak in the time spectrum, was approximately 13 nsec, the exact value depending on experimental circumstances. This comparatively high figure (Stewart and Martin [18] report 8 nsec) was caused by the difficulty in obtaining good timing information from the NaI scintillator used to detect the gamma-rays. Reports have been published [26] which showed that, using a technique known as constant fraction discrimination, the time resolution obtainable from various scintillators was much improved over that obtained with conventional techniques. Improvements were thus possible to the system, and part of the work described here consisted of introducing them.

The new system was then used to measure the differential cross-sections for gamma-ray production for various elements, namely, magnesium, chromium, and iron. The criterion used to chose these elements was the lack of corroborated published measurements. In the case of chromium, there were no published results on measurements of angular distributions of gamma-rays,

at the beginning of the research project. The differential cross-sections of the 1·37 MeV gamma-ray from Mg^{24}, and the 0·85 MeV gamma-ray from Fe^{56} have been published by Martin and Stewart [18, 21]. The relative angular distribution of the 1·37 MeV gamma-ray from Mg^{24} has been published by Benetskii [19, 20], but the absolute value of the cross-section is not given. Values for the differential cross-section at 90° a quantity frequently measured, range between 26·2 ± 6·5 mb/str. [22] and 40·1 ± 3·9 mb/str. [21] for the 1·37 MeV gamma-ray of Mg^{24}, and between 30·2 ± 9·1 mb/str. [22] and 79·2 ± 9·4 mb/str. [21] for the 0·85 MeV gamma-ray from Fe^{56}. Since these values are not compatible within the experimental errors, it was thought worthwhile to repeat the measurements with the system capable of greater accuracy. From the theoretical point of view, the most abundant isotopes of these elements are all even-even nuclei, with 0^{+} ground states and 2^{+} first excited states. The treatment of the transitions between these two states is thus similar in each case.

The second phase of the work was then to calculate the angular distributions of the gamma-rays produced by inelastic scattering of neutrons on these nuclei, using the predictions of direct interaction theory. For this work, a coupled channels program, INCH, written by A. D. Hill of Oxford, was used. This program, which dealt with nucleon scattering, was modified to include a subroutine GAMMA, which calculates the gamma-ray angular distributions. These could then be compared with the experimental data, providing a test, both of the reaction mechanism and nuclear models assumed in the calculation, and of the simplifying assumptions made in the course of the calculation.

2. THE EXPERIMENTAL SYSTEM

2.1. Introduction

In this chapter, the apparatus and experimental procedure will be described. Only a brief description of the whole system will be given, more emphasis being placed on changes that have been made to the original system. The spectrometer, which was in operation when the present work was begun, was capable of measuring differential cross-sections for gamma-ray production of the order of 50 mbarns/str. It was felt that certain improvements could be made, mainly in increasing energy and time resolution. This would then enable, either cross-sections of this order to be measured more quickly, or smaller cross-sections to be measured in the same time as before. As will be shown, this has now been achieved. A complete description of the original system has been reported [17].

2.2. Brief Description of System

Neutrons of approximately 14 MeV are produced by the $T(d,n)$ He^4 reaction. Alpha-particles emerging at $90° \pm 6°$ to the deuteron beam are detected, thus defining a cone of associated neutrons at $83° \pm 6°$ to the deuteron beam, (figure 2.1).

The scattering sample, in the form of a rectangular plate, is placed so that it completely subtends the neutron cone. The sample thickness is such that 30% of the incident neutrons interact.

Neutron inelastic scattering events in the sample result in the emission of gamma-rays. These are detected by a 77 mm x 77 mm (3" x 3"). NaI crystal scintillator and 58 AVP photomultiplier. The gamma-ray detector is mounted 0·78 m from the scattering sample.
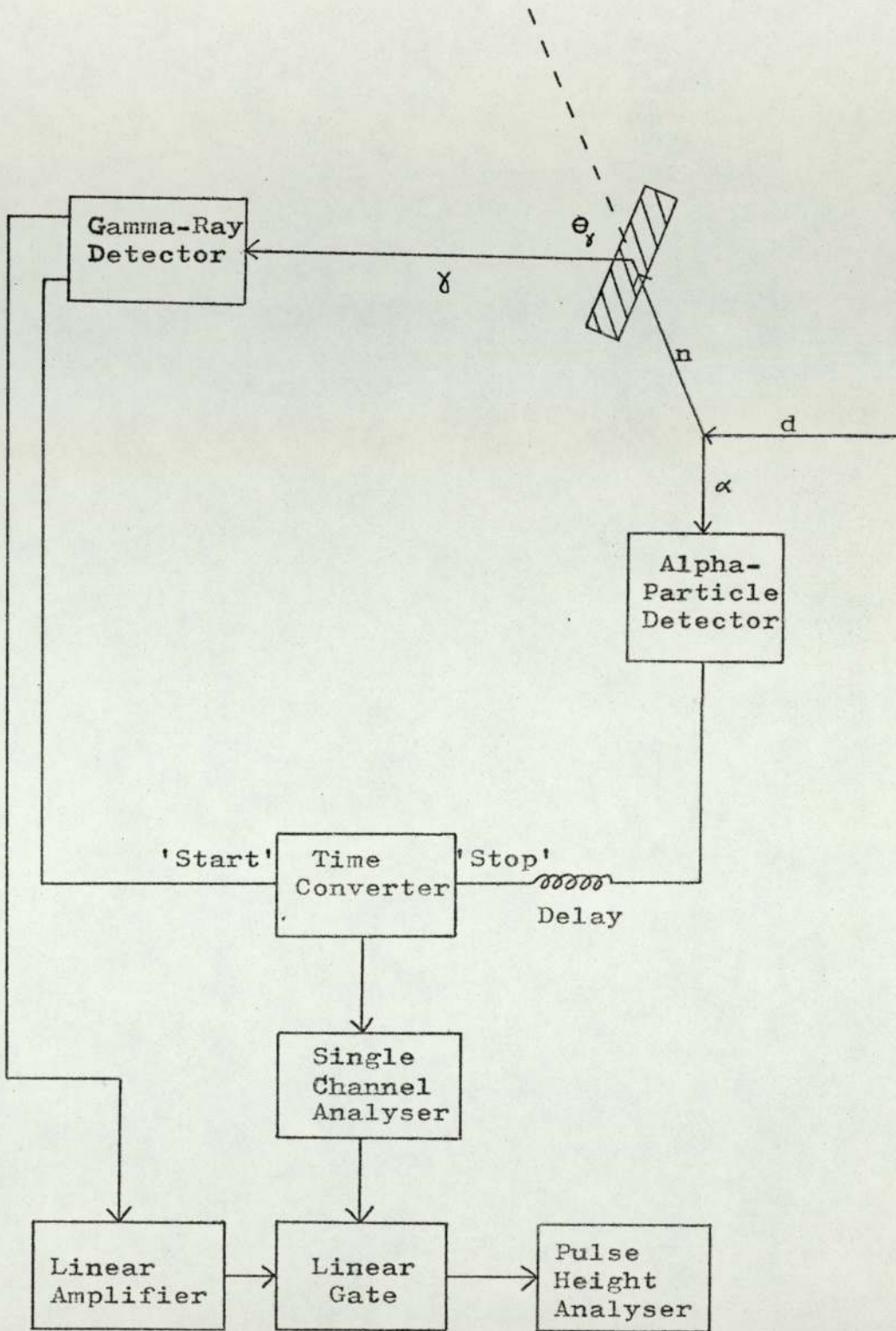
Figure 2.1   Schematic View of the Experimental
            System.

and is moveable so that measurements can be taken at scattering angles in the range 0° to 90° to the neutron beam direction, in the horizontal plane.

The NaI crystal is sensitive to neutrons as well as to gamma-rays, so time-of-flight discrimination is used to eliminate pulses due to the detection of neutrons. A pulse from the gamma-ray detector starts the time-converter, which is then stopped by a delayed pulse from the alpha-detector, producing an output pulse with height proportional to the time delay between the "start" and "stop" pulses. Since elastically scattered 14 MeV neutrons have a speed of about 0·17 C, and inelastically scattered neutrons less than this, their flight times from the sample to the detector are longer than the time taken by gamma-rays. This is the basis of the time of flight discrimination system. A single channel analyser is arranged to pass only those output pulses from the time converter which are due to gamma events, thus eliminating pulses due to neutrons scattered from the sample.

Another pulse is taken from the gamma-ray detector (figure 2.1), amplified, and passed to a linear gate which is opened by the single channel analyser output, thus allowing the gamma-ray pulses to be stored in a pulse-height analyser, forming an energy spectrum of the gamma-rays.

2.3. Neutron Production

Deuterons are obtained from an electrostatic accelerator (Type J) manufactured by the S.A.M.E.S.* Company, (figure 2.2). After acceleration to an energy of between 115 KeV and 150 KeV, the deuterons pass down a 6m. long evacuated beam tube to a
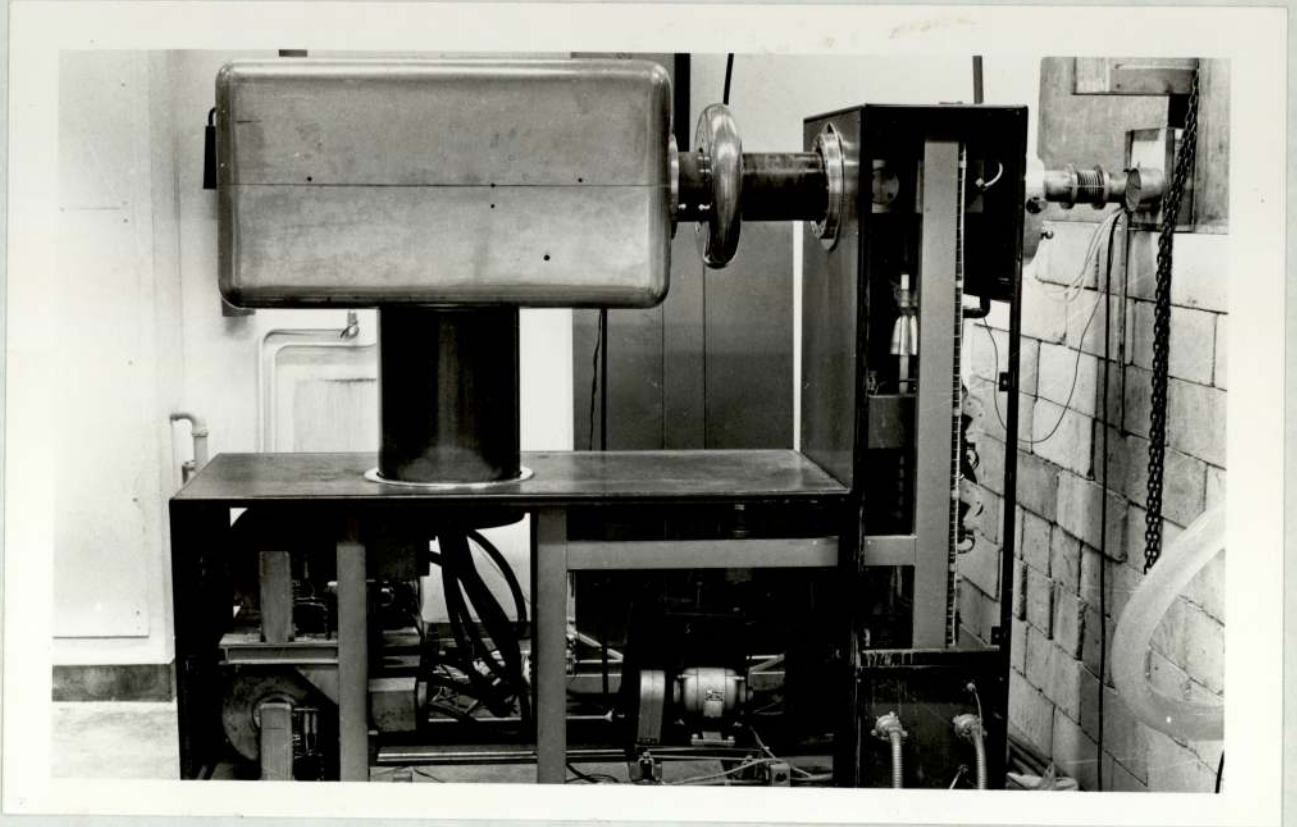
Figure 2.2   The S.A.M.E.S. Electrostatic Generator.

target of tritium adsorbed onto titanium. Because of the length
of the drift tube, the beam is focussed by two electrostatic
quadrupole lenses [27], in the horizontal and vertical planes,
and is directed on to the target by an electrostatic deflector
plate.

The beam incident on the target is defined by a vertical
slit, 10 mm x 1 mm, in a brass plate situated across the end of
the beam tube. This slit replaces a pin-hole which was used
previously, and results in a much increased neutron yield for the
same machine output. Machine instability had limited the neutron
yield to 3×10^7 sec^{-1}, but it is now possible to run at about
10^8 neutrons sec^{-1}. It is not possible to quantify this improve-
ment more accurately as the machine stability depends on several
factors such as ambient humidity and temperature which are not
controlled or monitored.

The target consists of a disc of titanium loaded with tritium,
contained in a stainless steel case, incorporating a water cooling
system**. Only a small part of the target is struck at any one
time by the deuteron beam, and the target can be rotated to expose
new areas to the deuterons.

2.4. The Alpha-Particle Detection System

Alpha-particles emitted in the range 84° to 96° to the
deuteron beam are detected by a plastic scintillator (NE 102A),

----

* Societe Anonyme de Machines Electrostatique.

** Supplied by Multivolt Ltd., Sussex.

0·5 mm thick. The sheet of scintillator is 30 mm square and
shielded from the alpha-particles by an aluminium plate, 1 mm
thick. An aperture in the plate, 10·9 mm x 18·9 mm, defines
a "beam" of alpha-particles which are detected, with half angles,
3·5° in the vertical plane and 6° in the horizontal plane. The
alpha-particle detector is 90 mm from the target. The scintil-
lator is optically coupled by a perspex light pipe 10 mm thick
to a Phillips 56 AVP photomultiplier, (figure 2.3). The light
pipe also forms a flange isolatingthe photomultiplier from the
vacuum system, and supports the scintillator sheet. The dynode
chain which supplies voltage to the dynodes of the photomultiplier
tube is shown in figure 2.4. Equal voltages are applied between
the dynodes, a design recommended by the manufacturers, for high
gain.

Since the range of the alpha particles, which have an energy
of 3·5 MeV, is 0·025 mm (from the manufacturers data sheets), in
the plastic scintillator, its detection efficiency for alpha-
particles is 100%. The scintillator is also sensitive to beta-
particles, which are produced in the decay of tritium in the target

$$T \rightarrow He^3 + \beta^- + \bar{\nu}$$
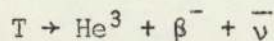
with a half life of 12·3 years. These beta-particles, with a
maximum energy of 18·6 KeV, have a corresponding maximum range in
aluminium of 0·0022 mm [28]. Also incident on the scintillator
are deuterons scattered through 90° by the target. The energy of
the deuterons depends on the accelerator voltage, which was varied
during the experiments, up to a maximum of 120 kv. Deuterons of
energy 120 KeV have a range in aluminium of 0·001 mm [29]. The
scintillator is therefore completely shielded from both these

Figure 2.3 The Alpha-Particle Detector.
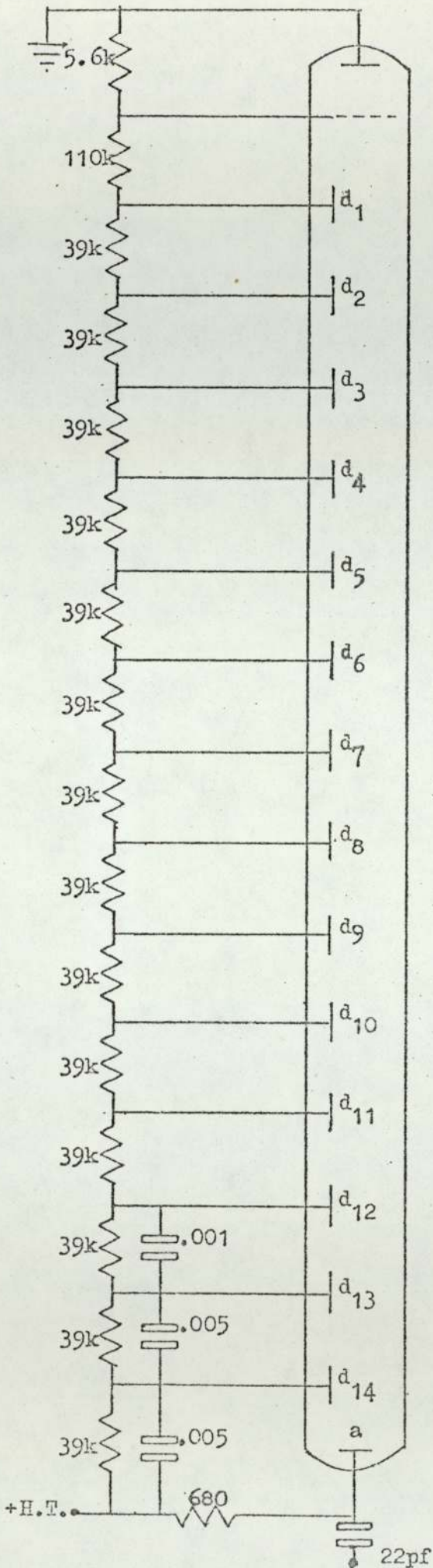
Figure 2.4
Alpha-Detector Dynode
Chain Circuit.
Resistances in Ohms
Capacitances in μF.

components of the background by an aluminium foil of thickness
0·0044 mm. Since the range of 3·5 MeV alpha-particles in alumin-
ium is 0·017 mm, the foil has a negligible effect on the alpha-
particle count.

2.5. Kinetics of d-T Reaction

For every alpha particle produced there is a corresponding
neutron, whose energy and direction can be calculated by classical
mechanics. (The energies involved are not relativistic, being much
less than the rest mass of the neutron, 938·55 MeV [30]).

Figure 2.5 shows a schematic representation of the reaction,
in both the laboratory and centre of mass reference frames.
Benveniste and Zenger [31] have investigated the kinetics of this
reaction. They find the relation:-

$$\tan \phi_\alpha = \frac{\frac{1}{2} \sin 2\phi_n + \sin \phi_n \sqrt{1/\gamma^2 - \sin^2 \phi_n}}{- \sin^2 \phi_n + \cos \phi_n \sqrt{1/\gamma^2 - \sin^2 \phi_n} - \frac{m_\alpha}{m_n}} \quad ..(2.1)$$

where:-
$$\gamma = \frac{V_{cm}}{V_n{}'} \quad ..(2.2)$$

V_{cm} is the velocity of the centre of mass frame relative to the
laboratory frame, $V_n{}'$ is the neutron velocity in the centre of mass
frame, m_n and m_α are the neutron and alpha-particle masses. Also:-

$$\frac{1}{\gamma^2} = \frac{m_\alpha}{m_n} \cdot \frac{m_d + m_T}{m_d} \left(\frac{m_T}{m_d + m_T} + \frac{Q}{E_o} \right) \quad ..(2.3)$$

E_o is the incident deuteron energy in the laboratory frame, m_d and
m_T are the deuteron and triton masses, and Q is defined as usual by;
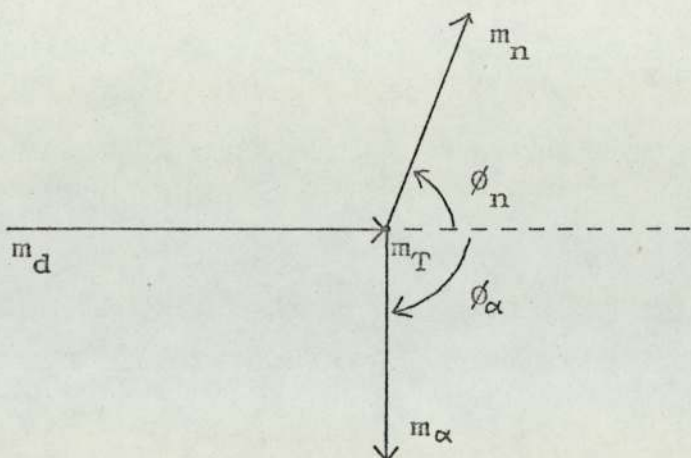
Laboratory Frame; solid angle is dw
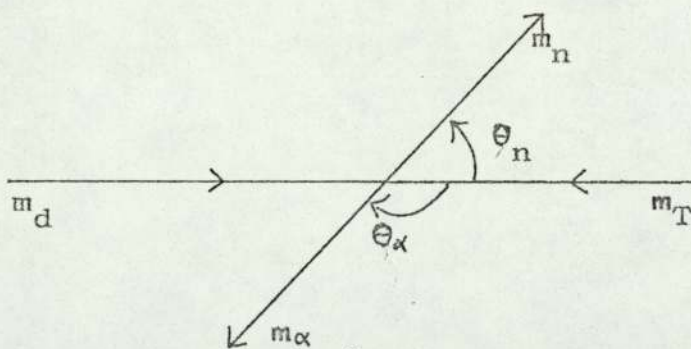
Centre of Mass Frame; solid angle is dw'.

Figure 2.5   The Kinematics of the d-T Reaction.

$$Q = (m_T + m_d - m_\alpha - m_n) \, c^2 \qquad ..(2.4)$$

hence:- $Q = 17 \cdot 586$ MeV

It can be seen from equations (2.1) and (2.3) that the relation
between ϕ_n and ϕ_α depends on the incident deuteron energy E_o. The
tritium target is "thick", that is, its thickness is greater than
the range of deuterons in it, so the value of E_o can vary from the
maximum bombarding energy used, in this case 120 KeV, to zero.
Thus E_o will be used to denote the energy of deuterons incident on
the target, equivalent to the accelerating voltage of the generator,
and ϵ will be used to denote the deuteron energy at the instant of
the reaction. Figure 2.6 shows the variation of ϕ_α with ϕ_n for
various values of ϵ in the required range, calculated [17] from
equations 2.1. and 2.3. Although the relation is not strictly
linear, over the range of angles considered, the departure from
linearity is negligible. Figure 2.6 shows that a range of ϕ_α from
$84°$ to $96°$ (that is, $\phi_\alpha = 90° \pm 6°$), leads to values of ϕ_n from
$76 \cdot 5°$ to $96°$, although the extreme values are given by only single
values of ϵ.

In these calculations it is assumed that angular straggling, due
to scattering in the target, can be neglected. It has been shown [17]
that this introduces an uncertainty of $\frac{1}{2}°$ in the results of these
calculations. In view of the overall angular resolution of the
system, this is negligible.

2.6. The Neutron Beam Profile

The cross-section for the $T(d,n)He^4$ reaction depends on the
value of ϵ as shown in figure 2.7. Thus as different values of
ϕ_n are produced by different values of
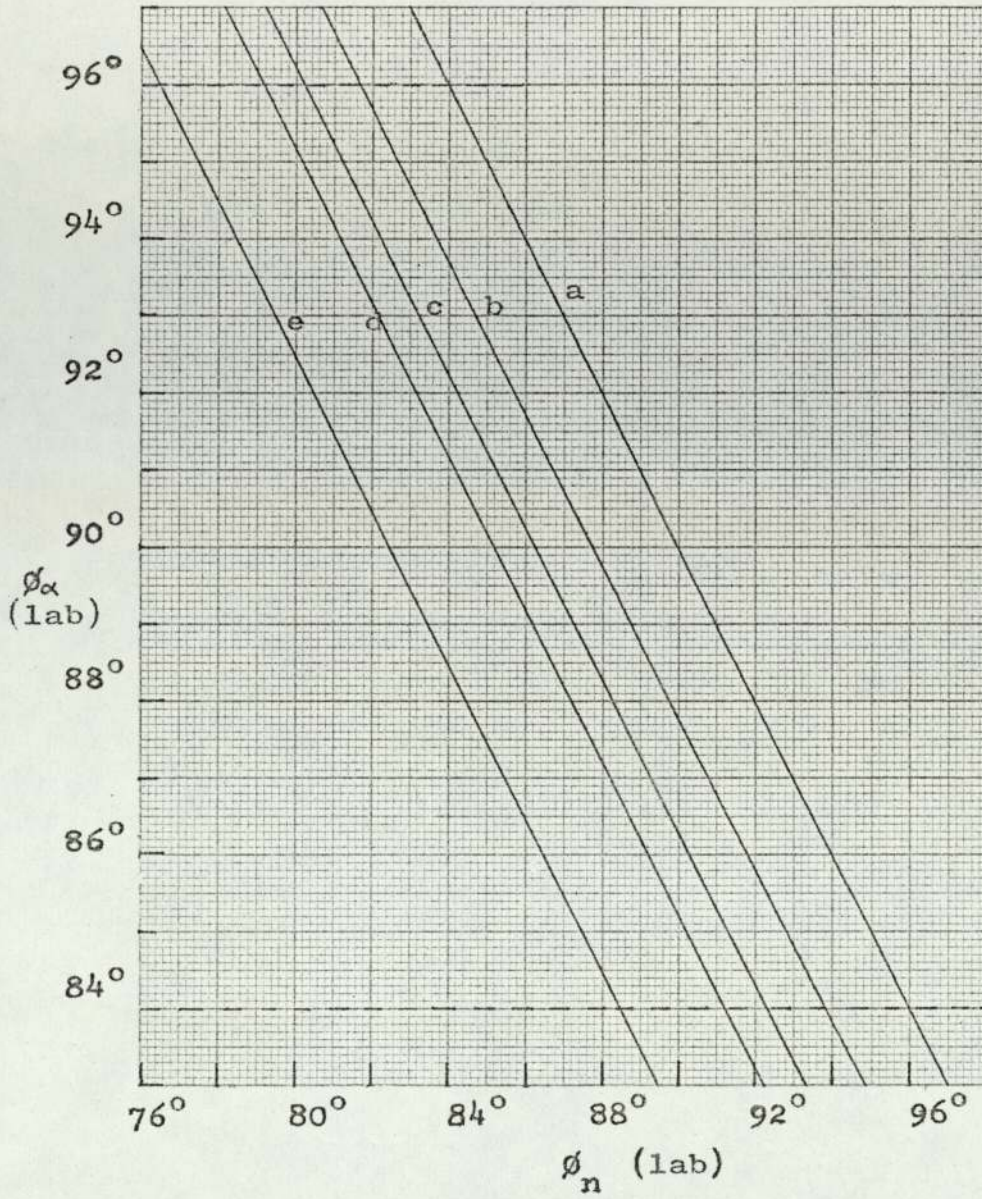
Figure 2.6 ϕ_α and ϕ_n for Various Values of
Deuteron Energy.

a; $\varepsilon = 0$
b; $\varepsilon = 10 \text{keV}$
c; $\varepsilon = 30 \text{keV}$
d; $\varepsilon = 50 \text{keV}$
e; $\varepsilon = 120 \text{keV}$
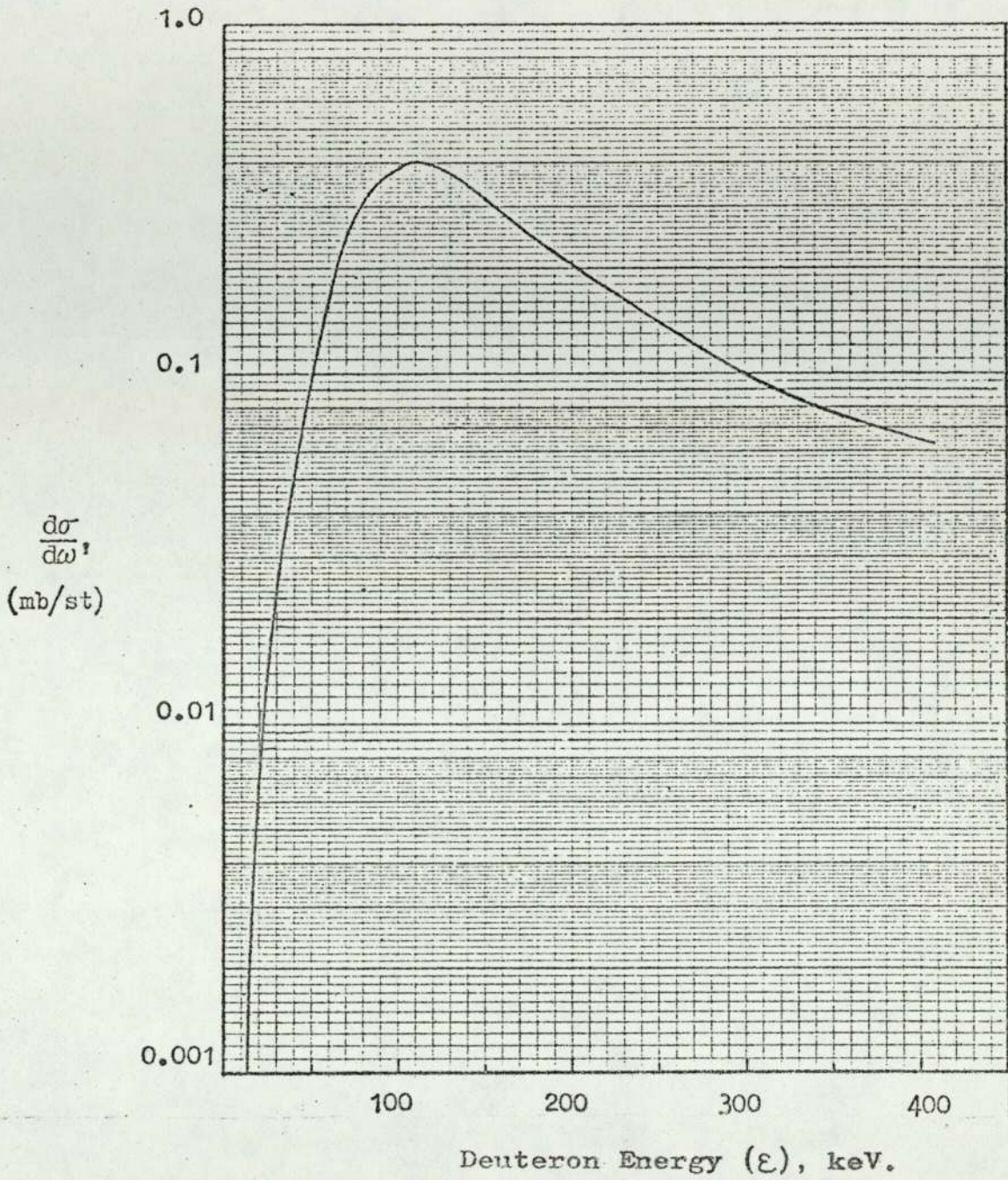
Figure 2.7   The Differential Cross-Section for the
T(d,n)He^4 Reaction vs. Deuteron Energy.

ϵ, the neutron yield will vary with ϕ_n. This variation is
described by the neutron beam profile. To calculate this, the
dependence of the neutron yield on the value of ϵ must be known.

2.6.1. The Neutron Yield

The differential cross-section for the d,T reaction has been
found by measurement to be isotropic in the centre of mass refer-
ence frame for values of incident energy up to 570 KeV [32]. If
$\sigma(\epsilon)$ is the total cross-section for the d,T reaction at a deuteron
energy ϵ, and N is the number of tritium nuclei per unit volume of
the target, then the neutron yield per incident deuteron, per unit
solid angle is:-

$$Y(\theta_n) = \int_0^{E_o} \frac{\sigma(\epsilon)}{4\pi} \cdot \frac{N}{d\epsilon/dx} \, d\epsilon \qquad ..(2.5)$$

Here the deuteron energy is treated as a variable in the range E_o
to zero, as the deuteron slows down in the target. This formula
assumes the incident deuteron flux is constant throughout the target.
This is a good approximation because only a small fraction of the
deuterons react with the tritium.

2.6.2. The Anisotropy Factor

To convert to the laboratory frame, the cross-section must be
multiplied by the anisotropy factor:-

$$\frac{dw'}{dw} = \frac{\sin \theta_n \, d\theta_n}{\sin \phi_n \, d\phi_n} \qquad \begin{array}{l} \text{(centre of mass frame)} \\ \\ \text{(laboratory frame)} \end{array} \qquad ..(2.6)$$

The relation between θ_n and ϕ_n is [31] :-

$$\cos \theta_n = -\gamma \sin^2 \phi_n \pm \cos \phi_n \sqrt{1 - \gamma^2 \sin^2 \phi_n} \qquad ..(2.7)$$

Thus again dw'/dw depends on ϕ_n and ε. Figure 2.8 shows this dependence, with ε as a parameter. It can be seen from this figure that over the range of interest of ϕ_n, namely 76° to 96°, dw'/dw is approximately equal to unity, with an error of at most $1 \cdot 5\%$. This factor is thus neglected.

2.6.3. The Stopping Power

The factor $d\varepsilon/dx$ in equation 2.5, represents the rate of energy loss of deuterons of energy ε in the titanium-tritium target also called the stopping power of the target. To determine this, the loading factor, or number of tritium atoms in the target must be known. A reasonable estimate for this factor[31] is unity. Then the stopping power is given by:-

$$\frac{d\varepsilon}{dx} = \frac{48}{48 + 3} \left(\frac{d\varepsilon}{dx}\right)_{Ti} + \frac{3}{48 + 3} \left(\frac{d\varepsilon}{dx}\right)_T \qquad ..(2.8)$$

Here 3 and 48 are the atomic weights of tritium and titanium respectively, and $(d\varepsilon/dx)_{Ti}$ represents the rate of energy loss in normal titanium, and $(d\varepsilon/dx)_T$ in tritium. Benveniste and Zenger [31] obtained $(d\varepsilon/dx)_{Ti}$ by interpolation of proton data for various elements, and by assuming the rate of energy loss is a function only of the particle velocity, so that:-

$$\left(\frac{dE_p}{dx}\right)_\varepsilon = \left(\frac{dE_d}{dx}\right)_{2\varepsilon} \qquad ..(2.9)$$

The stopping power for deuterons in tritium has also been found from Phillip's [33] measurements on proton energy losses in
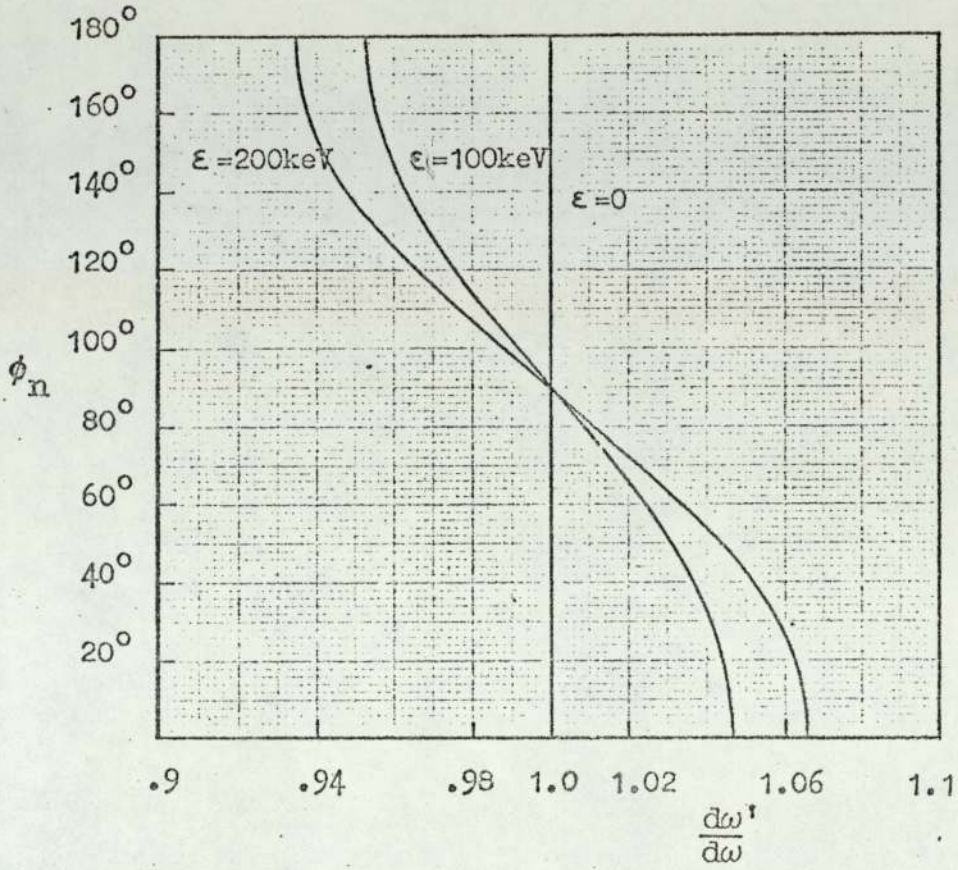
Figure 2.8 The Neutron Anisotropy Factor as a Function
of Neutron Scattering Angle ϕ_n.

hydrogen and helium. Combining the two functions, the stopping powers of both materials, in equation 2.8, the stopping power of the tritium-titanium target is found. This is shown in figure 2.9

The neutron yield can now be expressed, from equation 2.5:-

$$Y(\theta_n, \epsilon) \propto \frac{\sigma(\epsilon)}{d\epsilon/dx} \, d\epsilon \qquad ..(2.10)$$

Here $Y(\theta_n, \epsilon)$ is the neutron yield per unit solid angle, per unit deuteron energy deposited in the target. This has been evaluated [17] numerically in 10 KeV steps, taking at each step, mean values of $\sigma(\epsilon)$ and $d\epsilon/dx$ from figures 2.7 and 2.9 respectively. The result is shown in figure 2.10.

2.6.4. The Neutron Beam Profile

The neutron beam profile is finally found from figures 2.6 and 2.10. The calculation is performed in 1° steps. For each value of ϕ_n from 76° to 96° inclusive, figure 2.6 shows the range of ϵ which contributes to the neutron yield. Figure 2.10 is then consulted to determine the relative yield that this range of values of deuteron energy can produce. This is found from the area under the curve in the relevant range of ϵ. The areas are then normalized so that the maximum relative neutron yield is 1·0. The resultant neutron beam profile is shown in figure 2.11. It can be seen that the full width at half maximum of the beam is 12°, and that the total width of the beam of associated neutrons is 17°.

To a certain extent, this calculation repeats the work of Connell [17], but it has been given here in some detail for completeness, and also because the present work uses a wider range
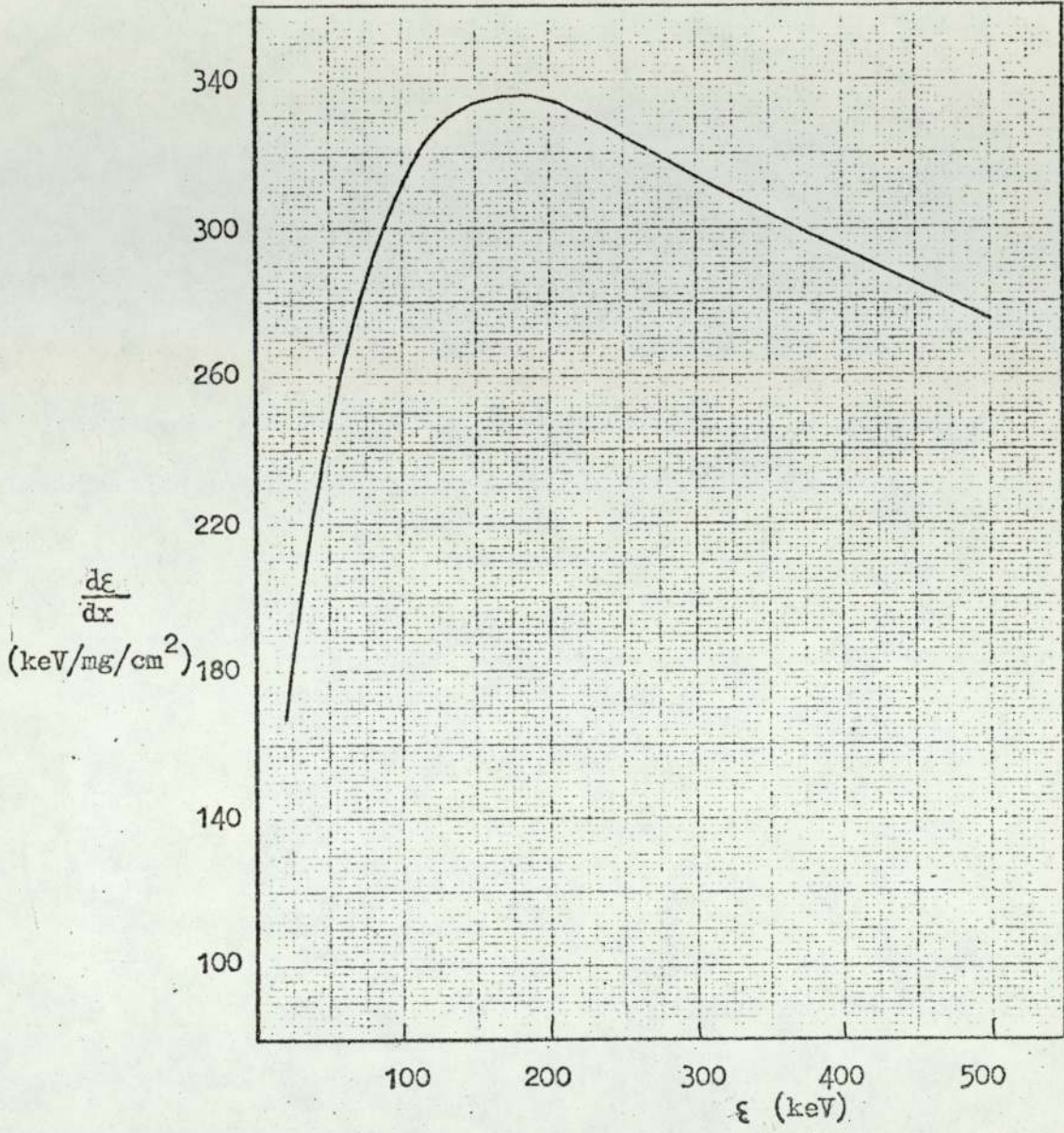
Figure 2.9   The Stopping Power of Deuterons in
             Titanium-Tritide[31].
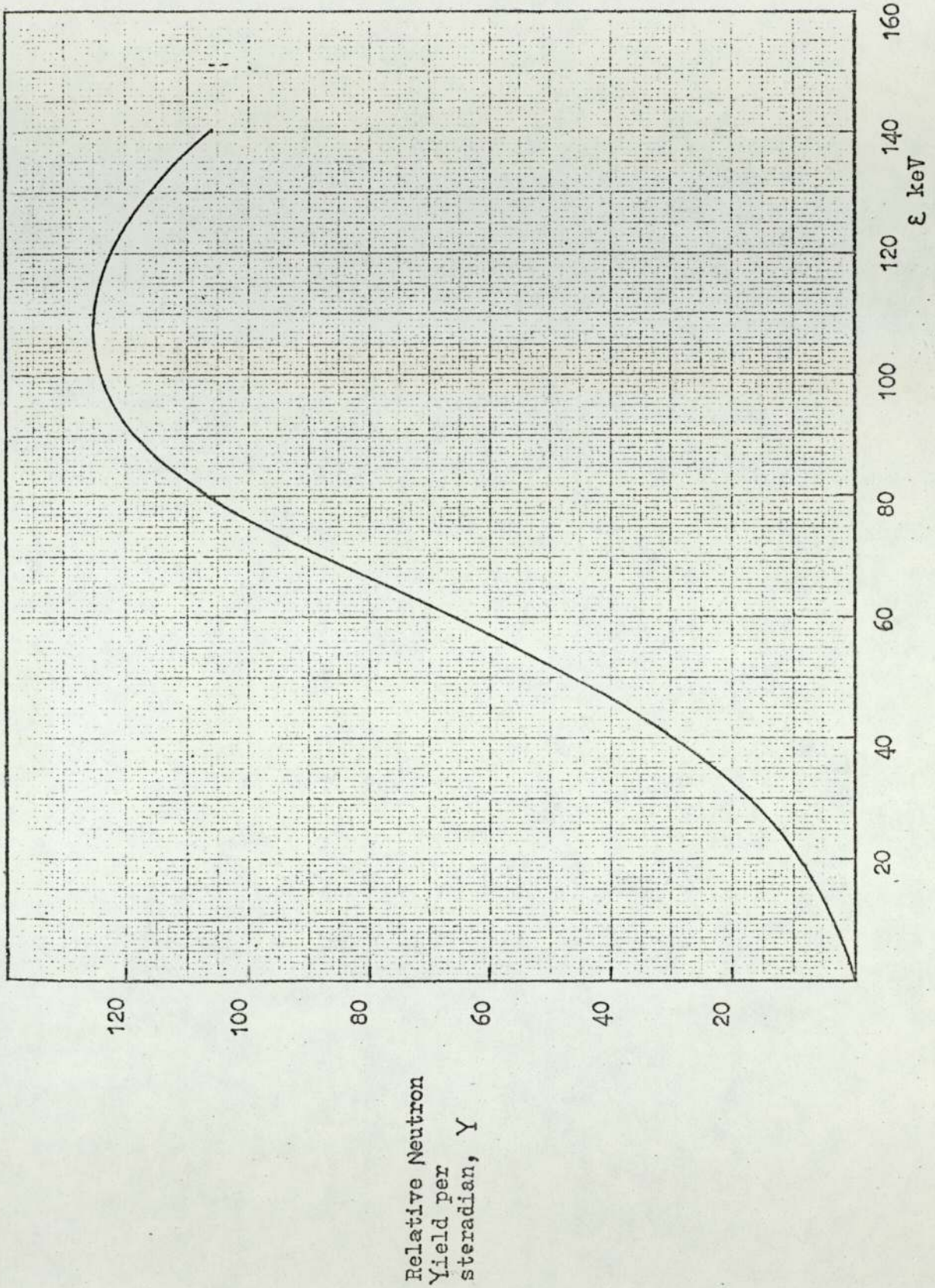
Figure 2.10 The Relative Neutron Yield as a Function of Deuteron Energy.
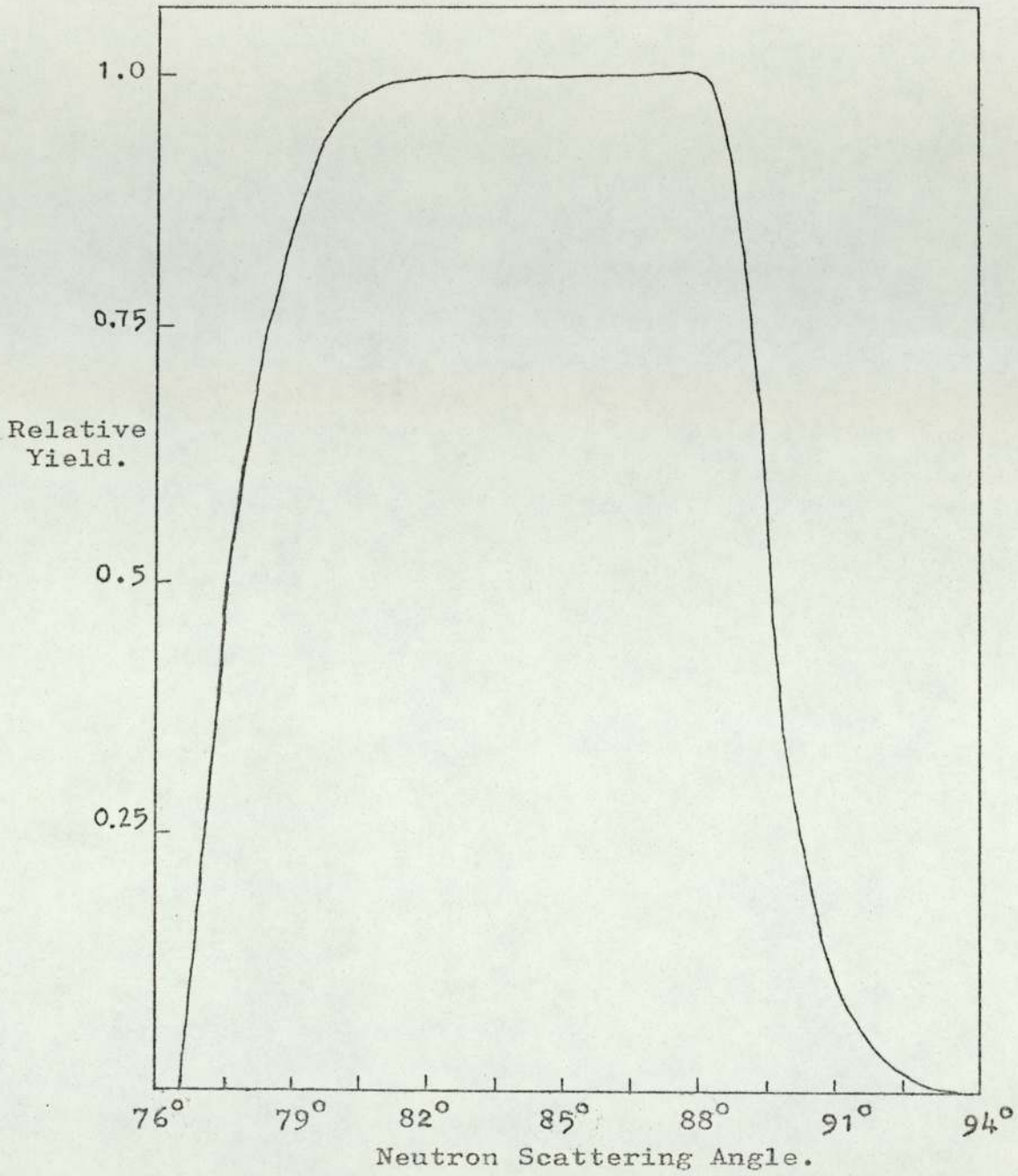
Figure 2.11   Neutron Beam Profile.

of ϕ_α, ($\pm 6°$) than the previous work, which used $\phi_\alpha = 90° \pm 4°$.
It has thus been necessary to check that the assumptions made are
still valid for the present case. The increase in the range of
ϕ_α affects mainly the anisotropy factor dw'/dw. Here the assump-
tion that this factor is unity is still valid.

Thus a beam of associated neutrons is defined, extending from
approximately 77° to 93° to the deuteron beam in the horizontal
plane, and with half angle 3·5° in the vertical plane.

2.6.5. The Neutron Line Shape

The line shape refers to the energy distribution of neutrons
at a given angle. The neutron energy, E_n, is a function of the
angle of emission ϕ_n, and of the incident deuteron energy, ε;

$$E_n = (\frac{m_d}{m_d + m_T})^{\frac{1}{2}} \frac{m_n}{m_d} \varepsilon \cos 2\phi_n + \frac{m_\alpha}{m_n + m_d} (\frac{m_T}{m_d + m_T} \frac{\varepsilon}{} + Q)$$

$$\pm \frac{2 \cos \phi_n}{m_n + m_d} (\frac{m_d \, m_n \, m_\alpha}{m_n + m_\alpha} \cdot \varepsilon \, (\frac{m_T \, \varepsilon}{m_d + m_T} + Q))^{\frac{1}{2}} \times$$

$$\times (1 - \frac{m_\alpha \, m_n \, \varepsilon \, \sin^2 \phi_n}{m_\alpha \, m_T \, \varepsilon + Q \, (m_d + m_T)})^{\frac{1}{2}} \qquad ..(2.11)$$

Here m_d, m_T, m_n and m_α are, as stated previously, the deuteron,
triton, neutron and alpha-particle masses respectively, and Q has
been previously defined. This expression has been evaluated [17]
at $\phi = 84°$ for a range of values of ε from 120 KeV to zero. The
neutron yield at this value of ϕ_n and at the various values of ε
has also been evaluated [17], from equation 2.5. The resulting
neutron line shape is shown in figure 2.12, which shows that the
energy spread of the neutrons at this angle is 100 KeV. The
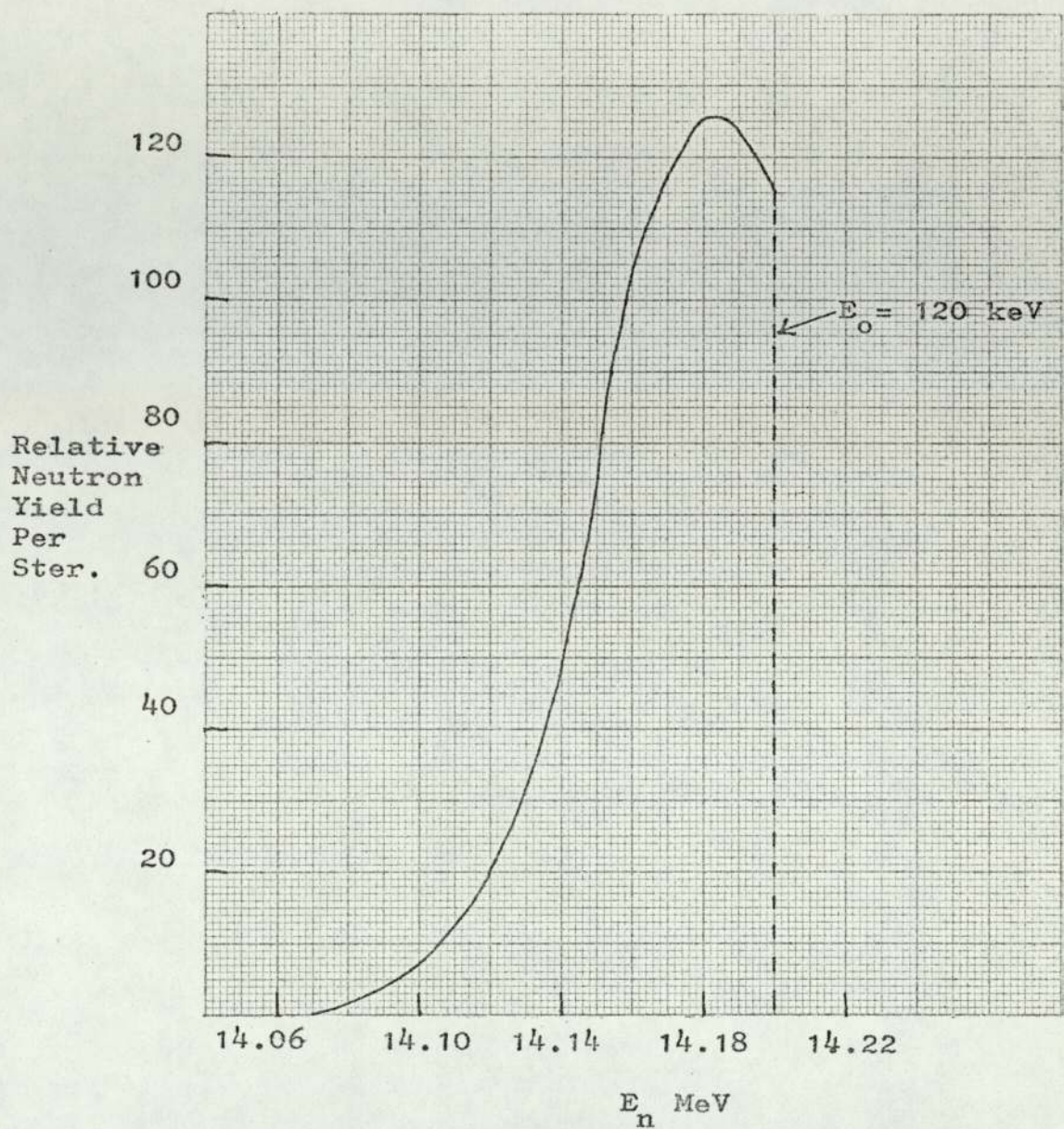
Figure 2.12   The Neutron Line Shape at $\phi_n = 84°$.

calculation at this value of ϕ_n is typical, due to the small range of ϕ_n which is of interest.

2.7. The Scattering Sample

The magnesium sample is a block of the natural element, of purity 99%, cast to the required shape*. The dimensions are 30 mm x 120 mm x 126 mm. Due to difficulties in casting, the shape of the sample is somewhat irregular, producing errors of 1 mm in each of the dimensions. It was not found possible to machine the sample to size as magnesium filings are inflamable.

The chromium sample consists of chromium powder, purity 99·95%**, compressed into an aluminium can of internal dimensions 28·4 mm x 85·3 mm x 90·6 mm. The density of the packed chromium powder is 2·74 gms/cc, compared with 6·92 gm/cc for the solid metal. To subtract the contribution to the gamma-ray spectrum of the aluminium container, an identical empty can replaces the chromium sample for the background runs. A solid chromium block was not available, as chromium is used mainly as foil or film coating for other materials.

Aluminium is chosen for the container by a consideration of the macroscopic cross-sections, Σ, of possible materials. The fraction of neutrons not interacting in a thickness, x, of material is given by $e^{-\Sigma x}$. It is required that as few neutrons as possible will interact in the sample container, so that material is chosen which has the minimum value of Σ. This is given by:

----

* Supplied by BKL Alloys Ltd., Birmingham.

** Suplied by New Metals and Chemicals Ltd., London.

$$\Sigma = \frac{N_o \rho}{A} \sigma_\tau \qquad\qquad ..(2.12)$$

where N_o is Avagadros number, ρ is the density, A is the atomic weight, and σ_τ is the total cross-section for 14 MeV neutron interactions. Table 1 shows values of Σ for various possible materials.

Material	$(\Sigma/N_o) \times 10^{-24}$ cm^{-1}
Aluminium	0·175
Steel	0·358
Tin	0·273
Yellow Brass	0·380

TABLE I

Macroscopic Cross-Sections of Various Container Materials

Aluminium is seen from this table to be the best material for the sample container.

The iron sample consists of a rectangular block of '0' quality dynamo steel, which is 99·27% pure iron machined to the dimensions 9·15 mm x 92·00 mm x 120·00 mm. To prevent rusting contaminating the sample, it was sprayed with a P.T.F.E. solution which forms a coating, with a thickness of a few molecular diameters. It is expected that this layer will produce negligible gamma-ray yield due to its small thickness and the low atomic number of its constituents.

In each case, the scattering sample is placed at a distance of 250 mm from the target, so as to subtend completely the neutron

beam, (figure 2.13). The thickness of each sample has been calculated so as to result in a transmission of 70% or over. (For magnesium and iron the figure is 70%, for chromium 80%, resulting from the low density of the powdered sample). It is thought (34, 35) that at thicknesses of this order, neutron beam attenuation and multiple scattering are mutually compensating, so the neutron flux may be considered constant throughout the thickness of the sample. This assumption will be considered in more detail later (section 3.10).

The sample is placed at 45° to the central axis of the neutron beam, so as to minimise self absorption of gamma-rays in the sample, for scattering angles in the range 0° to 90°.

2.8. Gamma-Ray Detection

Gamma-rays produced in the sample are detected by a 3" x 3" NaI(Tℓ) crystal scintillator, optically coupled by a plano-concave perspex plate, central thickness 15 mm, to a Phillips 58 AVP photomultiplier, figure 2.14. The reasons for the use of a NaI scintillator are given in Section 2.9.1.

The resistance chain used to supply voltage to the stages of the photomultiplier is shown in figure 2.15. The design of this dynode chain is based on that recommended by the manufacturers [36] for fast timing purposes. The voltages applied to the focussing grids and first dynode are critical to good timing, as it is in this region that the electrons have the lowest energy, and are thus most susceptible to stray fields, even if weak. Each tube is tested by the manufacturer to determine the optimum values of V_{k-g1} and V_{k-d1} for accurate focussing of electrons from the

Figure 2.13   The Tritium Target and Sample Stand
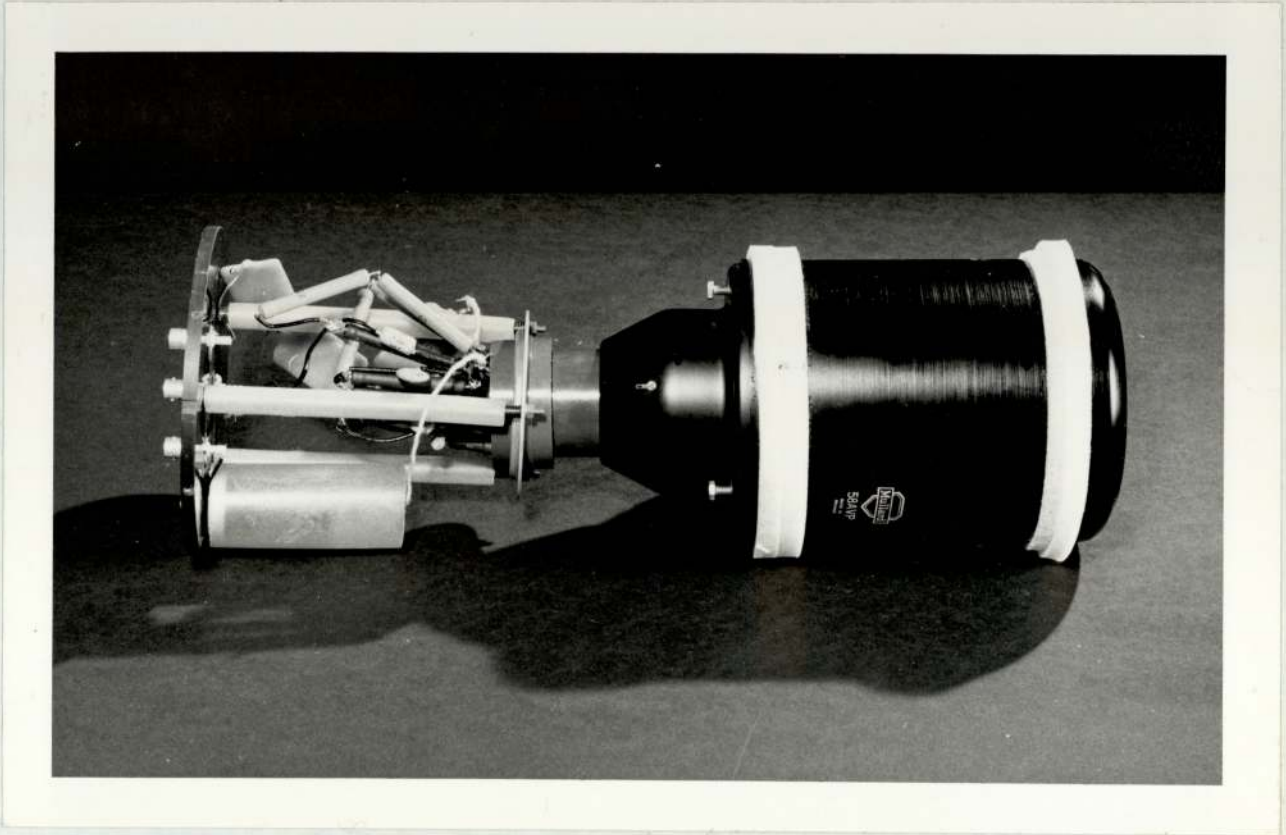
Figure 2.14   Gamma-Ray Photomultiplier

Figure 2.15
Gamma-Ray Detector
Dynode Chain Circuit.
Resistances in Ohms.
Capacitances in μF.
L=Linear Signal
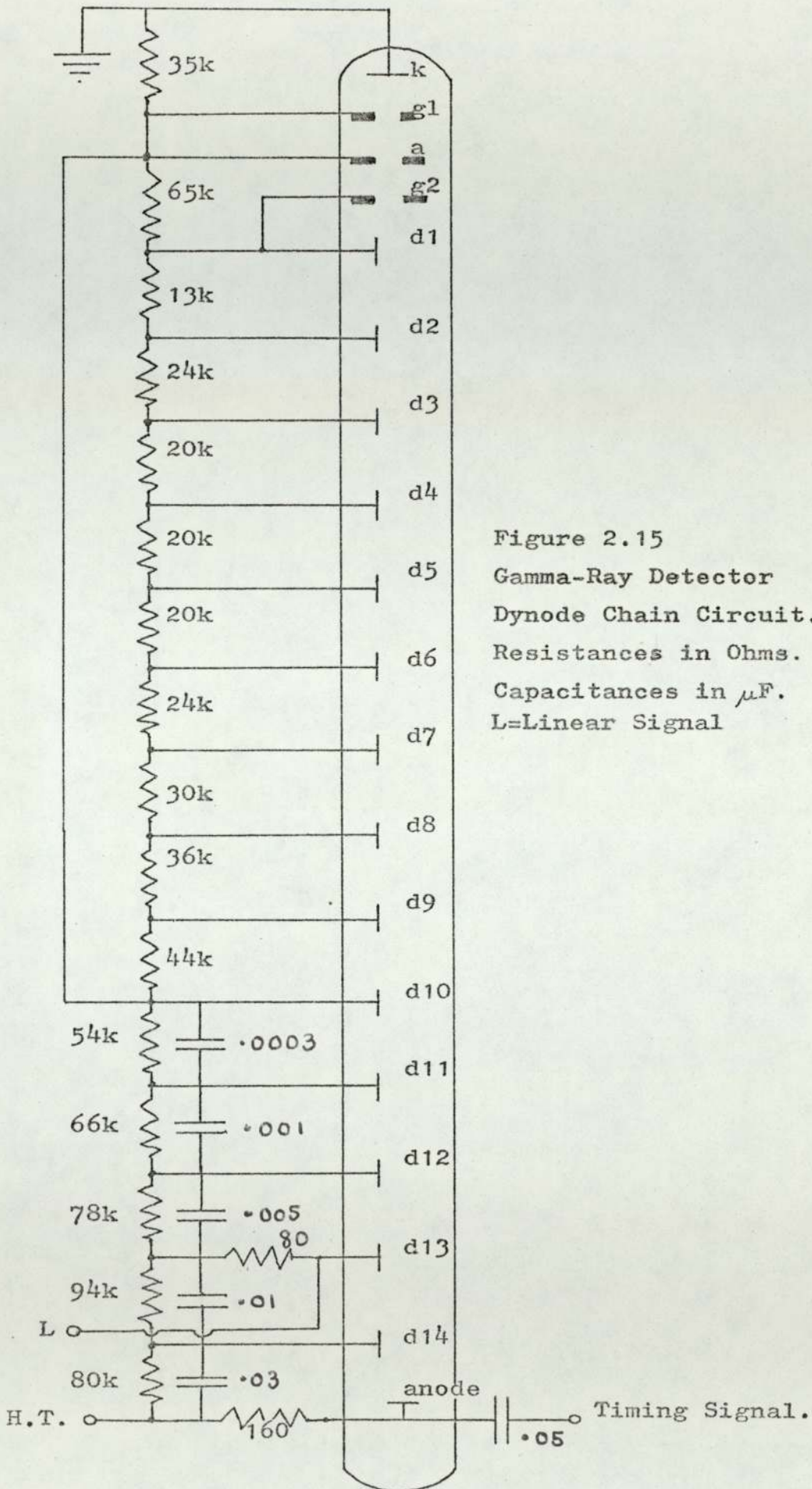
photocathode on to the first dynode.

The capacitors across the final stages of the dynode chain are used to store charge, to enable the peak current of the output pulse to be greater than that of the steady dynode chain current. For example, the chain current is 3 mA, and the peak current of a typical 3 volt pulse across the 160 Ω output resistor is 20 mA. The output pulse must not draw power from the chain supply, as this must remain stable, to maintain stable voltages at the dynodes. The peak value of the current pulse is obviously attained for only a small fraction of the pulse length, and cannot be maintained continuously. This consideration also limits the counting rate which can be achieved before the gain begins to decrease, but this is not a limiting factor in the present work.

A mu-metal cylinder is used to shield the photocathode, focussing grids, and first few dynodes, from the earth's magnetic field. This is strong enough to cause defocussing of electrons in this region of low energy.

The detector is shielded from scattered neutrons by a combination of lead, borax, and paraffin wax cylinders as shown in figure 2.16. The effect of the shielding material is shown in figure 2.17, together with the effect of the shadow bar. This steel bar is placed so as to prevent neutrons straight from the tritium target impinging on the detector and creating a high background signal.

2.9. Time Resolution

The problem of obtaining good time resolution has been widely discussed [37 - 40]. The time resolution available from
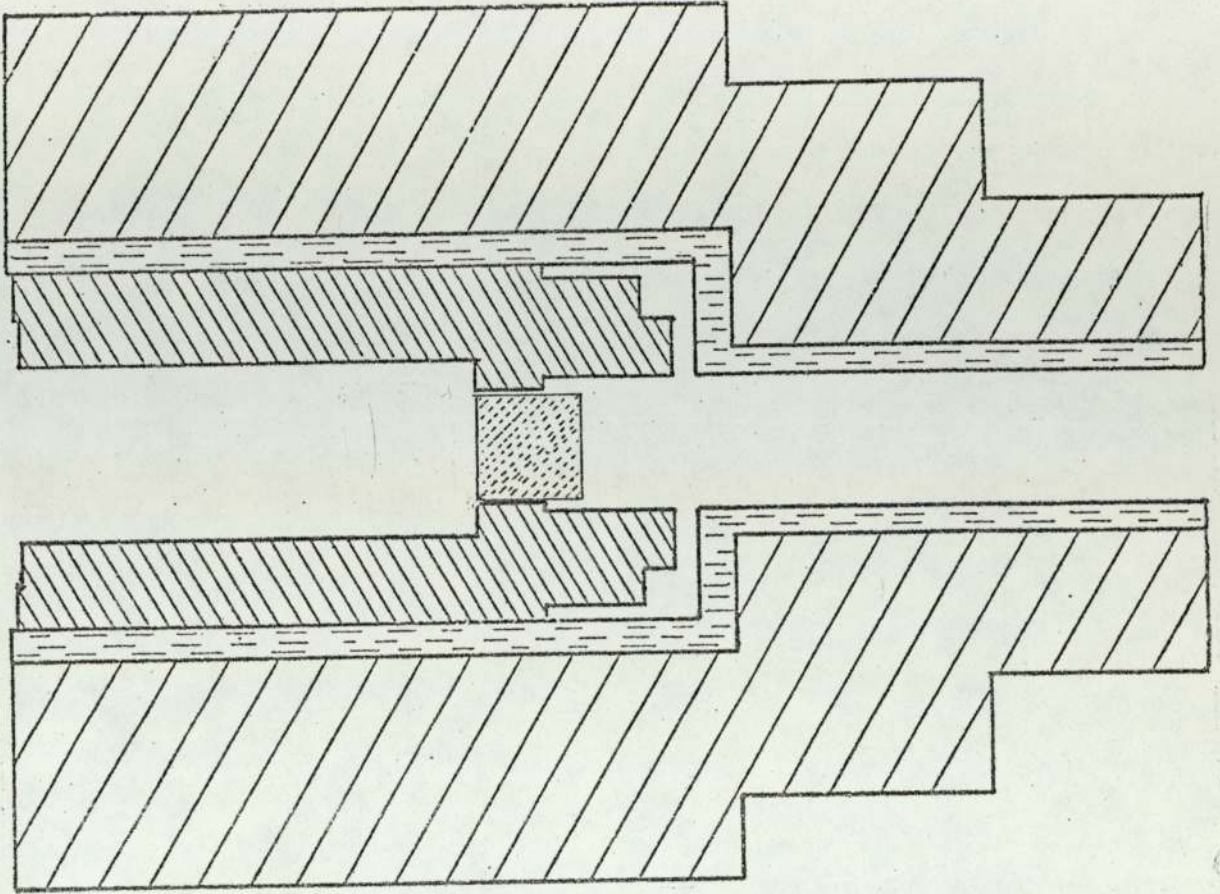
Paraffin Wax   Boric Oxide

Lead   NaI Crystal

0   5   10
|____|____| cm.

Figure 2.16   Cross-section of the Neutron Shield.
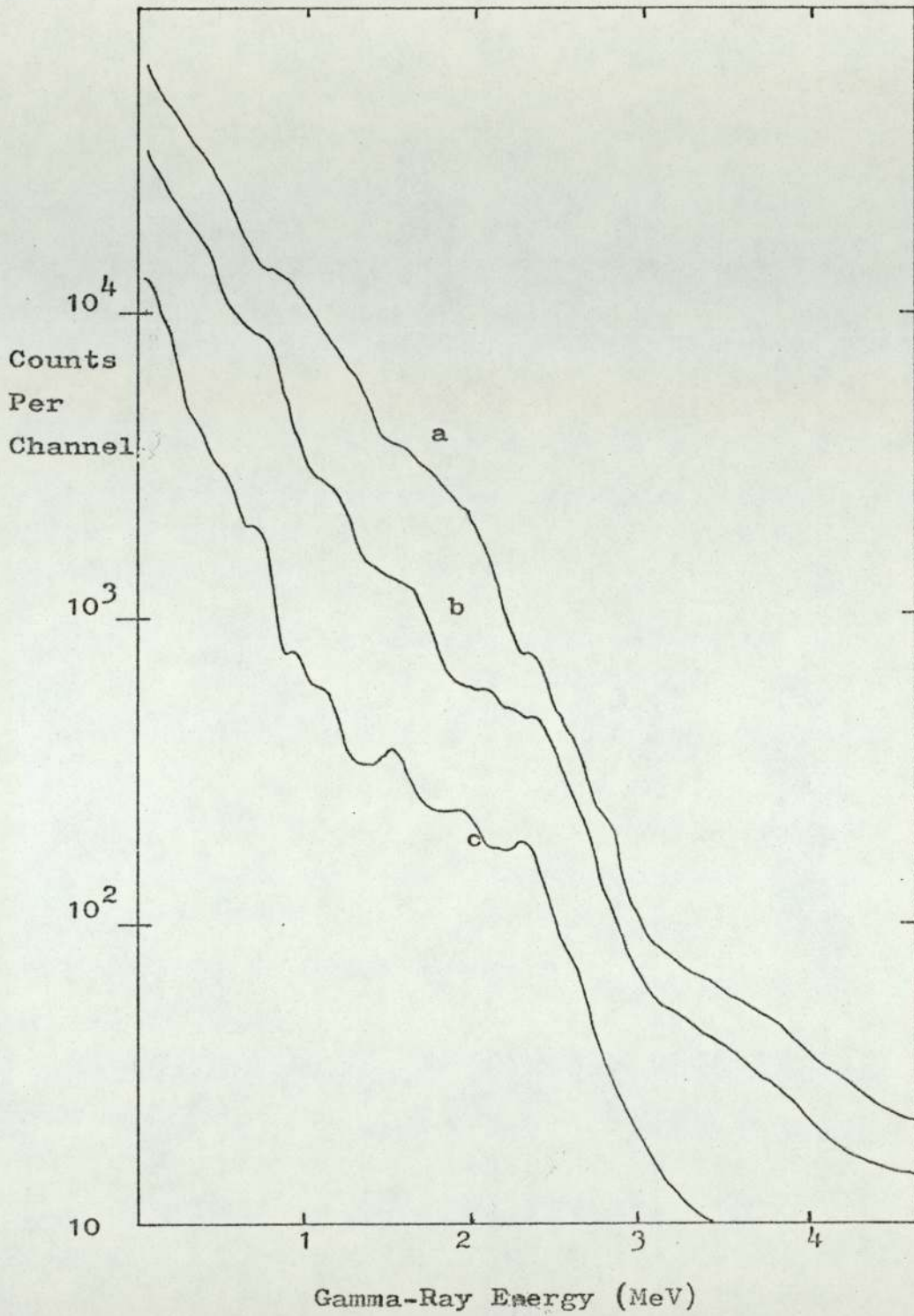
Figure 2.17 The Effect of the Gamma Ray Shield.

    a = Unshielded Spectrum

    b = Spectrum with Shield

    c = Spectrum with Shield and Shadow-bar

a scintillation detection system depends mainly on the characteristics of the output signal from the photomultiplier. Since comparatively high power signals are available, noise in the following circuitry is not a problem [41], so that subsequent instrumentation, if properly designed, does not add to the timing inaccuracy.

The first stages in the detection process are the transfer of energy from the incident radiation to the scintillator by excitation of optically active states, the subsequent decay of these states and consequent emission of light, and the collection of this light onto the photocathode of the photomultiplier. These are considered to be governed by Poissonian statistics.

In the multiplication process, it is particularly the flight of the first electron, emitted from the photocathode, to the first dynode, which can produce timing errors. This is because the electron energy is low, and path lengths from different parts of the photocathode may vary considerably. Careful consideration of the design [42] of the photocathode - first dynode geometry, with the addition of focussing grids, and adjustment of the accelerating voltage, combined with good design of the rest of the tube can reduce the timing error considerably. For example, the 58 AVP photomultiplier has a quoted [43] transit time spread of 1·0 nsec, and a photocathode diameter of 110 mm.

If the excitation of the scintillator takes place at the instant t = 0, then the detection of the nth photoelectron takes place a time $\bar{t}$ afterwards, where; [37]

$$\bar{t} \simeq \frac{n\tau}{R} \left[1 + \frac{(n + 1)}{2R} + \dots \right] \qquad \qquad ..(2.13)$$

Here τ is the mean decay time of the scintillator, and R is the average number of primary photoelectrons produced for each detection event. In omitting higher termsof the series it is assumed that n << R. Also the variance of $\bar{t}$ is:-

$$v \cong \frac{n\tau^2}{R^2}[1 + \frac{2(n + 1)}{R} + \dots] \qquad \qquad ..(2.14)$$

Taking into account the effect of the spread in transit times through the photomultiplier, [44, 45] the following result is obtained:

$$v \cong \frac{n\tau^2}{R^2} + \frac{\sigma^2}{n} \qquad \qquad ..(2.15)$$

where σ gives a measure of the transit time spread of the photomultiplier tube. This expression for v has a minimum of $2\sigma\tau/R$ at $n = \sigma R/\tau$. Thus to obtain best timing resolution from a scintillation detector, the scintillator should have a short decay time and high light output, and the photomultiplier a low transit time spread and high photon conversion efficiency, (a high proportion of the light incident on the photocathode should result in the emission of electrons). It can also be seen that if a timing pulse is obtained after the collection of a fraction n/R of the total charge produced in the detection of a single gamma-ray, this fraction should be a constant for optimum timing resolution. This result is confirmed experimentally [46 - 48] and has previously been predicted theoretically [49].

2.9.1. Choice of Scintillator

Since the time resolution obtainable from a scintillator

is proportional to $\sqrt{\tau}/R$, it is necessary to choose a scintillator with a low value of τ and a high value of R. From this point of view it is best to use a plastic scintillator such as NE102 which has $\tau = 2 \cdot 51$ nsec and R equal to 65% of that of anthracene [50] which is used as a standard. NaI, on the other hand, has $\tau = 250$ nsec and R = 240% of anthracene [26]. Thus for timing, the plastic NE102 is approximately five times better than NaI.

However, the detection efficiency must also be considered. To perform energy analysis ofthe gamma-ray energy spectra, the total gamma-ray energy must be detected on a substantial number of occasions, so the full energy peak is resolved. Although some multiple Compton scattering occurs, the main process for the detection of all of the incident gamma-ray energy is the photo-electric effect. However, the cross-section for this process is proportional to Z^n where n is between 4 and 5 [50]. Plastic scintillators are composed of carbon and hydrogen with some nitrogen and oxygen [51], so an average value of Z is about 6, while for NaI the value of Z is the average of 11 and 53, that is 32. Thus clearly NaI is more efficient by a factor of $(32/6)^n \approx 10^3$ at detecting the total energy of an incident gamma-ray than is a plastic scintillator. Thus energy analysis requirements dictate that a NaI crystal must be used for gamma-ray detection.

Good timing resolution (4 - 5 nsec FWHM) and energy resolution ($0 \cdot 14$% at $1 \cdot 33$ MeV) are obtainable for gamma-ray detection by GeLi detectors. However it was calculated that the rate of radiation damage from fast neutrons would be so high that the useful life of the detector would be only 20 hrs. For this reason a GeLi detector was not used.

2.9.2. Timing Techniques

A brief summary of the timing circuitry of the original spectrometer will now be given, leading to a description of the alterations made to the system.

The timing circuitry is shown in figure 2.18. The "start" pulse of the time converter was obtained from the gamma-ray detector. The pulse from the 14th dynode was amplified by a "fast" amplifier, that is, one which was driven into saturation. The resulting pulse then triggered a switching circuit, producing a pulse with a re- latively short rise time, 20 nsec, compared with the rise time of the photomultiplier dynode output pulse, which was 40 nsec. To allow time for the operation of the slow coincidence gate in the "stop" line, this pulse was delayed for 220 nsec by a 40 m length of cable before connecting with the "start" input of the time converter.

The anode pulse from the alpha-particle detector was matched into a 35 m long coaxial cable by means of an emitter-follower which connected with a discriminator and pulse shaping circuit. The anode pulse from the gamma-detector was similarly treated, and if these two pulses were in slow coincidence, the alpha-pulse was used to "stop" the time converter. The gating time of the slow coincidence circuit was 400 nsec. Timing uncertainties in the gamma-pulse did not affect the "stop" pulse, as this took its timing information only from the alpha-pulse. It was necessary, however, to ensure that the gamma-pulse arrived at the slow coin- cidence gate before the related alpha-pulse, within the 400 nsec gating time.

The reason for the use of the slow coincidence gate was to
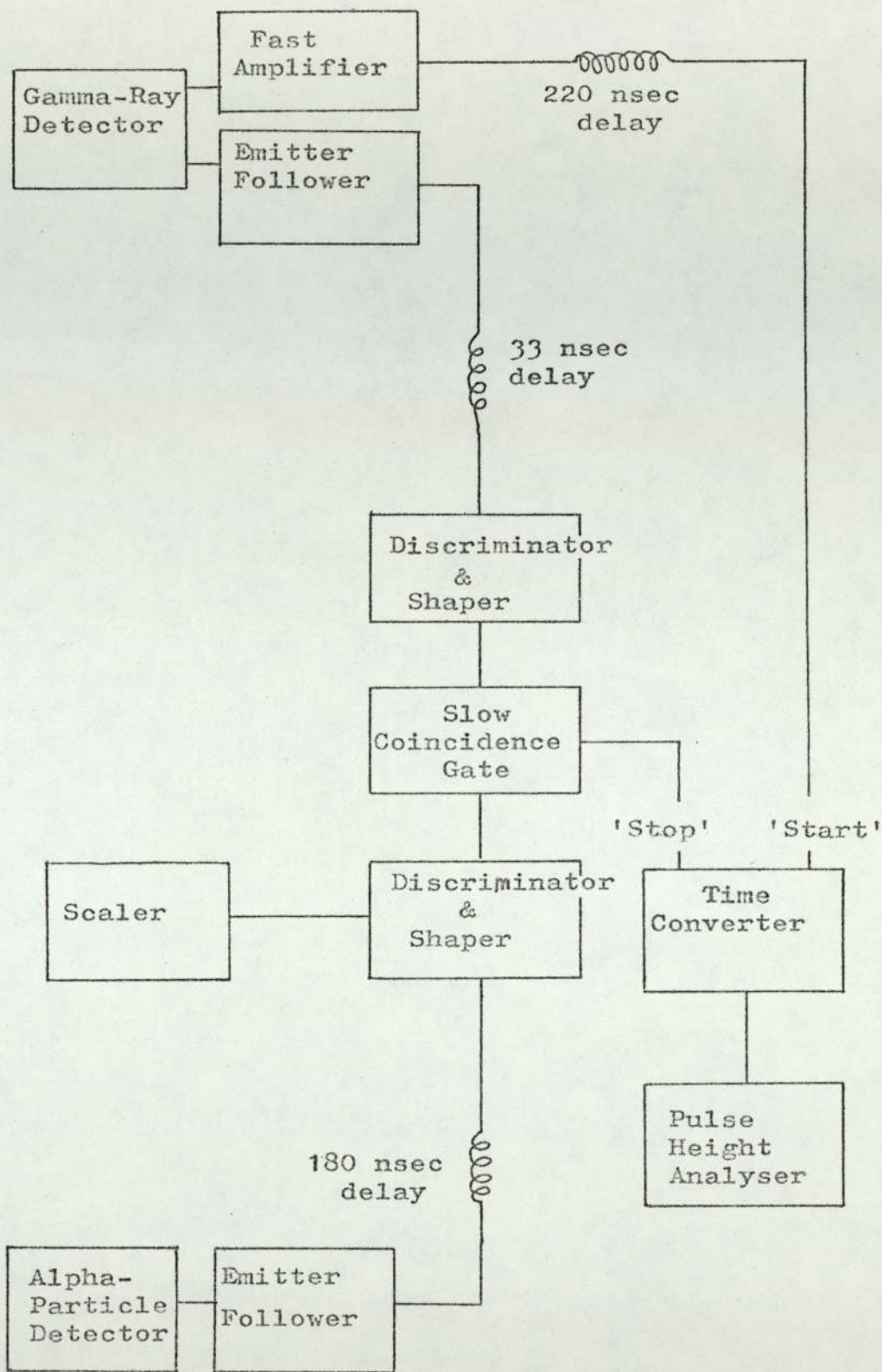
Figure 2.18 Original Timing System.

reduce the high count rate from the alpha-particle detector to a level which was acceptable to the time converter unit. This had the additional advantage of reducing the number of random events in the time spectrum, caused when the time converter was stopped by an alpha pulse which was unrelated to the gamma-pulse which had started the time converter.

The time resolution obtainable with this system is shown in figure 2.19, which is a time spectrum of a silicon scattering sample, at a scattering angle of 30°. It can be seen that the full width at half maximum (FWHM) of the gamma-peak is 11·5 nsec, and the full width at 1/10 maximum (FWTM) is 21·5 nsec.

As described above, the method of obtaining the timing infor- mation from the gamma-pulse was the fixed-level triggering technique. It has been found [26] that although this method gives good time resolution for a narrow dynamic range, that is, range of incident gamma energies, the resolution drops considerably as the energy range increases. This is because the triggering level cannot be set at the correct fraction of pulse height for a wide variety of pulse heights, and because "walk" becomes a serious problem. "Walk" refers to the shift in the time of crossing the triggering level of pulses which start at the same time, but which have different heights, (see figure 2.20) and is independent of any statistical effects on the time resolution.

To overcome these difficulties, the timing circuitry was replaced by that shown in figure 2.21. The gamma-timing pulse was taken from the anode rather than the 14 th dynode. This is general practise, as better timing is obtained from the larger pulse. An emitter follower was not found necessary to match the signal into

- 44 -
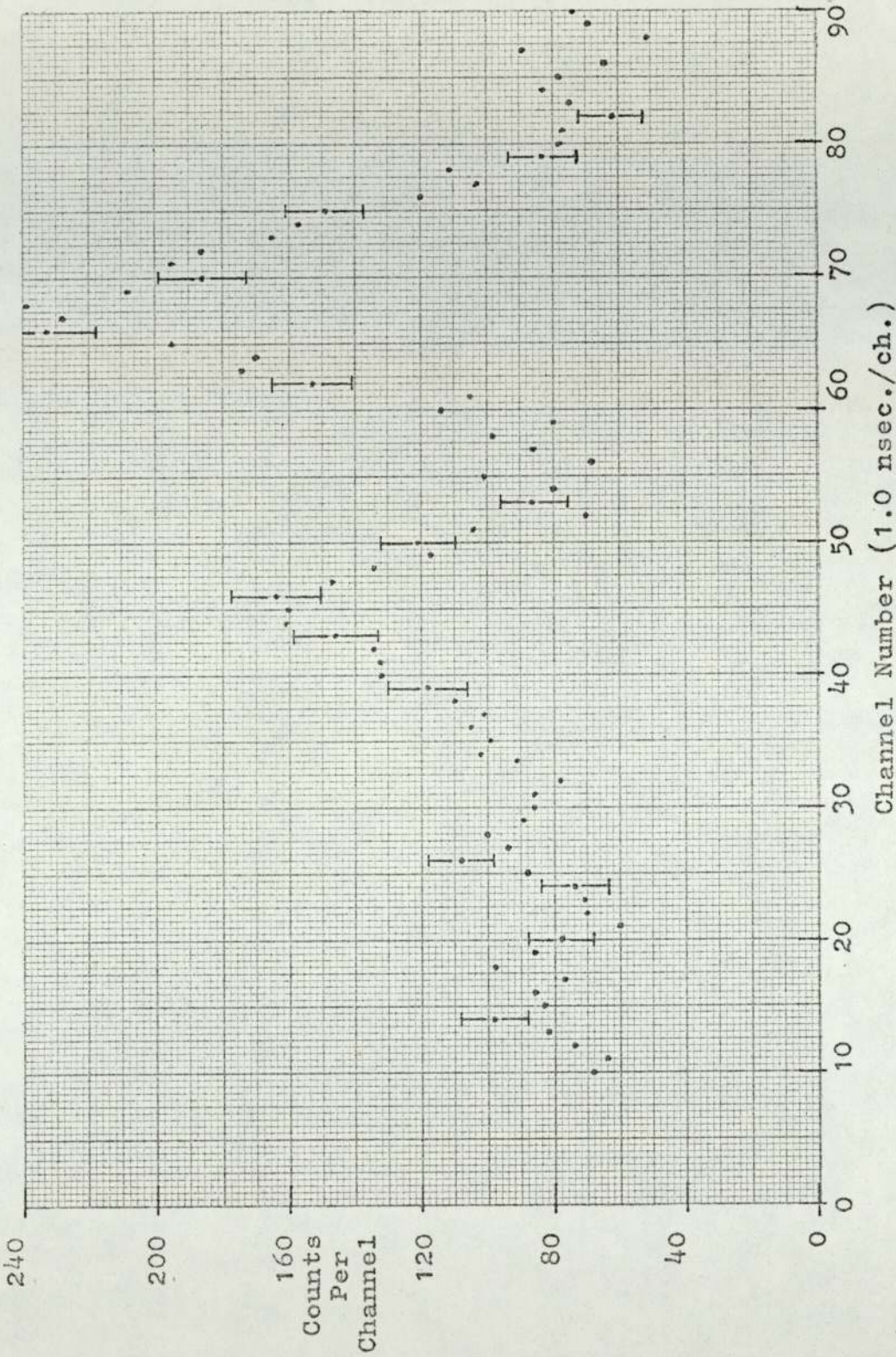
Figure 2.19   Time Spectrum from Silicon Sample using Original
Timing System.

(Gamma-Discriminator Level:1.0 MeV.)
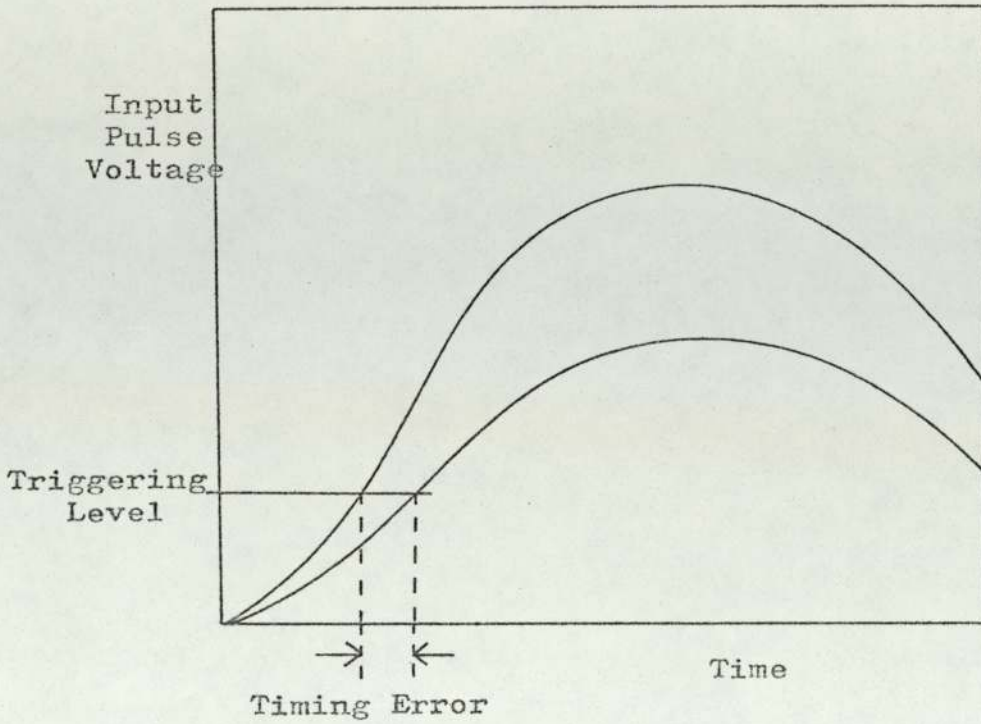
Figure 2.20   Timing Error Due To 'Walk!
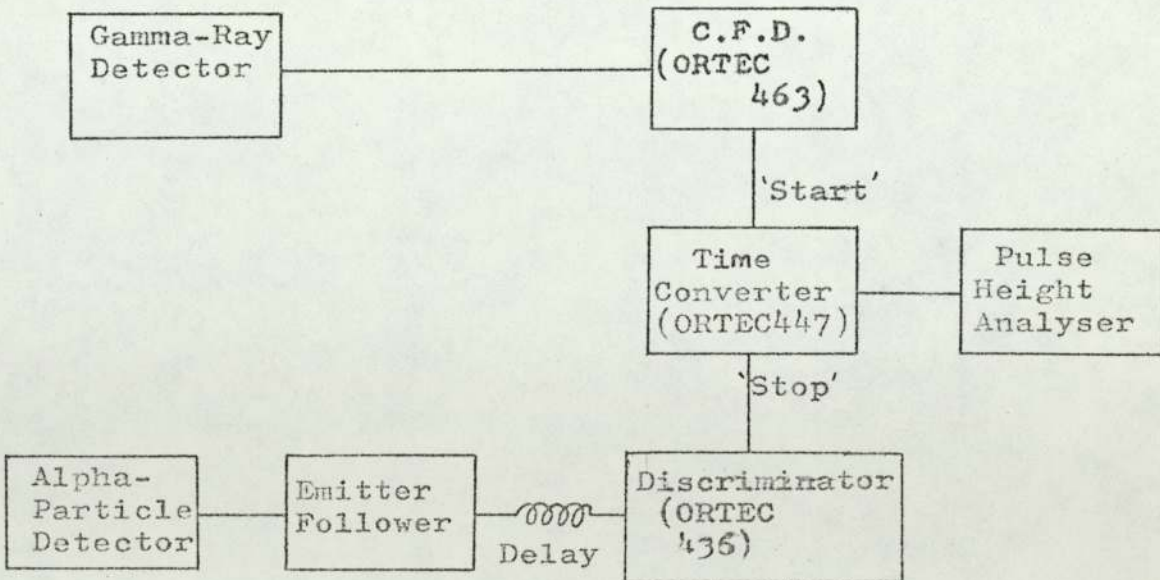
Figure 2.21   Time of Flight System.

the cable, and as it did not improve the time resolution, it was omitted. The ORTEC unit 463 incorporates a simple discriminator level and a constant fraction discriminator circuit. This triggers, as its name suggests, at a constant fraction, f, of the input pulse height, [46 - 48] where f is set to the value found experimentally to give the best resolution, ie. 0·2. "Walk" is almost entirely eliminated, as the circuit triggers on the same phase point on each pulse.

The alpha detector has not been altered, but to provide a timing pulse compatible with the input requirements of the new time to pulse height converter, (ORTEC 447), a fast discriminator, ORTEC 436, is now used in the alpha line. The ORTEC time converter can accept a much higher rate of input pulses than the original NE 6250 unit, (3 x 10^6 "start" and 3 x 10^7 "stop" counts sec^{-1}, compared with 25 x 10^3 counts sec^{-1}), so the slow coincidence gate is unnecessary. The gamma-ray pulse is used to start the time converter, as this line has a lower count-rate than the alpha-line, (10^4 sec^{-1}, compared with 8 x 10^4 sec^{-1}), so the dead time of the time converter is reduced, as are random coincidences.

The time resolution obtainable with this new system is shown in figure 2.22, which is a time spectrum obtained from a sample of silicon at a scattering angle of 30°. It can be seen that the F.W.H.M. of the gamma-ray peak is 4 nsec and the F.W.T.M. is 8·5 nsec. The pulses due to neutron detection form several peaks which are not resolved. The main peak is due to elastically scattered neutrons of 14 MeV, the smaller peaks are due to neutrons inelastically scattered from the various nuclear levels of the nuclei of the scattering sample.

The improvement in the F.W.T.M. from 20 nsec to 8·5 nsec is
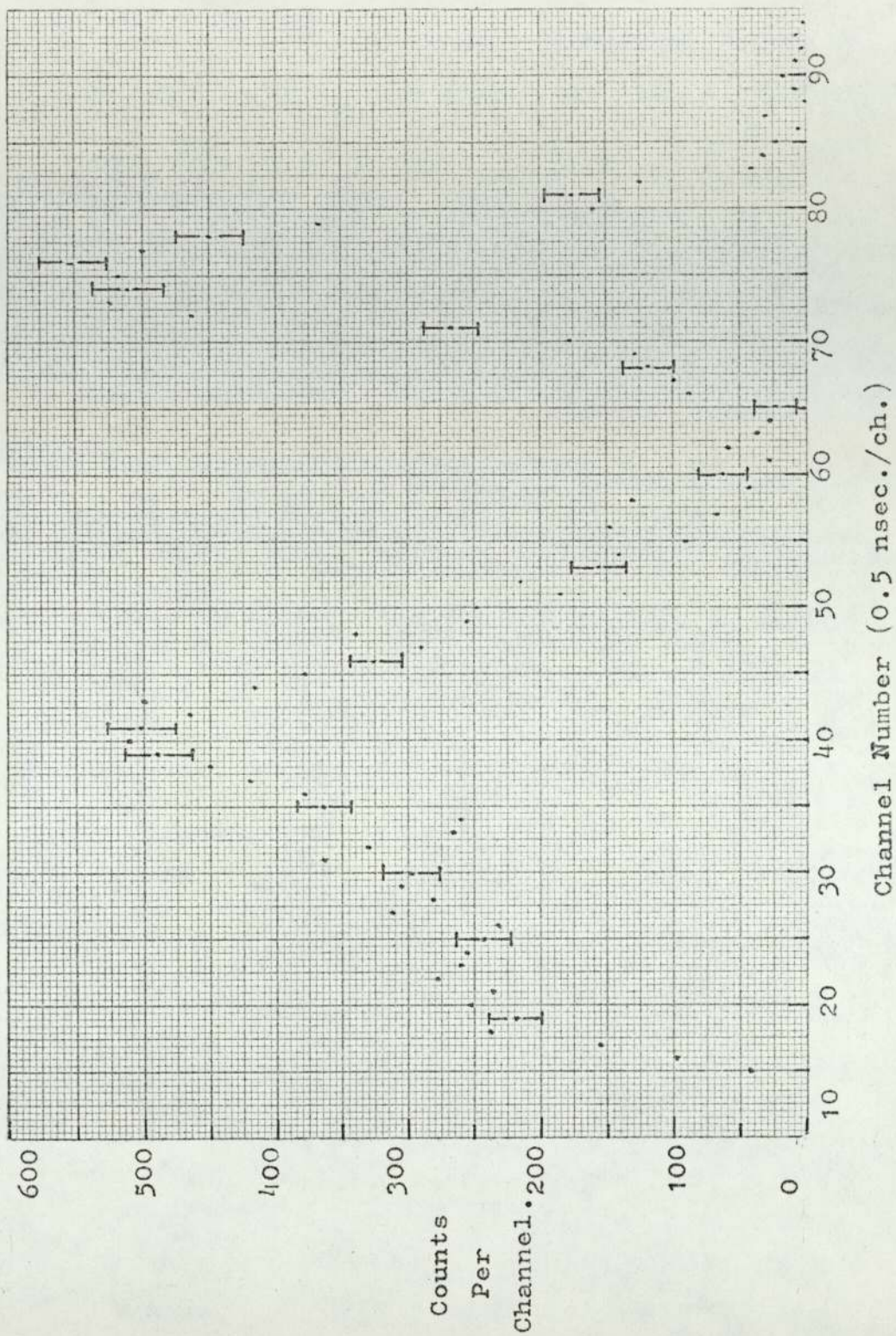
Figure 2.22 Time Spectrum from Silicon Sample.
(Gamma-Discriminator Level:1.0 MeV.)

particularly important as this determines the width of the "window"
set over the gamma-ray peak on the time spectrum. This is the
portion of the time spectrum which is passed by the single-channel
analyser. Pulses in this region pass through the analyser and then
gate the corresponding pulses in the energy line, allowing the
gamma-ray energy pulses to be stored in the energy spectrum
(figure 2.23). Reducing the width of this window obviously pro-
portionately reduces the number of background pulses in the time
spectrum which are allowed through the analyser, thus reducing
the background in the energy spectrum. However, the window must
not be reduced to the extent that a significant proportion of
the gamma-ray peak is lost. It is implicitly assumed in the
data analysis, that the efficiency of the gating circuit is 100%
for gamma-ray events; that is, if a gamma-ray is detected by the
scintillator, it is certain to be counted in the energy spectrum,
assuming the pulse height is great enough to pass the gamma-ray
discriminator level.

2.9.3. Sample-Detector Separation

This improvement in time resolution enabled the gamma-ray
detector to be moved closer to the scattering sample, reducing the
flight path travelled by the scattered neutrons and gamma-rays from
1·39 m to 0·78 m. This is the reason for the reduced separation
between the neutron and gamma-ray peaks in figure 2.22 compared
with figure 2.19. The neutron and gamma-ray peaks can still be
satisfactorily resolved with this reduced flight-path and the
increased solid angle subtended by the crystal means the count-
rate in the gamma-ray detector has increased by $(139/78)^2$ or
3·17.
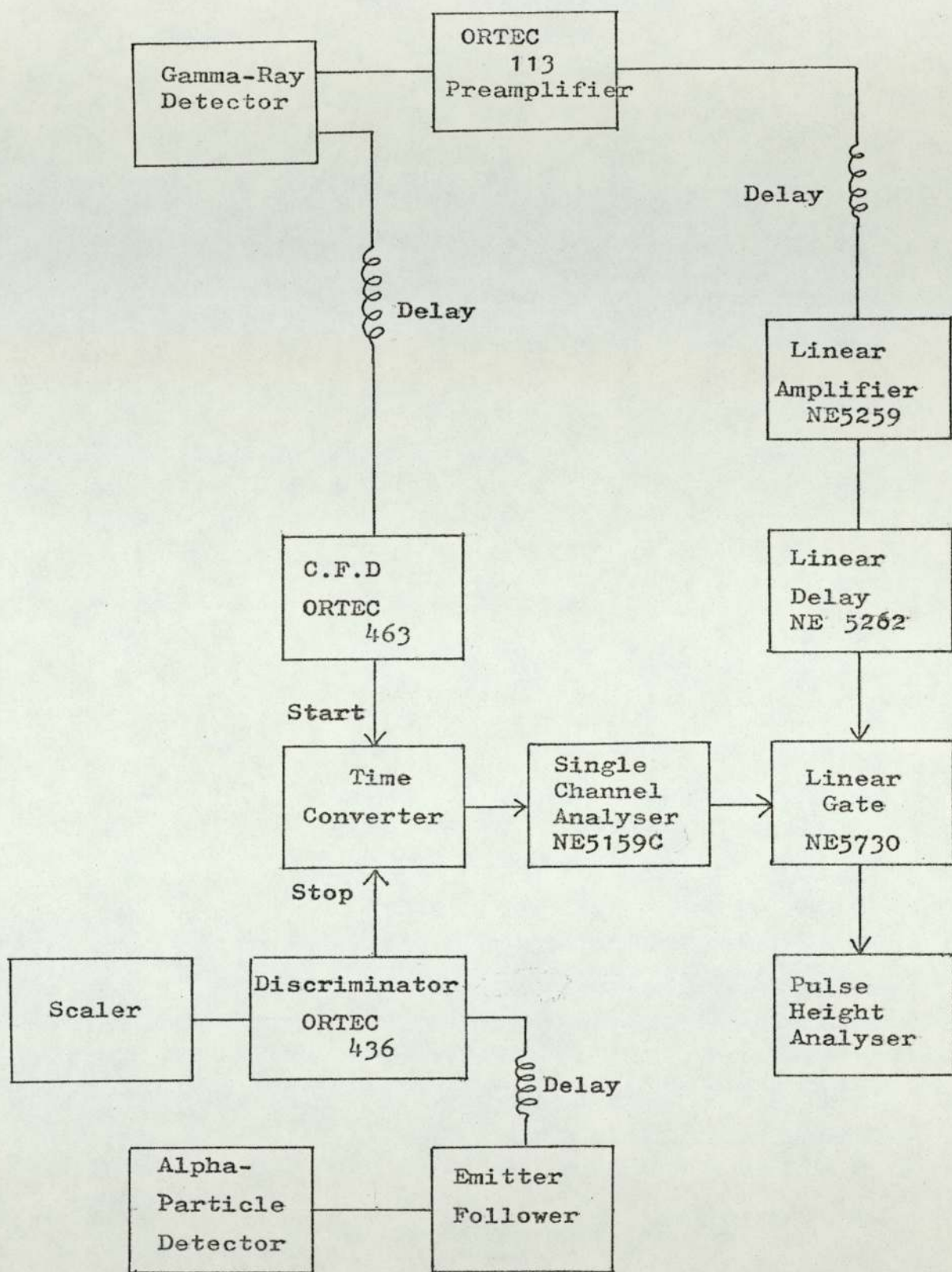
Figure 2.23   The Electronic System used to accumulate
             the Energy Spectrum.

2.10. Setting Discriminator Levels

The alpha-particle pulses are discriminated by a level fixed in the ORTEC 436 unit, to eliminate low energy noise, but to pass the pulses due to the 3 MeV alpha-particles from the $T(d,n)He^4$ reaction. The detector output is amplified (see figure 2.24), by a NE 5259 linear amplifier, and the resulting pulses gated by the output of the discriminator. As the discriminator level is increased, pulses below this level are not passed, and thus are not available to open the gate. The lower energy region of the spectrum is thus removed. The resulting spectra are shown in figure 2.25, both with the discriminator level set to zero and set to 0·365 volts. This level was left fixed throughout the whole of the subsequent work.

The gamma-ray discriminator level is set in a similar way to the alpha-level (see figure 2.26). This level is set at a value appropriate to the gamma-ray energies being investigated, that is, below the gamma-ray peak at the relevant energy, yet sufficiently high to remove the many low amplitude pulses due to neutron back-ground.

2.11. Energy Scale Calibration

Radioactive sources, listed in table 2, are used to calibrate the energy scale. The linear pulse for energy evaluation is taken from the 13th dynode, and matched into a cable by an ORTEC 113 preamplifier (figure 2.26). The pulses are then amplified by a NE 5259 spectroscopic amplifier with double differential shaping. The pulse-shaping time constants are chosen to give optimum energy resolution; the best values are found to be 1 μsec for both integrating and differentiating. The pulses are then gated, and
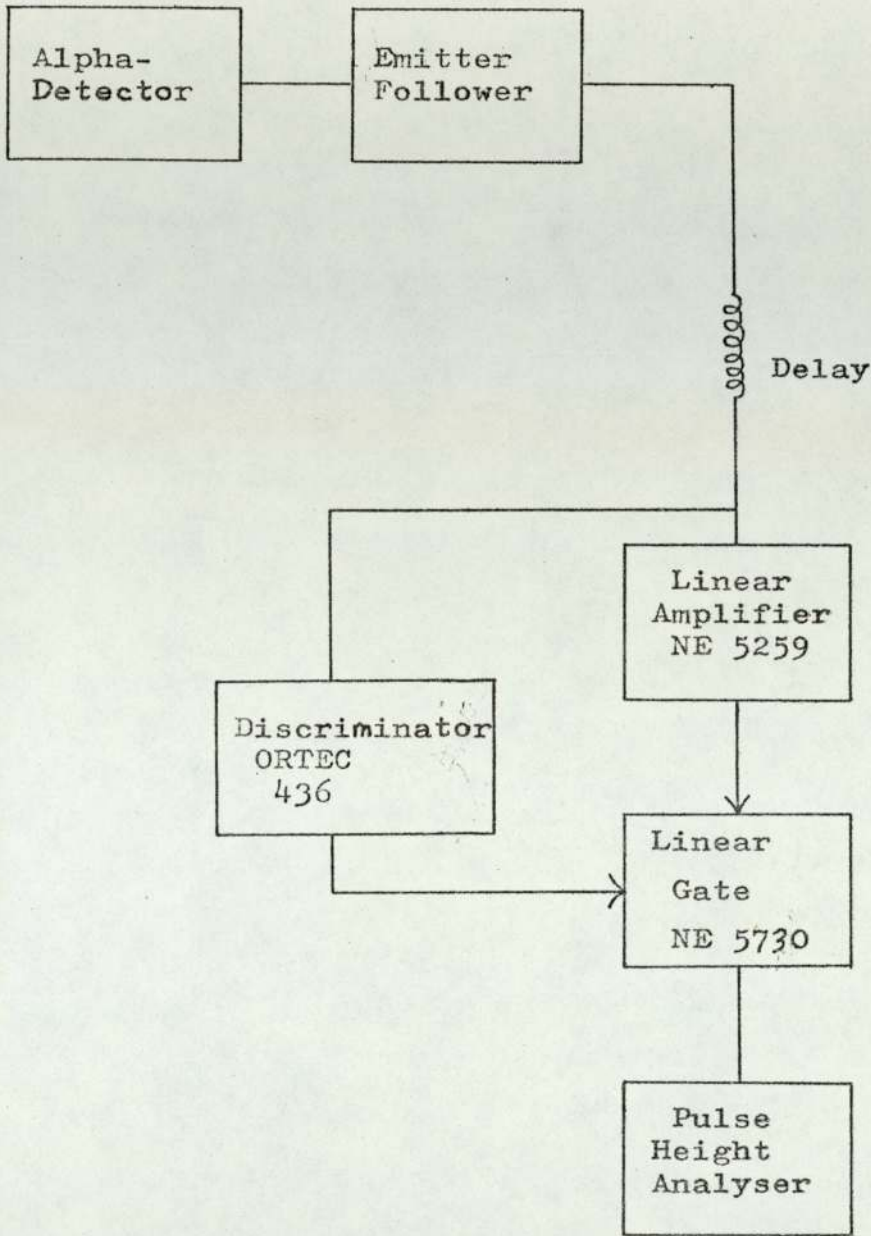
Figure 2.24   Setting of Alpha-Particle Detector
            Discriminator Level.
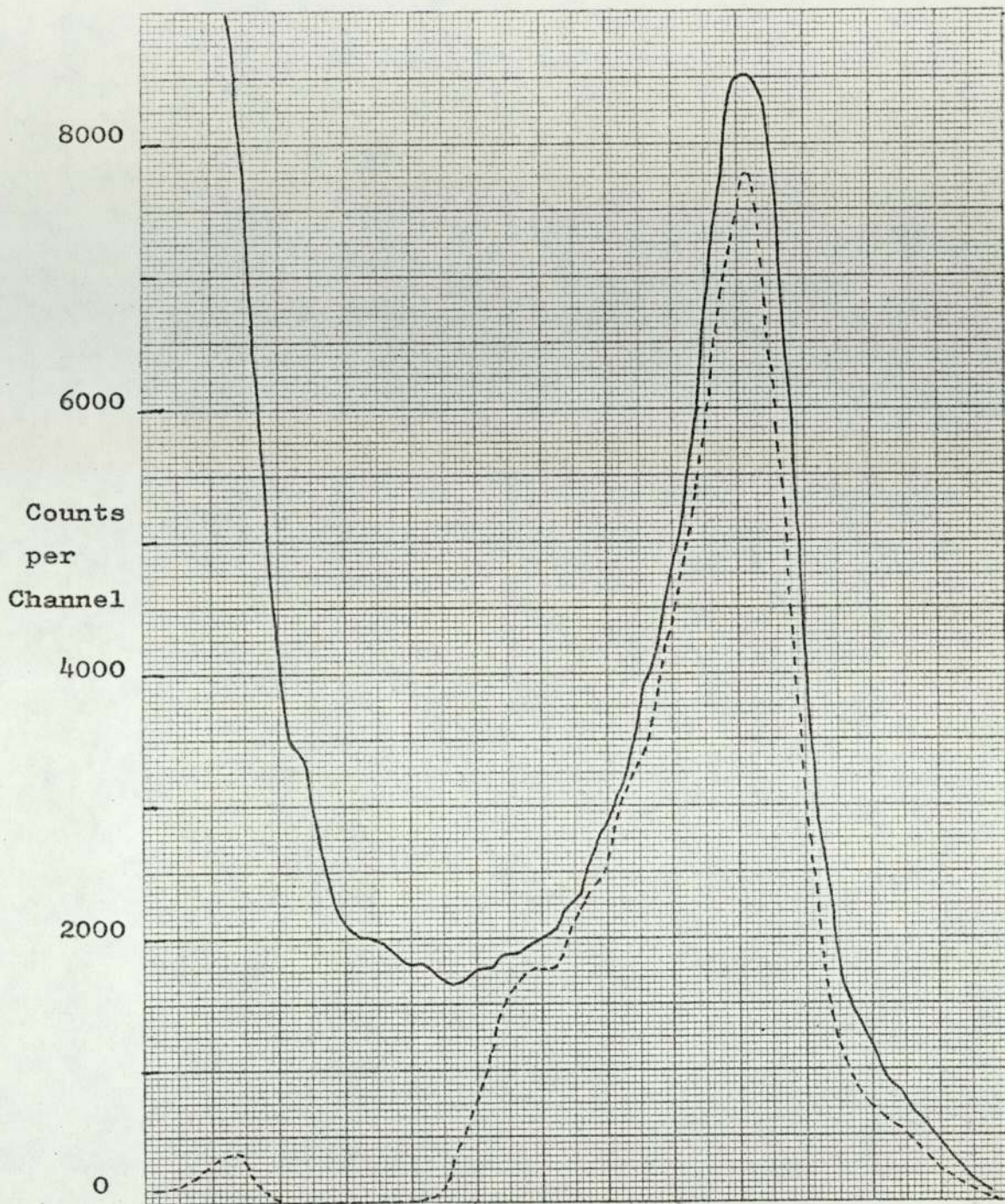
Alpha-Particle Energy.

Figure 2.25 Effect of Alpha Discriminator Setting.
_____ Undiscriminated spectrum

-------- Discriminated spectrum
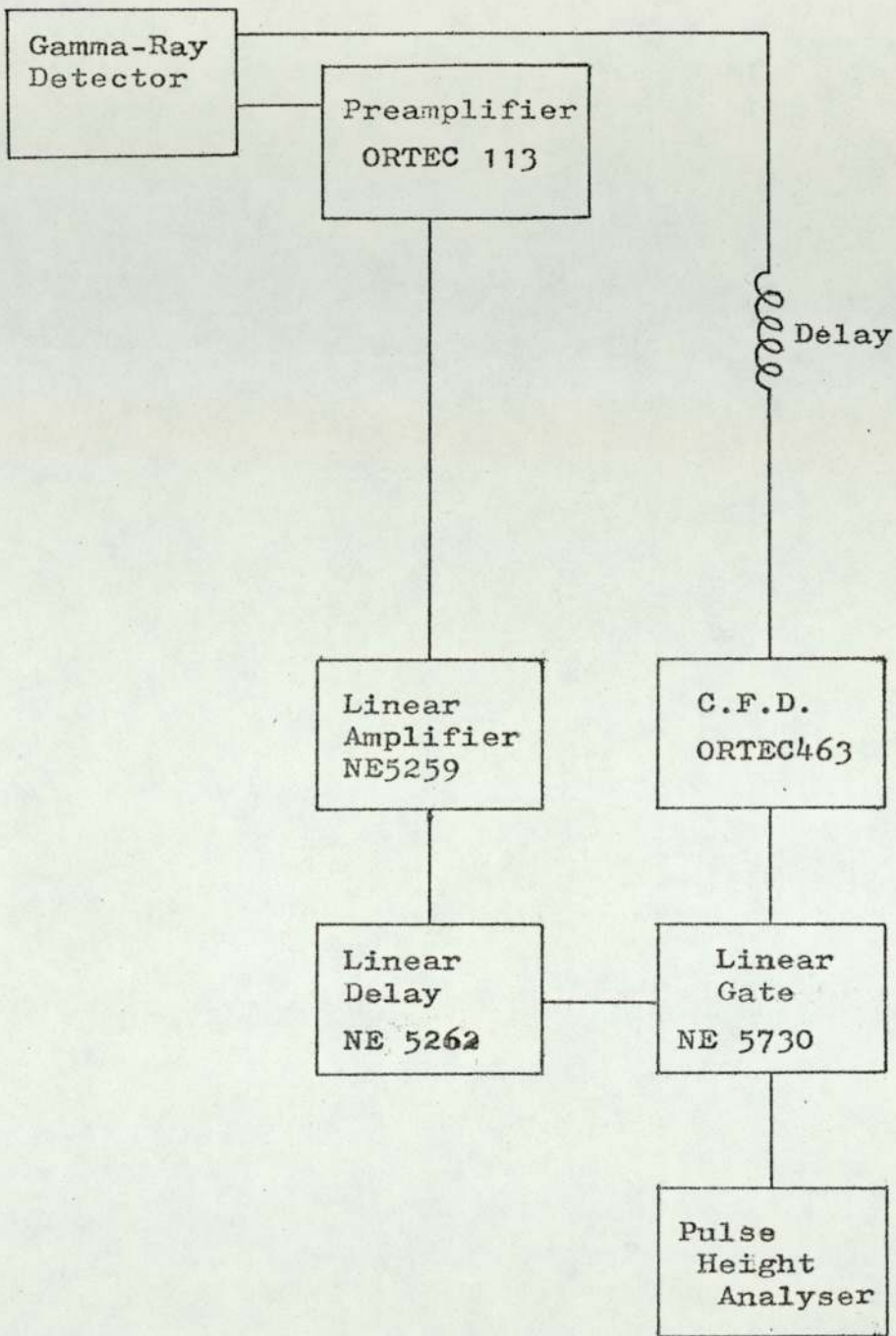
Figure 2.26 Setting of Gamma-Ray Detector
Discriminator Level.

analysed by the pulse height analyser. To calibrate the energy
scale, the discriminator level, on the ORTEC 463 unit, is set to
zero. A linear calibration was obtained, within the experimental
errors of 1%.

The delay unit NE 5262, and the linear gate NE 5730 should
not strictly be necessary for the calibration, as their specifi-
cations state that they do not affect the height of pulses being
processed by them. However, it is found that a slight decrease
in amplitude occurs, of approximately 5% in pulses passing through
these units. They are therefore included, so the energy scale
calibration takes account of these effects.

Isotope	Gamma-Ray Energy (MeV)
Cs^{137}	0·662
Mn^{54}	0·835
Na^{22}	0·511, 1·28
Co^{60}	1·173, 1·332
$A\ell^{28}$	1·78
Na^{24}	2·75

TABLE 2

Isotopes used for Energy Scale Calibration

The first four isotopes in table 2 are available as standard
sources, due to their comparatively long half-lives. The $A\ell^{28}$
isotope is produced by the reaction:

$$Si^{28} \ (n,p) \ A\ell^{28}$$
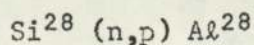
The Al^{28} decays by β^- emission to Si^{28}, with a half life of 2·3 mins. The Si^{28} decays to its ground state with the emission of the 1·78 MeV gamma-ray. Similary, the Na^{24} isotope is produced by neutron bombardment of Mg^{24}:-

$$Mg^{24} \ (n,p) \ Na^{24} \xrightarrow{\beta^-} Mg^{24}$$
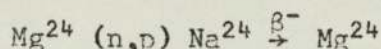
The Na^{24} half life is 15·0 hrs. The decay of Mg^{24} to its ground state produces the 2·75 MeV gamma-ray.

2.12. Energy Resolution

The energy resolution of a NaI scintillation detector is conveniently measured by the peak to valley ratio obtained in the energy spectrum of Co^{60} (figure 2.27). The original system employed a Phillips 56 AVP photomultiplier, which has a 51 mm (2") diameter photocathode. The photomultiplier was optically coupled to a 77 mm (3") diameter crystal by a 100 mm long converging light pipe of perspex. This system barely resolved the two Co^{60} peaks, giving a peak to valley ratio of 1·05 : 1 (figure 2.28).

The photomultiplier tube was replaced by a Phillips 58 AVP, which has a photocathode diameter of 110 mm. The light pipe was then unnecessary and was discarded, except that, as previously described, a plano-concave perspex plate was used to couple the convex surface of the photomultiplier glass case to the plane surface of the scintillator casing. This new system achieved a peak to valley ratio of 3·0 : 1 as shown in figure 2.28. This improvement is probably due to the better light collection efficiency of the new arrangement, and the fact that mainly the

Counts
Per
Channel

Peak

Valley

1.17   1.33

E_γ MeV.
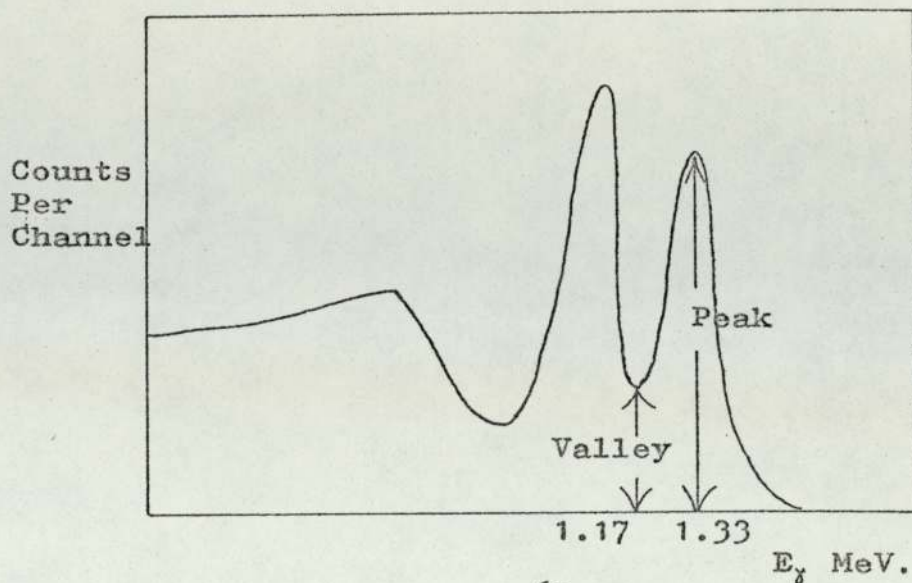
Figure 2.27   Sketch of Co^{60} Gamma-Ray Spectrum
to illustrate the P:V (peak to valley) ratio.

600

500

400

Counts
per   300

Channel

200

100

0

Gamma-Ray Energy.
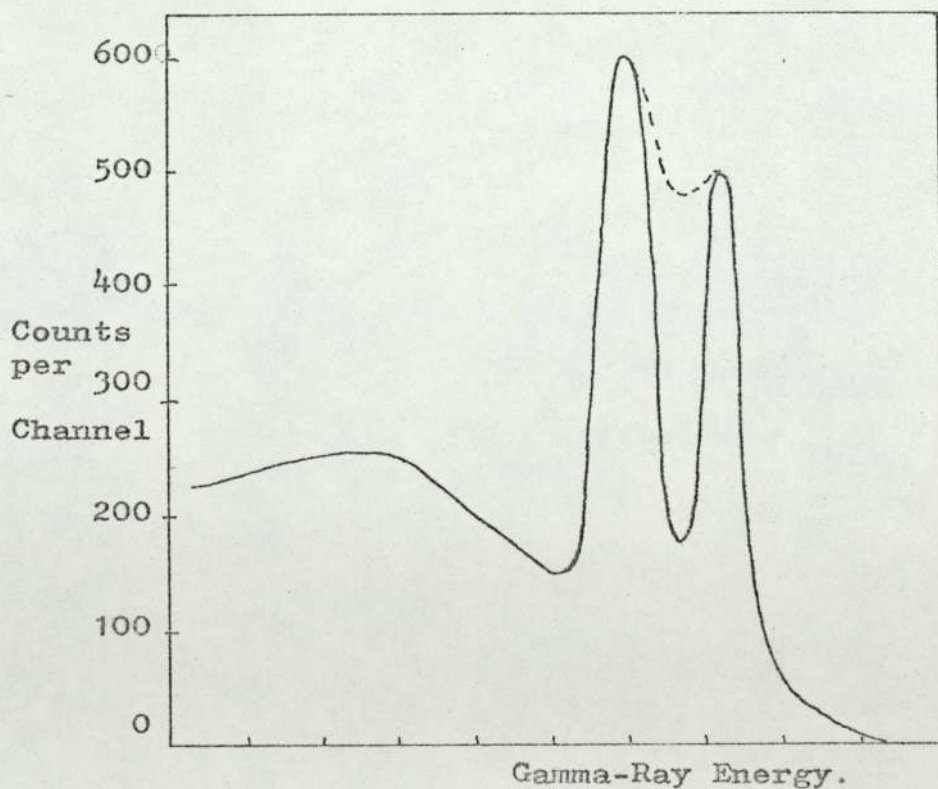
Figure 2.28   Improvement in Energy Resolution.

central region of the photocathode is now used, which generally
has a higher photoemission efficiency than the edges [42].

2.13. The Energy Spectrum

The complete electronic system used to accumulate the gamma-
ray energy spectrum is shown in figure 2.23. The output from the
time converter is passed to a single channel analyser (NE 5159C),
set so that only pulses in the gamma-peak produce output pulses
from this unit. Thus pulses due to scattered neutrons are cut
out and do not contribute to the background except in random
coincidences.

The measurements are obtained by counting alpha-pulses on
the scaler, and simultaneously accumulating the gamma-ray energy
spectrum on the P.H.A. This process is then repeated for the same
alpha total with the sample removed, to measure the background
spectrum. This procedure, which takes approximately 45 mins in
all, is repeated 2 - 4 times for each angle, depending on the
size of the differential cross-section at that angle, and the
relative amount of background present.

Previous experience warned that the gain of the system might
be unstable. This is therefore checked between each run. It is
found that the gain increases steadily throughout the day, resulting,
in a spectrum shift of about 5% over 10 hrs. Since the gain is
reset, if necessary, after each run, this shift does not affect
the results.

2.14. Conclusions

The main improvements which have been made to the system

are the following;

(a) Timing resolution has been improved from 10 nsec F.W.H.M. to 4 nsec,

(b) Resulting from (a), sample-detector distance has been decreased from 1·39 m to 0·78 m.

(c) The slit replaced the pinhole in defining the deuteron beam onto the target, allowing greater neutron yield while maintaining the beam stability.

(d) Energy resolution has been improved by a factor of 3.

Points (b) and (c) together can be seen to increase the rate of data accumulation by a factor of approximately 10. This means that long term instability of the equipment is not now serious, and not so much time is lost checking gain changes due to drifting of H.T. supplies etc. This improvement can be seen in the time taken to accumulate a gamma-ray energy spectrum of the required statistical accuracy. This has been reduced from 20 hrs [17] to 2 - 3 hrs.

It is also to be expected that due to point (d) the gamma-ray peaks will appear more quickly as they will be spread over fewer channels of the pulse height analyser. Point (a) implies that the random background should be reduced to half its previous value. This point is difficult to check accurately, as the spectra which have been measured during this work, have photopeaks at different energies from those measured by Connell [17], so they are not directly comparable. However as an approximate estimate, comparison of the 1·27 MeV peak in the gamma-ray spectrum of S^{32} [17]

with the 1·37 MeV peak of Mg^{24} (present work) indicates an
increase in the signal to background ratio at the peak centre
from 3·1 : 1 to 7·7 : 1. The energy range per channel of the
two spectra are respectively 44 KeV/ch and 41 KeV/ch. The dif-
ference in gamma-ray energy means that the comparison cannot be
exact, however, both gamma-ray detection efficiency and background
intensity decrease with the increasing energy scale, tending to
cancel as a first approximation. It can thus be seen that the
signal to background ratio has been improved by a factor of about
2.

These alterations imply that the lower limit of the differen-
tial cross-section which the system could be used to measure, is
reduced, from about 50 mb/str to about 5 mb/str, with the same
experimental errors and data accumulation time. The system has
not, in the present work, been used to measure such low cross-
sections because theoretical interest has centred on cross-sections
larger than this. However, the stability of the SAMES generator
would be the limiting factor in such a measurement of a low cross-
section.

3. DATA ANALYSIS

3.1. Form of Data

As described in the previous section (2.13), the raw experimental data is accumulated in the form of a gamma-ray energy spectrum, and the time-integrated total of associated alpha-particles detected during the period of measurement at each scattering angle. This data must then be analysed to derive from it the differential cross-section per unit solid angle, for production of the gamma-ray concerned.

3.2. The Differential Cross-Section

If there is a flux of n neutrons per sec, per unit area incident on the scattering sample, and g gamma-rays of specified energy E MeV, are produced, per second, in the sample, which contains N nuclei, then the total cross-section per nucleus for production of that gamma-ray is given by:-

$$\sigma_E = \frac{g}{n \, N} \qquad\qquad ..(3.1)$$

It can be seen that σ_E has units of area; it is conveniently measured in barns (1 barn = 10^{-28} m^2).

The differential cross-section per unit solid angle at a scattering angle θ is given by:-

$$\frac{d\sigma_E(\theta)}{d\Omega} = \frac{g(\theta)}{n \, N} \qquad\qquad ..(3.2)$$

where $g(\theta)$ is the number of gamma-rays produced per sec. into

unit solid angle, centred on the direction θ to the neutron beam.
(All measurements are taken in the horizontal plane). From
equation 3.2 it can be seen that $d\sigma/d\Omega$ has units of area / (solid
angle), usually mbarns/steradian. Examination of the gamma-ray
energy spectra permits the determination of the number of gamma-rays
of energy E_γ detected in the photopeak during the period of measure-
ment. Various possible sources of error have to be taken into
account; for example, partial detection of gamma-rays of higher
energy, or activation of the sample material. Also this photopeak
total, $P(\theta)$, must be corrected for the efficiency of the detector
(ε), and for the absorption of gamma-rays in the sample itself.
The correction factor for this effect is $S(\theta)$. The total of
associated alpha-particles, ϕ, gives a measure of the incident
neutron flux, here again correction factors (F) are necessary.
The differential cross-section is thus given by;

$$\frac{d\sigma_E(\theta)}{d\Omega} = \frac{P(\theta)}{\varepsilon S(\theta)(\phi/A)FN} \qquad ..(3.3)$$

here A is the area of the sample face on which the neutron flux is
incident.

These various factors will now be considered in detail,
leading to a discussion of the problems particular to each
element, which will be considered separately.

3.3. Gamma-Ray Energy Spectra

An example of a gamma-ray energy spectrum is shown in
figure 3.1, that of gamma-rays from magnesium at a scattering
angle of 40°. Several features of this spectrum may be noted,
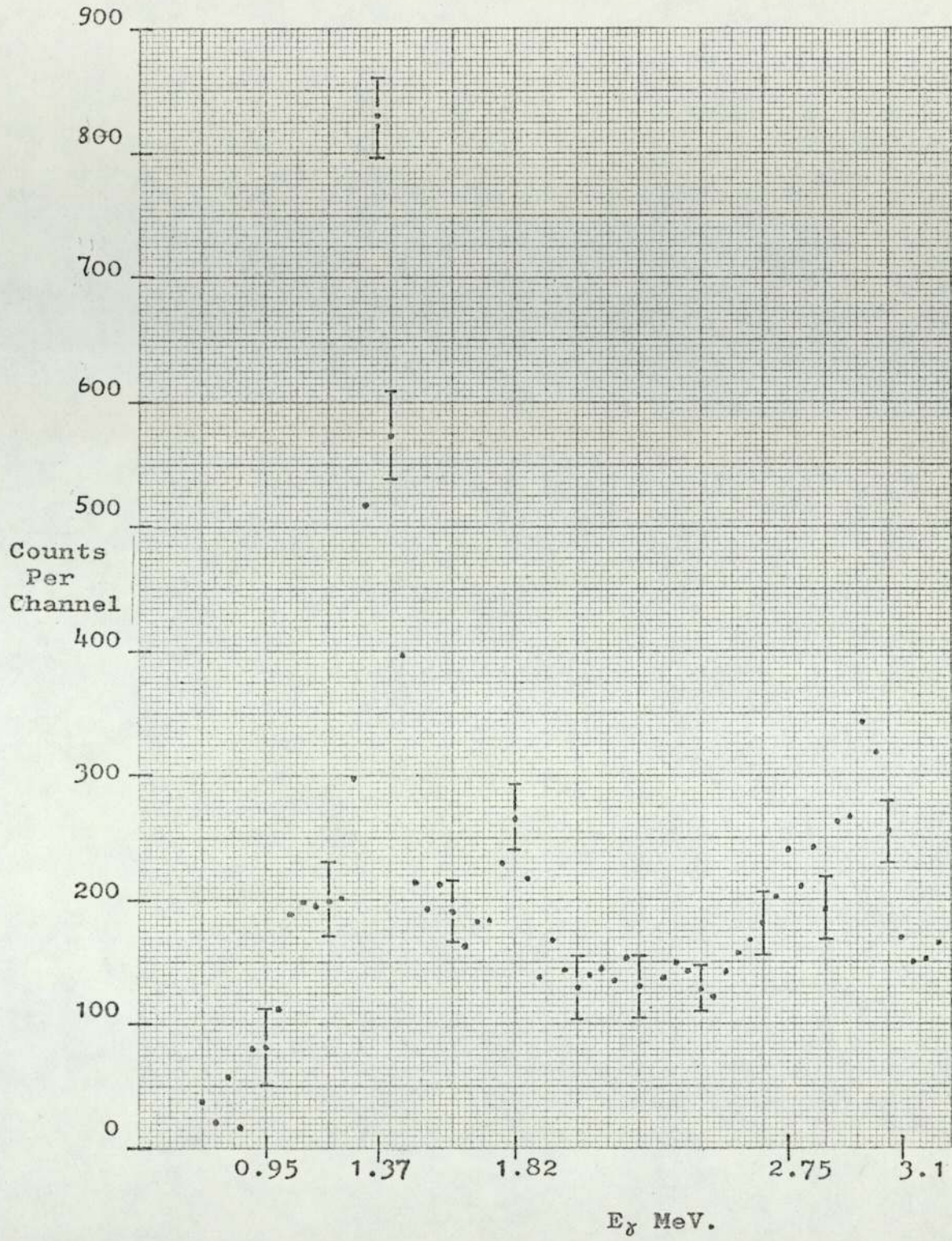
Figure 3. 1 Spectrum of Gamma-Ray Energies from
Magnesium.

to illustrate the problems involved in obtaining the number of
gamma-rays of a particular energy emitted by the sample at a
particular angle.

The gamma-ray discriminator level has been set above zero,
specifically at 0·95 MeV. As mentioned in section 2.10, this is
necessary to eliminate the high background count at low energies,
which produces an unworkable signal-to-noise ratio in this energy
region. The setting of this level means that the peak efficiency,
rather than the total efficiency must then be used (section 3.7).

The gamma-ray of interest is that of 1·37 MeV, which is
clearly resolved. Other gamma-ray energies are also detected,
a peak being resolved at 1·81 MeV. The 1·37 MeV photopeak is
situated on the Compton distributions due to the partial detection
of these higher energy gamma-rays. To obtain $P(\theta)$, the total
count in the 1·37 MeV photopeak, the counts under the photopeak
due to these Compton distributions must be accounted for. Various
methods for achieving this have been used.

One such method involves the subtraction from the spectrum
of the Compton distributions due to these other gamma-rays, a
process known as "spectrum stripping". In the present work, this
process cannot be carried out completely as there may be further
gamma-rays present, of energy greater than 3·0 MeV for which the
photopeaks are above the high energy end of the recorded spectrum.
Since the magnitudes of these photopeaks are unknown, the Compton
distributions accompanying them cannot be estimated. Also, some
of the photopeaks which are within the energy range of the spectrum
are not clearly resolved, and relative statistical fluctuations
are high. Errors in the "stripping" procedure increase as each

peak is removed, statistical uncertainties and the possibility of error in the spectral shapes accumulating with each subtraction.

An alternative to this procedure is the method of Covell [52]. This involves measuring a known fraction of the full peak count. As shown in figure 3.2, a line is drawn across the peak and counts above this line are noted. To find from this the total number of counts in the whole peak, $P(\theta)$, it is necessary to measure a reference spectrum. This must show the gamma-ray photopeak of the appropriate energy fully resolved, and with all background subtracted from the spectrum. Then the fraction of the total count which is above the corresponding line can be determined.

The sources of error involved in this procedure include the statistical uncertainties in the experimental and reference spectra, and the possibility of misplacing the base-line.

In the present case, Covell's method of measuring a calibrated fraction of the peak total is likely to yield a more accurate result for the photopeak total $(P(\theta))$, than the procedure of spectral stripping, and for this reason is preferred. This method is thus used to determine $P(\theta)$, from each spectrum.

3.4. The Neutron Flux

As mentioned above, the total count of associated alpha particles gives the number of neutrons incident on the sample, when certain corrections have been made.

3.4.1. Activation Background

The background count which is included in the measured
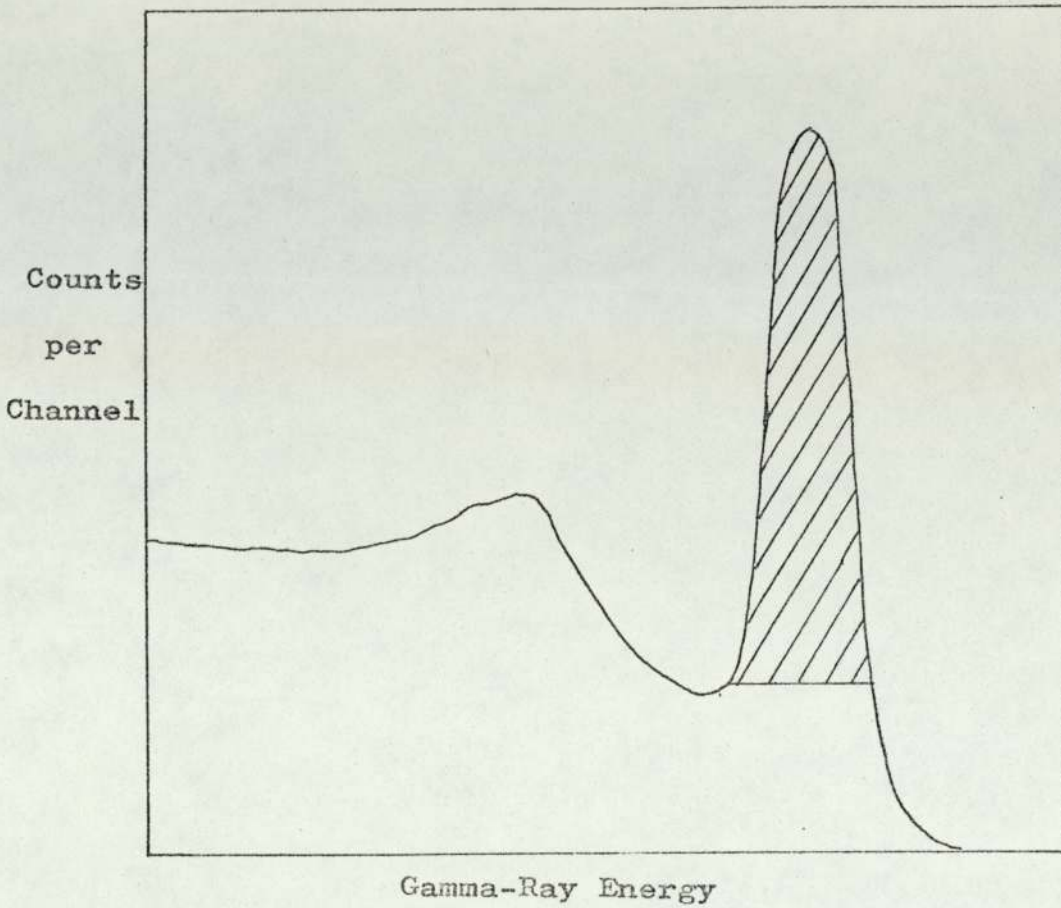
Gamma-Ray Energy

Figure 3.2   Sketch of Gamma-Ray Energy Spectrum
illustrating Covell's method$^{(52)}$.

Isotopes used for analysis;
For Mg^{24} ; Na^{24} (1.368 MeV)
    Cr^{52} ; Na^{24} and Y^{88} (1.367 and 1.836 MeV)
    Fe^{56} ; Mn^{54} (0.835 MeV)

total of alpha particles can be divided into two components. The
first consists of radiation produced by activation of the target
and surrounding assembly, caused principally by neutron reactions
of the type A(n,x)B. The materials used in the construction of
the target assembly are mainly iron, copper and zinc. The gamma-
ray spectrum produced by the target has previously been investigated
[17]. It was found to consist of peaks at 0·511 MeV, 0·85 MeV,
1·81 MeV and 2·12 MeV, superimposed on a continuous level dropping
from a high value at low energies, to zero at 3 MeV. The 0·511
MeV peak intensity decreases with a half life of approximately 10
mins, while the other peak intensities have half lives of several
hours. These peaks have been accounted for by the following
reactions:

$$Fe^{56} \ (n,p) \ Mn^{56} \ \xrightarrow{\beta^-} \ Fe^{56*}$$
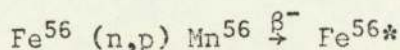
The (n,p) reaction has a cross-section of 110 mb, and the Mn^{56}
decays with a mean half-life of 2·6 hrs. The decay of the excited
states of Fe^{56} to the ground state then results in the emission of
the gamma-rays of energy 0·85 MeV, 1·81 MeV and 2·11 MeV.

Activation of copper and zinc takes place mainly by the
(n,2n) reaction, for example;

$$Cu^{63} \ (n,2n) \ Cu^{62} \ \xrightarrow{\beta^+} \ Ni^{62}$$
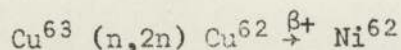
The cross-section for the (n,2n) reaction is 550 mb, and the
half life of Cu^{62} is 9·8 mins, which may correspond with the
half life of production of the 0·511 MeV gamma-ray. 99% of the
beta decay events go to the ground state of Ni^{62}, so few gamma-

rays are produced. The decay modes of the unstable zinc isotopes produced by the (n,2n) reactions are similar, also producing few gamma-rays.

This part of the background may be measured directly as it is present for some time after the deuteron beam has been switched off. The procedure used to account for this is thus to complete the measurement of the alpha-particle total, to note this figure, switch off the deuteron beam, then immediately restart the alpha-particle monitor, allowing it to count for 10 seconds. The background count-rate thus determined, usually in the range 1,700 ± 100 counts/sec., is used to correct the alpha total just measured. Since the alpha-particle count rate is in the range 80 to 90 Kc/s, this correction is of the order of 2%. Assuming that the background count-rate is constant throughout the period of measurement, the only error introduced by this correction is that due to statistical fluctuations, which are of the order of $\sqrt{1700}/80,000$, or 0·5%. Since the background count-rate is measured throughout the day, it can be seen that it does remain approximately constant, differences being less than the statistical uncertainties. This is true only after the deuteron beam has been switched on for some time to allow the activation to reach approximate saturation. For this reason the machine is always run for 90 minutes at the start of every day before measurements are taken.

3.4.2. Fast Background

The remainder of the background is due to direct reactions, and consists mainly of 14 MeV neutrons produced in the $T(d,n)He^4$ reaction which leave the target at 90° to the deuteron beam. This component of the background is produced only when the deuteron

beam is on, so it is not accounted for by the above procedure.
To measure this component, the deuteron beam is switched on, and
the alpha-count rate is monitored for various values of target
current in the range used. The beam is then switched off, and the
alpha-particle detector aperture plate (section 2.4) is replaced
by an aluminium plate without an aperture. The plate thickness is
1·0 mm, sufficient to stop 3·5 MeV alpha-particles, (range in
aluminium 0·017 mm [29]) but having a negligible effect on 14 MeV
neutrons. Only 1·6% of the neutrons interact in passing through
the plate. The count rate in the alpha-particle detector is again
measured for the same range of target currents.

It has thus been found that a fraction 0·055 of the alpha-
count consists of this background, and that the fraction is constant
over the range of target currents within ± 0·005. To correct for
this "fast" background the alpha-count is thus multiplied by the
correction factor F_1 which is 0·945 ± 0·005.

3.5. Neutron Absorption in the Target

Neutrons associated with detected alpha-particles must escape
the target assembly before reaching the scattering sample. To do
this they must pass through 2·50 mm of steel and 1·30 mm of water
(used to cool the target). These figures are taken from the manu-
facturers specifications. To calculate the fraction of neutrons
escaping the target, the cross-sections for neutron interactions,
excluding forward elastic scattering, for these materials are
needed. These have been found to be [17]:-

Iron	$\sigma = 2·316b$
Oxygen	$\sigma = 1·523b$
Hydrogen	$\sigma = 0·646$

The ffraction of neutrons escaping the target assembly, F_2, is thus given by:-

$$F_2 = \exp \left(- x_{Fe} \, \Sigma_{Fe} - x_W \, (\Sigma_H + \Sigma_O) \right) \qquad ..(3.4)$$

where $x_{Fe} = 2 \cdot 50$ mm $\pm$ $0 \cdot 03$ mm, $x_W = 1 \cdot 30$ mm $\pm$ $0 \cdot 03$ mm. Here the Σ_i are the macroscopic cross-sections excluding forward elastic scattering, and the x_i are the respective thicknesses.

The correction factor for absorption in the target it thus:

$$F_2 = 0 \cdot 939 \pm 0 \cdot 048$$

where the error is due mainly to uncertainties in the cross-sections.

3.6. Absorption of Gamma-Rays in Sample

Gamma-rays produced by neutron reactions in the sample may be absorbed before leaving the sample. The calculation of the correction for self absorption has been made elsewhere [17], but will be repeated here for clarity. The magnitude of the effect depends on the gamma-ray energy, and the nature of the sample, which determine the absorption coefficient for the gamma-ray in the material, and also on the sample geometry.

The neutron flux is assumed constant throughout the sample, as multiple scattering is assumed to cancel the effect of beam attenuation (section 3.10). Figure 3.3 shows the sample position in the horizontal plane of the neutron beam, which extends from 78° to 90° as described in section 2.6.4.
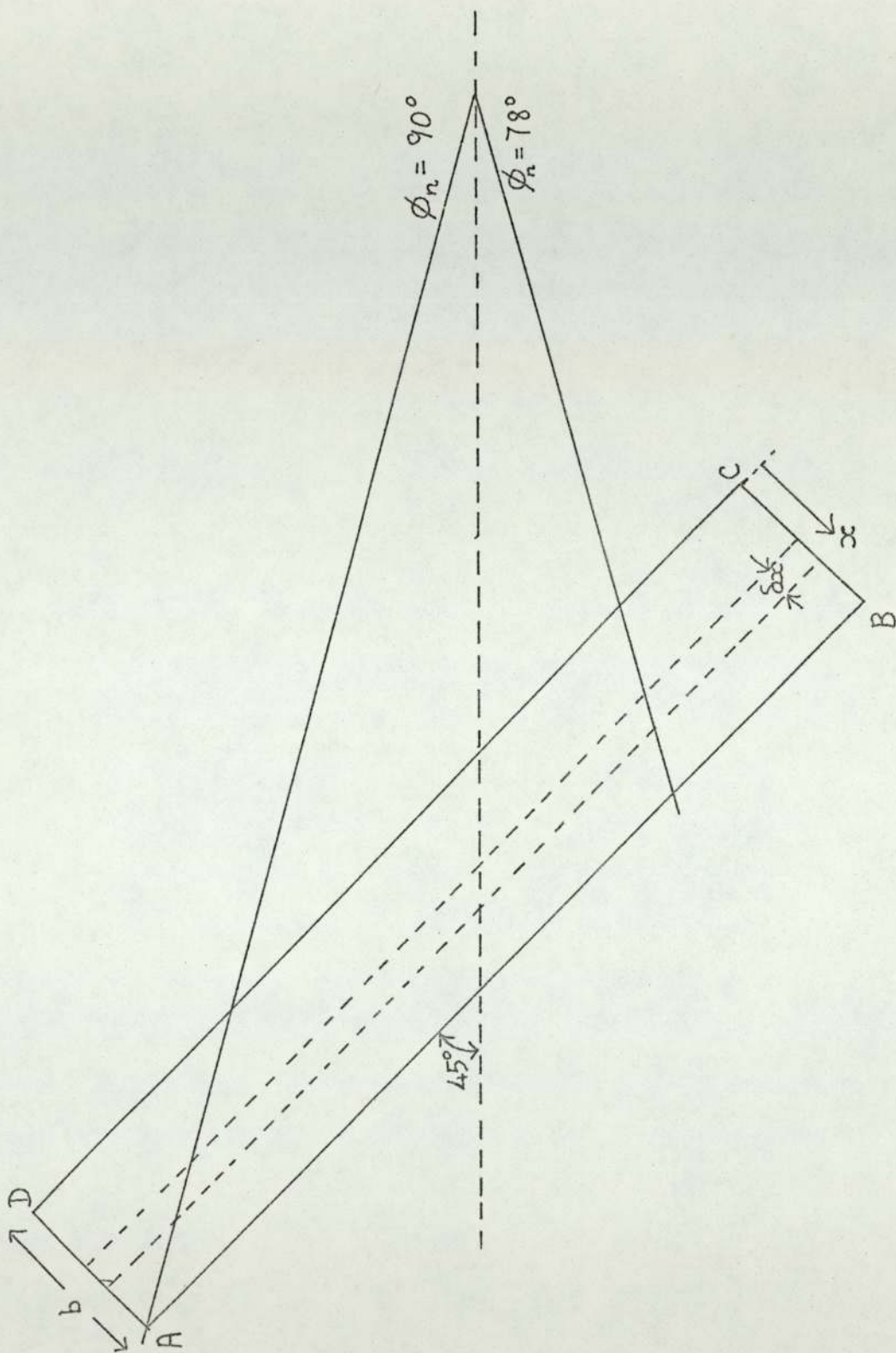
Figure 3.3 Calculation of fraction of gamma-rays escaping
the sample; not to scale.

The fraction of the total gamma-ray beam which is produced
in the elemental strip is $\delta x/b$. Assuming further that the
emerging gamma-rays which enter the detector form a parallel
beam, it is not necessary to consider any change in the scattering
angle, θ, over the length of the shaded strip. The fraction
of gamma-rays produced in the strip and escaping the sample,
through the face AB is thus;

$$S(\theta) = \exp\left(-\mu . \frac{b - x}{\cos(\theta - 45°)}\right) \frac{\delta x}{b} \qquad\qquad ..(3.5)$$

Here μ is the absorption coefficient, excluding coherent scat-
tering, for the gamma-ray of interest, in the sample material.
It is a function of the gamma-ray energy, and the sample Z
number. Integrating equation 3.5 over the width, b, of the
sample leads to;

$$S(\theta) = \int_0^b \exp\left(-\mu . \frac{b - x}{\cos(\theta - 45°)}\right) \frac{dx}{b} \qquad\qquad ..(3.6)$$

$$S(\theta) = \frac{\cos(\theta - 45°)}{\mu b} \left[1 - \exp\left(\frac{-\mu b}{\cos(\theta - 45°)}\right)\right] \qquad\qquad ..(3.7)$$

Thus $S(\theta)$ gives the fraction of the total gamma-ray yield produced
in the sample which escapes from the sample at the scattering angle
θ.

Consideration of this equation, 3.7, shows why the scattering
sample is placed at 45° to the neutron beam direction. This posi-
tioning ensures that the correction $S(\theta)$ has the minimum possible
variation, and the maximum possible value, over the range of
scattering angles 0° to 90°. If the sample had been placed

perpendicular to the neutron beam direction, gamma-rays escaping
at low scattering angles would traverse a comparatively short
distance in the sample, but gamma-rays escaping at 90° to the beam
would have to traverse the length of the sample. For intermediate
angles, part of the gamma-ray beam would escape through face AB
and part through BC of the sample making calculation of $S(\theta)$ com-
plicated. The sample width, in each case, is great enough to en-
sure that all the detected gamma-rays have left the sample through
face AB.

Equation 3.7 is evaluated at each value of the scattering
angle, θ, for which experimental measurements have been taken.
The value of μ is taken from the tables of Grodstein and Hubble
[53] for magnesium and iron, and the value for chromium is found
from the report of Storm and Israel [54]. In each case, inter-
polation is necessary to find the value of μ at the relevant
gamma-ray energy. Table 3.1 shows the relevant values of μ and
some typical values of the correction factor $S(\theta)$.

Sample	E_γ MeV	μ $\times 10^3$ m^2/kg.	$S(50°)$
Magnesium	1·37	5·552	0·8627
Chromium	1·43	4·952	0·8154
Iron	0·85	6·495	0·7984

TABLE 3.1

Absorption Coefficients and Typical Correction Factors for

Sample Materials

3.7. Efficiency of Gamma Detector

The number of gamma-rays detected in the peak of the gamma-

ray energy spectrum must be corrected for the effect produced by the fact that the gamma-ray detector is not 100% efficient.

The absolute gamma-ray detection efficiency $T(E_\gamma)$ is defined as that fraction of the total number of gamma-rays incident on the detector which interact with a finite energy loss in the crystal, and hence are detected, although not neces- sarily in the photopeak of the spectrum. In the present case, this is inappropriate as the total spectrum is not measured. Counts below the gamma-ray discriminator level (section 2.10) are not recorded.

The required correction factor is the peak efficiency ε, defined as that fraction of the total number of incident gamma- rays which deposit the whole of their energy in the crystal, and are thus recorded as counts in the photopeak of the gamma- ray energy spectrum. This may occur by the photoelectric effect, or by multiple scattering, followed by the photoelectric effect. The detection efficiency, however it is defined, depends on the gamma-ray energy as this governs the absorption coefficient in the NaI crystal, and on the sample-detector geometry. Rather than attempt the extremely complicated calculation of the peak efficiency, which should be done using Monte Carlo techniques, the efficiency was measured experimentally.

3.7.1. Measurement of Peak Efficiency

A gamma-ray source of strength S disintegrations per second emits into unit solid angle $\frac{S \ x \ (E\gamma)}{4\pi}$ gamma-rays per second of energy E_γ, where $x(E_\gamma)$ is the fraction of disintegrations which produce the gamma-ray concerned. If the spectrum of this source

is accumulated by the gamma-ray detection system for a time t seconds, and the spectrum then is found to have $P(E_\gamma)$ counts in the photopeak, then the peak efficiency is measured to be:-

$$\varepsilon(E_\gamma) = \frac{P(E_\gamma)}{t} \cdot \frac{4\pi}{S.x(E_\gamma)} \qquad ..(3.8)$$

Certified reference sources of known strengths, as supplied by the Radiochemical Centre, Amersham are used in the determination of ε. The source is placed on the sample stand, supported at the centre of the sample position by a small paper support which is assumed to introduce negligible scattering. The energy spectrum is accumulated using the experimental arrangement of figure 2.26 (section 2.10) with the discriminator level on the constant fraction discriminator (ORTEC 463) set as low as possible. The sources used for the measurement are shown in table 3.2 which gives the activities together with the uncertainties in the activities.

Isotope	E_γ MeV	Half Life		Activity μci	% Accuracy of Activity
Cs^{137}	0·662	30·0	yrs	10·29	3·7
Mn^{54}	0·835	303	days	12·32	3·7
Na^{22}	1·275	2·6	yrs	10·88	3·7
Co^{60}	1·173	5·26	yrs	11·11	1·9
Co^{60}	1·332	5·26	yrs	11·11	1·9
Y^{88}	1·836	108	days	10·62	5·0

TABLE 3.2

Reference Sources

These values for the activites, the source strength in microcuries,
(1 µċι = 3·700 x 10⁴ disintegrations per second), were measured on
1st January 1974, according to the manufacturers specifications.
Corrections are thus necessary to allow for reduction in the activity
since that date. The half-life for each isotope is also listed in
table 3.2, and the correction is made by multiplying the activity
by the factor exp $(-T/_\tau)$ where T is the time elapsed from the date
the sources were calibrated to the date when the efficiency was
measured, and τ is related to the half-life $t_{\frac{1}{2}}$ by:

$$\tau = \frac{t_{\frac{1}{2}}}{\ln 2} \qquad ..(3.9)$$

The corrected value of the activity is then used in equation 3.8.
The value of x is unity for each source, except for Cs^{137}, where
it has the value 0·935. This is because in the decay:-

$$_{55}Cs^{137} \xrightarrow{\beta^-} {}_{56}Ba^{137}$$
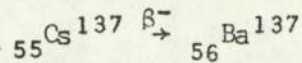
6·5% of the transitions go to the ground state of Ba^{137} so that no
gamma-ray is emitted. The remaining 93·5% decay to the $^{11}/_2{}^-$ state,
0·6616 MeV above the ground state, which then decays to the ground
state by emission of the 0·6616 MeV gamma-ray. No other decay modes
of this level are known [55].

The time taken for accumulation of the spectrum, t, is measured
on a calibrated stop watch with an estimated error of 0·2%. The
number of counts in the peak $P(E_\gamma)$ is found from the spectrum, cor-
rected for background, by completing the lower energy side of the
photopeak to be symmetrical with the high energy side, then adding
the counts in the peak on a desk calculator. Typically the error

due to statistical fluctuations is of the order of 0·5%. The

most important source of error in the determination of ε is

thus the uncertainty of the calibrated values of the activities

supplied by the manufacturer, and the other errors are not

considered further. Figure 3.4 shows the result of this measure-

ment, the variation of the peak efficiency of the gamma-ray

detector with incident gamma-ray energy. The curve has been

drawn by eye through the experimental points. This formulation

of the peak efficiency actually involves the ratio;

$$\varepsilon = \frac{\text{Total of counts in photopeak}}{\text{Total of gamma-rays emitted into unit solid angle}} \quad ..(3.10)$$

This definition includes the effect of the solid angle subtended

at the sample by the detector, so this need not be measured sepa-

rately.

3.8. Isotopic Abundance

The formula for the differential cross-section for gamma-ray

production, equation 3.3, involves the factor N/A, where N is the

number of nuclei of the relevant isotope in the sample, and A is

the area of the sample face upon which the neutron beam is incident

This factor can be written $N'x$, where N' is the number of nuclei

of the isotope in unit volume of the sample, and x is the sample

thickness. In all cases, the sample consists of the natural element

of which the isotope of interest forms only a part. Thus N' is

given by;

$$N' = \frac{N_o \rho I}{Aw} \quad ..(3.11)$$
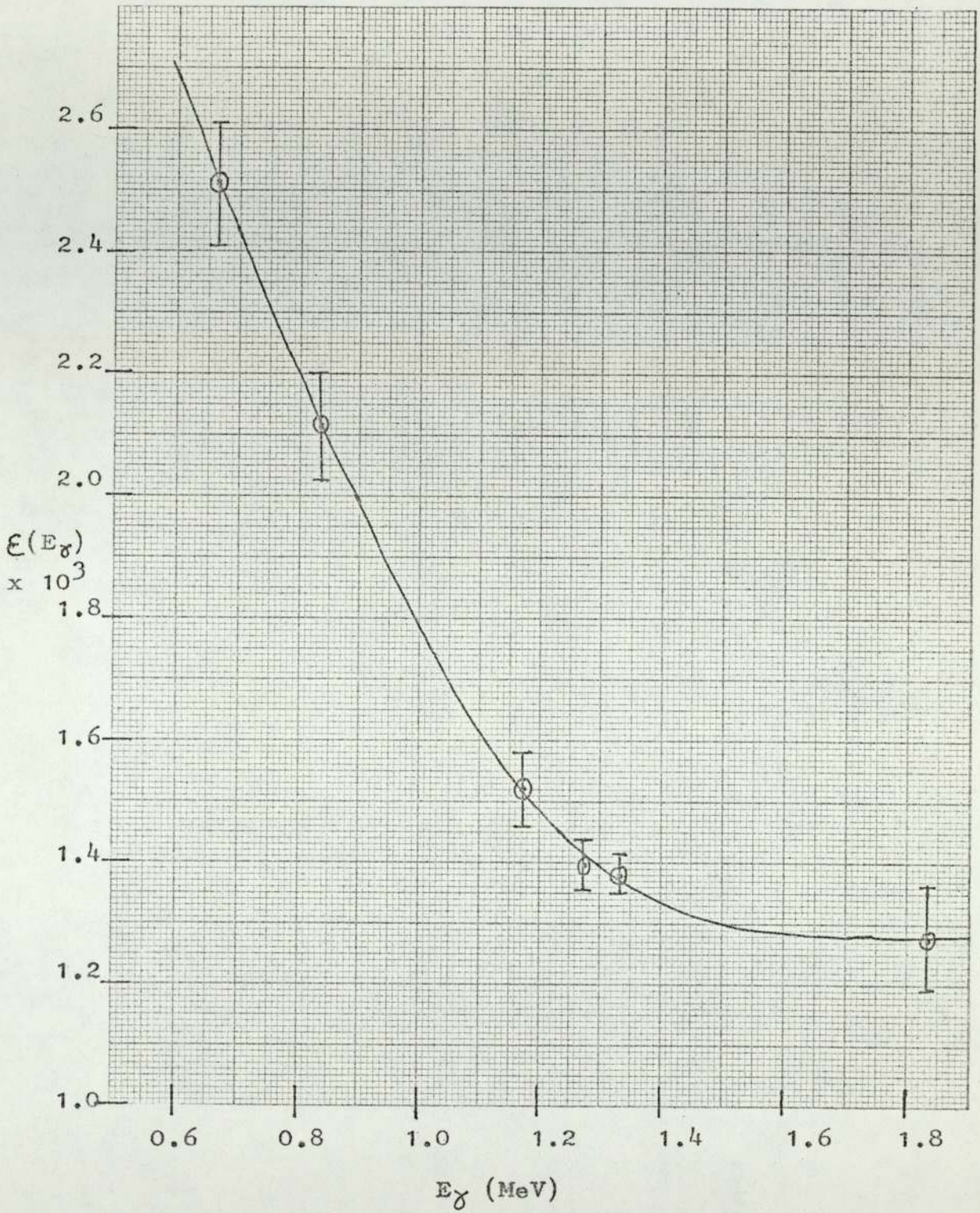
Figure 3.4 Efficiency of Gamma-Ray Detector.
(Curve drawn by eye through experimental points).

Here N_o is Avogadro's number, ρ is the density of the sample,
Aw is the atomic weight of the relevant isotope, and I is a
correction factor which accounts for the isotopic abundance of
that isotope. These fractional abundances, which have been
obtained from the Handbook of Chemistry and Physics [88], are
shown in table 3.3.

Isotope	Fractional Abundance (I)
Mg^{24}	0·7860
Cr^{52}	0·8376
Fe^{56}	0·9168

TABLE 3.3.

The factor I can be considered as correcting the density, ρ, so
that the value of Aw used is the exact atomic weight of this isotope
concerned, not the averaged value of the natural sample. Since
these abundance factors have been quoted to four significant figures,
it can be assumed that they are accurate to better than 1%. Errors
in N' are thus due mainly to uncertainties in the density.

3.9. Weighted Sample Thickness

The neutron beam incident on the scattering sample is not
parallel, but diverging, c.f. figure 3.3. The width of sample
material traversed by the beam thus differs at different values
of ϕ_n. The neutron beam profile (section 2.6.4) shows that the
relative intensity of the neutron beam also varies with neutron
angle. It is thus necessary to calculate the weighted sample
thickness $\bar{x}$, defined by;

$$\bar{x} = \frac{\sum_i f_i x_i}{\sum_i f_i} \qquad \qquad ..(3.12)$$

where i labels the values of the neutron scattering angle, ϕ_n, running from 77° to 93° in 1° steps. The weighting fraction, f_i, is proportional to the area under the beam profile curve, figure 2.11, in the 1° interval denoted by i. The value of the sample thickness, x_i, also depends on ϕ_n, the geometrical dependence is shown in figure 3.5. This sum has been performed using a desk calculator, the result being;

$$\bar{x} = (1 \cdot 610 \pm 0 \cdot 087)b$$

where b is the actual sample thickness. The error in this factor is composed of the estimated error in the neutron beam profile, of 5%, and possible errors in positioning the sample. An error of 1° in sample position results in a 2% error in the x_i. In practise, the sample could be positioned with an estimated accuracy of $\frac{1}{2}°$, (based on an error of 0·5 mm over half the sample width, 60 mm).

3.10. Multiple Scattering and Beam Attenuation

If the neutron flux incident on the sample is ϕ_o, then this flux may be expected to decrease in intensity with increasing penetration, x, of the sample, according to the exponential form;

$$\phi(x) = \phi_o \exp\left(-\frac{x}{\lambda}\right) \qquad \qquad ..(3.13)$$

Here λ is a constant of the sample material, specifically;

$$\lambda = \frac{1}{N'\sigma_\tau} \qquad \qquad ..(3.14)$$

$$\bar{x}_1 = \frac{b}{\sin(39° - \phi_n)} \qquad 84° \leqslant \phi_n \leqslant 90°$$

$$\vec{x}_2 = \frac{b}{\sin(51° + \phi_n)} \qquad 78° \leqslant \phi_n \leqslant 84°$$
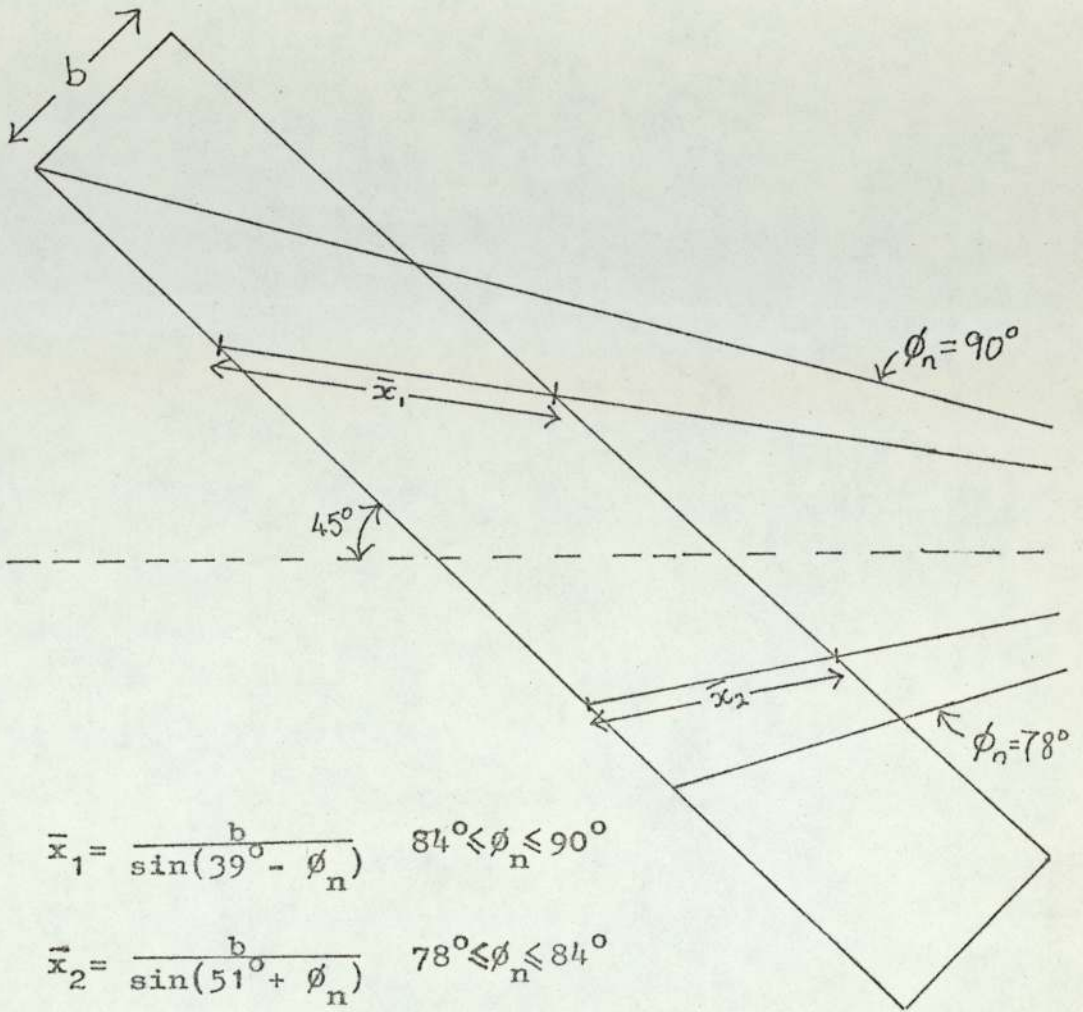
Figure 3.5   Calculation of the weighted sample
thickness, $\bar{x}$.

As before, N' is the number of nuclei per unit volume of the sample, and σ_τ is the total cross-section for neutron interactions, of any type, in the sample.

However, one of the most frequently occuring reactions of the 14 MeV neutrons in the sample is scattering, elastic or inelastic. While these processes remove neutrons from the beam travelling in the defined direction, the neutrons are still present in the sample and available for further reactions. Equation 3.13, thus underestimates the neutron flux present in the sample, leading to an overestimate of the cross-section for gamma-ray production. There is however, some attenuation of the neutron flux due to absorption of neutrons in reactions of the type; (n,p), (n,α), (n,γ) and so on.

An approximate method of dealing with this problem is to assume that, when transmission through the sample is greater than, or equal to, 70%, the beam attenuation is exactly balanced by multiple scattering, so that the neutron flux is constant throughout the sample. This implies that the probability of neutron absorption at a neutron energy of 14 MeV is equal to the probability of a neutron which has scattered once, scattering again off another nucleus. The calculation of the first factor is straight forward, depending on the cross-sections for the various reactions (n,p), (n,α) and so on. The second factor is much more complicated, depending not only on the total scattering cross-sections but on the angular distributions of the neutrons after scattering, and on the sample geometry. It is probable that this calculation would be most successful using Monte Carlo techniques.

However, this approximation, due to Day [34] has been checked

experimentally [18, 35] on various occasions, and has been found
to introduce less error than that due to experimental uncertain-
ties. For this reason, this assumption is made here. The neutron
flux throughout the sample is assumed constant at the value incident
on the sample face.

3.11. Reference Frames

To compare the experimental results with the theoretical
predictions, it is necessary to convert the scattering angle, θ,
which has been measured in the laboratory frame, to the centre of
mass frame. All theoretical calculations are carried out in the
centre of mass frame to avoid the complications of centre of mass
motion. It is thus convenient to convert the experimental data
to the centre of mass frame.

Considering the inelastic scattering event, as shown in
figure 3.6, in the laboratory and centre of mass frames res-
pectively. Then, comparing components of velocity,

$$v'' \sin \theta_{cm} = v' \sin \theta_L \qquad \qquad ..(3.15)$$

$$v'' \cos \theta_{cm} + v_{cm} = v' \cos \theta_L \qquad \qquad ..(3.16)$$

hence; $$\tan \theta_L = \frac{\sin \theta_{cm}}{\cos \theta_{cm} + v_{cm}/v''} \qquad ..(3.17)$$

as before; $$\gamma = \frac{v_{cm}}{v''} \qquad \qquad ..(3.18)$$

so that; $$\tan \theta_L = \frac{\sin \theta_{cm}}{\cos \theta_{cm} + \gamma} \qquad ..(3.19)$$

(i) Laboratory reference frame

-:-:-:-:-:-:-:-:-
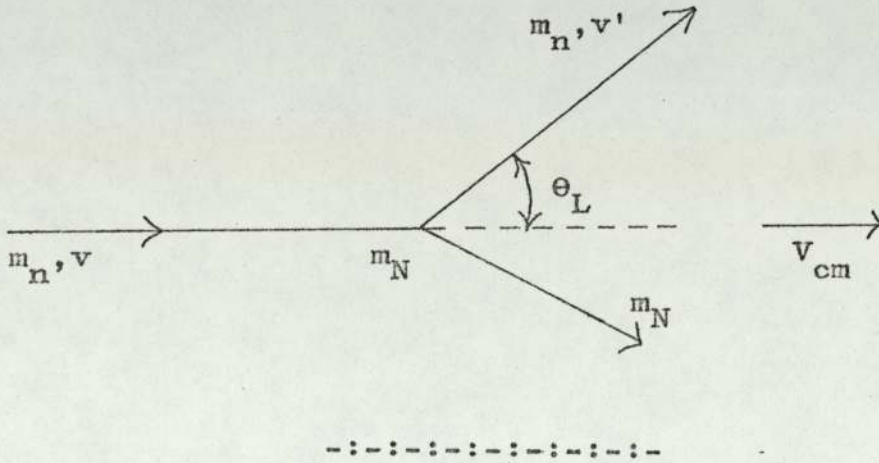
(ii) Centre of mass reference frame
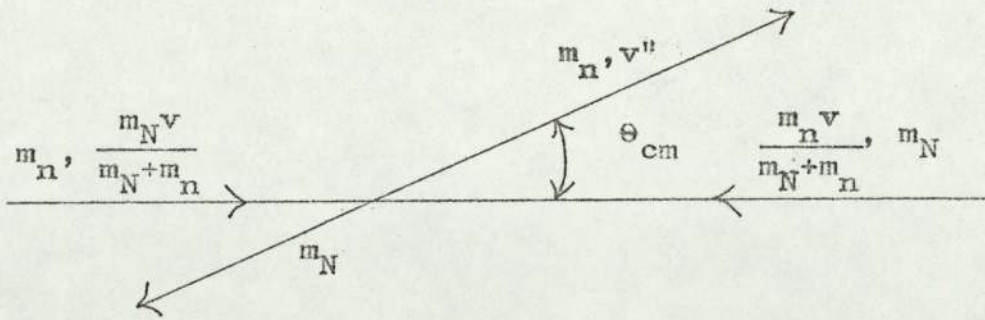
Figure 3.6   The scattering event in two reference
frames.

From the definition of γ, it follows that [56];

$$\gamma = + \left(\frac{m_n^2}{m_N^2} \cdot \frac{E}{E + Q}\right)^{\frac{1}{2}} \qquad \text{~~}(3.20)$$

Here m_n and m_N are defined in figure 3.6, E is the incident neutron energy, and Q is the difference between the initial and final values of the kinetic energy of the system;

$$Q = (K.E.)_f - (K.E.)_i \qquad \text{..}(3.21)$$

For elastic scattering, Q = 0 and $\gamma = m_n/m_N$, but for in-elastic scattering, Q is negative and equal to the value of the energy of the nuclear level which is excited. The value of Q is thus variable and unknown for a particular scattering event. The possible range of Q is from zero to -E, when the whole of the incident neutron energy is transfered to the nucleus. In this case, $\gamma = \infty$, as the neutron velocity after scattering is zero. However, the tranformation from the laboratory to the centre of mass frame (equation 3.19) is not very sensitive to the value of Q as can be seen from the following illustrative example. Consider the case of scattering from Mg^{24}, for θ cm = 45°. Calculating θ_L, for the two cases Q = 0 and Q = -13 MeV, gives the results;

Q = 0 ; $\qquad \gamma = \frac{1}{24} \qquad \theta_L = 43°\ 23'$

Q = -13 MeV ; $\qquad \gamma = \frac{\sqrt{14}}{24} \qquad \theta_L = 42°\ 1'$

The difference between these two extreme cases is thus seen to be 1° 22' much less than the angular resolution of the system.

For calculation of the transformation to the centre of mass frame, Q is thus set to zero.

It should be pointed out that although the transformation (3.19) is derived by application to the scattering angle of the neutron, it is generally applicable to any angle measured in the laboratory and centre of mass reference frames. It can thus be applied to the gamma-ray angle of emission, which is also measured relative to the neutron incident direction.

3.12. Activation of the Sample

Several alternative reactions can take place between the neutron and the target nucleus, apart from scattering. These reactions may lead to the emission of gamma-rays, which may then be accumulated as part of the gamma-ray energy spectrum.

One such reaction is the (n,p) reaction, which occurs for each of the elements concerned as shown in table 3.4.

Target Nucleus	Cross Section (mb)	Product Nucleus	Half Life	Gamma-ray Energies (MeV)
Mg^{24}	187	Na^{24}	15·0 hr.	2·754,1·368
Cr^{52}	116	V^{52}	3·76 min.	1·4336
Fe^{56}	160	Mn^{56}	2·576 hr.	2·110,1·811,0·847

TABLE 3.4.

(n,p) Reaction

Each product nucleus is unstable, decaying by β^- emission
to an excited state of the target nucleus, with the half-life
indicated. The target nucleus then decays to its ground state
producing the gamma-rays shown in the table. Only gamma-rays
produced in more than 5% of decays, are listed. These gamma-rays
are within the energy range of the spectra, and may therefore form
a source of error in the analysis of the spectra. The size of
this contribution will now be estimated.

Considering the general reaction;

$$X \ (n,p) \ Y \xrightarrow{\beta^-} X^*$$
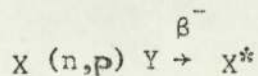
where the β^- decay occurs with time constant τ; then the number
of nuclei of Y produced per second, per unit volume of the sample
is $\phi n_x \sigma$, where ϕ is the incident neutron flux, n_x is the density
of nuclei of X, and σ is the cross-section for the (n,p) reaction.
This assumes that n_x remains effectively constant. It will be
shown later that this is the case. If n_y is the density of nuclei
of Y, then the rate of decay of Y is given by n_y/τ, so that [57],

$$\frac{dn_y}{dt} = \phi n_x \sigma - \frac{n_y}{\tau} \qquad \qquad ..(3.22)$$

Integration of this equation with the boundary condition $n_y = 0$
at $t = 0$, leads to;

$$n_y = \tau \phi n_x \sigma \ (1 - \exp \ (- t/\tau)) \qquad \qquad ..(3.23)$$

This expression gives the number of nuclei of Y present in the
sample, at a time t, after the start of the neutron bombardment

of the sample. However, the quantity required is n_d, the number
of disintegrations of Y which have occured in unit volume of the
sample during the time interval, t. This is given by;

$$n_d = \phi n_x \sigma t - \phi n_x \sigma \tau (1 - \exp(-t/\tau)) \qquad ..(3.24)$$

$$n_d = \phi n_x \sigma (t - \tau + \tau \exp(-t/\tau)) \qquad ..(3.25)$$

For the case $t \ll \tau$, the exponential term may be expanded,

$$n_d = \phi n_x \sigma \frac{t^2}{2\tau} \qquad ..(3.26)$$

and if $t \gg \tau$, then,

$$n_d = \phi n_x \sigma t \qquad ..(3.27)$$

If t is interpreted as the total duration of an experimental run,
then an average value of t is 45 mins. Considering the nuclei of
table 3.4, the condition $t \ll \tau$ is seen to be valid for Mg^{24} and
Fe^{56}, while for Cr^{52}, $t \gg \tau$.

Thus to determine the magnitude of the correction due to this
activation of the sample, equation 3.26 is evaluated for Mg^{24} and
Fe^{56}, while for Cr^{52}, equation 3.27 is used. The neutron flux, ϕ,
has the average value $8 \cdot 5 \times 10^4$ neutrons cm^{-2} sec^{-1}. The number
of β^- decay events, B, occuring in the sample during the period
of measurement is thus found.

In order that the gamma-rays produced in these decays may
be accumulated as part of the energy spectrum they must be in
random coincidence with a detected alpha-particle. If no

coincidence occurs, the associated particle discrimination system
will eliminate the pulses due to the detection of these gamma-rays.
If the efficiency for detection of the gamma-ray of energy E_γ is
$\epsilon(E_\gamma)$, then the number of gamma-rays due to (n,p) reaction , which
are detected in the gamma-ray energy spectrum is;

$$n_\gamma = B\phi_\alpha t_R \epsilon(E_\gamma) \qquad \qquad ..(3.28)$$

assuming that every decay produces the gamma-ray of energy E_γ.
The alpha-particle count rate, ϕ_α, is $8\cdot5 \times 10^4$ sec^{-1}, and the
resolving time of the coincidence circuit, t_R, is equal to the
gamma-ray "window" on the time spectrum, 10 nsec. The values
obtained for n_γ are $0\cdot2$, $0\cdot8$ and $1\cdot0$ respectively for Mg^{24}, Cr^{52},
and Fe^{56}, at gamma-ray energies of $1\cdot368$ MeV, $1\cdot4336$ MeV, and
$0\cdot847$ MeV. These figures are to be compared with the total number
of counts in the photopeaks of the respective energy spectra, $\sim$
2000. This shows that although the (n,p) cross-sections are
comparable with those for scattering, the contributions due to
(n,p) reactions in the gamma-ray energy spectra are negligible.
Similar reasoning shows that other reactions which produce gamma-
rays by activation of the sample are also negligible.

Referring to the earlier assumption that the density of
target nuclei, n_x, remains effectively constant during activation,
this can be justified by the following consideration. The maximum
value of n_y occurs at saturation when;

$$n_y = \phi n_x \sigma \tau$$

Considering the case of Cr^{52}, using values given previously,

$$n_y \approx 10^{-15} \, n_x$$

Since n_y is so much less than n_x, obviously n_x is effectively constant.

3.13. Reactions In The Detector

Gamma-rays, which have been produced by neutron interactions in the NaI crystal used as the gamma-ray detector, may be accumulated in the energy spectrum. When the scattering sample is in position, this forms a source of scattered neutrons of varying strength at various scattering angles. The neutrons which are scattered, elastically or inelastically, into the crystal, may cause interactions leading to the production of gamma-rays. If these interactions take place immediately, within a time period of less than the resolving time of the system, 10 nsec, the resulting gamma-rays will not be eliminated by the time of flight discrimination system, and will thus be accumulated. Inelastic scattering in iodine, specifically I^{127}, results in gamma-rays of comparatively low energy (less than 0.7 MeV), which are below the discriminator level for all of the elements considered, and hence may be neglected. Inelastic scattering in Na^{23} produces higher energy gamma-rays, for example 1.27 and 1.63 MeV, which are above the discriminator levels. When the sample is not in place, during the background subtraction runs, the scattered neutrons are no longer incident on the NaI crystal, so these interactions no longer occur. Thus the contributions due to these gamma-rays are not subtracted.

The size of this contribution may be estimated by the following consideration. Applying equation 3.2 to neutron

scattering in the sample, the rate of production of scattered

neutrons into unit solid angle is;

$$\phi_n = nN \left(\frac{d\sigma_n}{d\Omega}\right) \qquad \qquad ..(3.30)$$

where n and N have previously been defined and $d\sigma_n/d\Omega$ is the

differential cross-section for neutron scattering. Then, assuming

that gamma-rays produced in the crystal are detected with the same

efficiency as found in section 3.7, apart from the geometrical

factor 4π, then the number of gamma-rays detected per second,

which arise from neutron inelastic scattering in the NaI crystal,

P_c, is;

$$P_c = \frac{\phi_n}{A_c} \Omega N_c \sigma_c \epsilon_c \qquad \qquad ..(3.31)$$

Here A_c is the area of the crystal, Ω is the solid angle subtended

by the crystal at the sample, N_c is the number of sodium nuclei

in the crystal, σ_c is the total cross-section for Na^{23} for the

production of the relevant gamma-ray, and ϵ_c is the efficiency of

detection of this gamma-ray in the crystal.

From equation 3.3, the number of detected gamma-rays per

second which arise from neutron inelastic scattering in the

sample, P_s, is;

$$P_s = \frac{\phi}{At} FN \frac{d\sigma_\gamma}{d\Omega} \epsilon_s S \qquad \qquad ..(3.32)$$

where t is the period of measurement. To compare P_s and P_c

it is assumed that the cross-section for gamma-ray production

by 14 MeV neutron inelastic scattering is equal in the sample

material and in the sodium of the crystal; this is true to within a factor of 2 [58]. Thus, approximately,

$$4\pi \frac{d\sigma_\gamma}{d\Omega} = \sigma_c \qquad \qquad ..(3.33)$$

Reference to figure 3.4 shows that the efficiency does not change appreciably over the range 1·27 to 1·63 MeV, so, again approximately,

$$4\pi \, \varepsilon_c = \varepsilon_s \qquad \qquad ..(3.34)$$

Also, by definition,

$$n = \frac{\phi F}{At} \qquad \qquad ..(3.35)$$

and if r is the separation of the sample and the crystal,

$$\Omega = \frac{A_c}{r^2} \qquad \qquad ..(3.36)$$

Combining these relations in equations 3.31 and 3.32,

$$\frac{P_s}{P_c} = \frac{S \, r^2}{N_c \frac{d\sigma_n}{d\Omega}} \qquad \qquad ..(3.37)$$

From section 3.6, a typical value of S is 0·8. The value of r is 78 cm, and a typical value of $d\sigma_n/d\Omega$ is 50 mb/str. N_c is found from the crystal density and volume. Inserting these figures in equation 3.37 gives the result:

$$\frac{P_s}{P_c} \approx 10^4$$

It is thus seen that the contribution to the gamma-ray energy

spectrum from reactions in the NaI crystal is negligible.

3.14. Treatment of Data

The gamma-ray yield from the sample into unit solid angle
at the scattering angle θ, is seen from the above considerations
to be given by $P(\theta)/\epsilon(E_\gamma).S(\theta)$, where the terms have been defined
in sections 3.2, 3.7 and 3.6 respectively.

The integrated neutron flux incident on the scattering
sample, over the period of measurement, is also seen to be
$\phi(\theta)F_1F_2$. The differential cross-section per nucleus, for the
production of the gamma-ray of energy E_γ is thus,

$$\frac{d\sigma(\theta)}{d\Omega} = \frac{P(\theta)}{\epsilon(E_\gamma).S(\theta).\phi(\theta).F_1.F_2.N!\bar{x}} \qquad ..(3.38)$$

Here all the terms have been previously defined. This is the
formula which has been used to determine the differential cross-
section for production of the gamma-ray of energy E_γ, from the
raw experimental data.

The differential cross-section measurements are then fitted
by an equation of the form;

$$\frac{d\sigma(\theta)}{d\Omega} = a_o + a_2 P_2 (\cos \theta) + a_4 P_4 (\cos \theta) \qquad ..(3.39)$$

where $P_n(\cos \theta)$ is the Legendre polynomial of degree n. This
form of expansion is used as it is predicted by the theory
developed in chapter 4. Since the even order Legendre poly-
nomials are functions of $\cos^2\theta$, it is possible to express
equations 3.39 as a power series in $\cos^2\theta$, that is;

$$\frac{d\sigma(\theta)}{d\Omega} = b_o + b_2 \cos^2\theta + b_4 \cos^4\theta \qquad \qquad ..(3.40)$$

The analysis required to find the "b" coefficients is simpler than that to find the "a"s, but this expansion, (3.40), has two serious disadvantages [80]. Firstly, the theoretical expression for $d\sigma/d\Omega$ is naturally expressed in terms of the Legendre polynomials, so for strict comparison of experiment with theory, the conversion must be made to the form of 3.39. Secondly, the "b" coefficients are subject to strong statistical correlations, making correct analysis of experimental errors difficult. The "a" coefficients are only slightly correlated, and this is not a serious problem. Expansion in the form of equation 3.39 is thus prefered.

The coefficients are found by the method of least squares, the analysis being performed by the computer programme LPTSPL. Data input to the programme are the scattering angles in the centre of mass frame, the corresponding measurements of the differential cross-section, and the absolute errors in these measurements. The programme finds the best values of the "a" coefficients and the χ^2 values for the fits to the data. Also calculated is the 3 x 3 covariance matrix of which the diagonal elements are the variances of the respective "a" coefficients and the off-diagonal elements represent the correlations between the coefficients.

3.14.1. The Total Cross Section

The total cross-section, σ_τ, for a particular reaction is defined as the integral over the whole solid angle of the dif-ferential cross-section

$$\sigma_\tau = \int_o^{4\pi} (\frac{d\sigma}{d\Omega}) \, d\Omega \qquad \qquad ..(3.41)$$

Expressing $d\sigma/d\Omega$ in the above form, equation 3.39, and assuming that the differential cross-section is independent of the azimuthal angle,

$$\sigma_\tau = 2\pi \int_0^\pi (a_0 + a_2 \ P_2 \ (\cos \theta) + a_4 \ P_4 \ (\cos \theta)) \qquad ..(3.42)$$

thus; $\sigma_\tau = 4\pi \ a_0$ .. (3.43)

The total cross-section is thus found from the coefficient a_0, which is found by the computer fit to the experimental data.

4. THEORY OF THE INTERACTION

4.1. Introduction

The calculation of the differential cross-section for gamma-ray production in neutron inelastic scattering proceeds in two main stages. The first is to consider the interaction of the incident neutron with the nucleus concerned, resulting in the excitation of the nucleus above the ground state. The most successful method of describing the reaction is direct interaction theory. Previous work [17] at 14 MeV based on the theory of the compound nucleus has not satisfactorily predicted the experimental gamma-ray angular distributions, so in this work, only direct interaction theory is considered. This is expected to be more successful as it is widely used [7] to describe (n,x) reactions in this energy region. This first stage leads to the calculation of the density matrix elements describing the excitation of the nucleus after the reaction N(n,n')N*.

The second step is to consider the decay of the nucleus to the ground state, which takes place, in the cases considered, by electromagnetic transitions resulting in gamma-ray emission. Internal conversion is not a competing mode of de-excitation for the nuclei under consideration, and the energy levels are not high enough for particle emission to be possible. Thus this part of the calculation depends on only the spin states of the nucleus and the properties of the electromagnetic interaction. It is thus independent of considerations of nuclear models and interaction theory.

4.2. Interaction Mechanisms

The many-body problem of the interaction between the neutron and the nucleus could not be solved analytically, even if the exact analytical form of the nucleon-nucleon interaction were known. The fact that this interaction is not known exactly adds to the difficulties of dealing with the reaction on a microscopic level, that is, considering the interactions between the neutron and each nucleon in the presence of the other nucleons. These problems have lead to the use of various approximate methods of describing the interaction between the neutron and the nucleus, and of various models to represent the target nucleus. Some of the relevant theories will now be discussed.

4.2.1. Distorted Wave Born Approximation

In this approach, the incident neutron is represented by a wave distorted from the plane wave form by the nuclear potential The distorted waves, ϕ $(\underline{k},\underline{r})$ are given by the solution of Schrödinger's equation[7]

$$[\nabla^2 + k^2 - \frac{2\mu}{\hbar^2} V(\underline{r})] \ \phi \ (\underline{k},\underline{r}) = 0 \qquad ..(4.1)$$

where $\underline{k}$ is the neutron wave-vector, $\underline{r}$ the neutron displacement vector, $V(\underline{r})$ the potential due to nuclear forces, and μ the reduced mass of the system.

For charged particles, a Coulomb term $\frac{2\mu}{\hbar^2} \cdot \frac{Z_1 Z_2 e^2}{r}$ is also present in the Hamiltonian. The asymptotic form of the solutions of this equation in the incident and exit channels can be expressed as;

$$\phi^{1N}(\underline{k},\underline{r}) = \exp(i(\underline{k}.\underline{r})) + \frac{f(\theta,\phi)}{r}\exp(i(\underline{k}.\underline{r})) \qquad ..(4.2a)$$

$$\phi^{EX}(\underline{k},\underline{r}) = \exp(i(\underline{k}.\underline{r})) + \frac{f^{*}(\pi - \theta,\ \pi + \phi)}{r}\exp(i(\underline{k}.\underline{r})) \qquad ..(4.2b)$$

that is, as superpositions of plane and spherical waves. Using
first order perturbation theory [59], the matrix element for
transitions from a state i to a state f caused by a potential V
is given by:

$$M_{fi} = <J_B M_B, S_b M_b; \underline{k}_b|\underline{V}|J_A M_A, S_a M_a; \underline{k}_a> \qquad ..(4.3)$$

for a reaction of the form A(a,b)B. Then;

$$M_{fi} = \mathcal{J}\int d^3\underline{r}_{aA}\int d^3\underline{r}_{bB}\phi^{EX}_{bB}(\underline{k}_b,\underline{r}_{bB})<J_B M_B, S_b M_b|\underline{V}_{aABb}|J_A M_A, S_a M_a>$$

$$x\ \phi^{1N}_{aA}(\underline{k}_a,\underline{r}_{aA}) \qquad ..(4.4)$$

where J_I, S_i are the spins of the Ith nucleus or ith particle
respectively and M is the corresponding Z - component $\mathcal{J}$ is the
Jacobean of the transformation to the relative coordinates $\underline{r}_{aA}$
and $\underline{r}_{bB}$.

The use of perturbation theory is based on the assumption
that coupling between the various states of the nucleus is so
weak that there is no mutual interaction. However in many
cases the excited states of the nucleus have a collective
nature, and the coupling between states becomes appreciable,
so this approximation is no longer valid.

4.2.2. Strong Coupling Approximation

The strong coupling approximation (S.C.A.) is more appropriate, to the case of collective nuclear excitation. Instead of a perturbation treatment, the Schrödinger equation for the system is solved exactly for excitation of the first few nuclear levels.

The nuclear wavefunctions, $\phi_i(\xi)$ are the eigenfunctions of the nuclear Hamiltonian $H(\xi)$;

$$H(\xi)\phi_i(\xi) = \varepsilon_i\phi_i(\xi) \qquad ..(4.5)$$

where ξ represents all the relevant internal nuclear coordinates. The form of $H(\xi)$ is found by assuming a particular model for the nucleus, then equation 4.5 is solved to give the $\phi_i(\xi)$. The Schrödinger equation for the whole system, that is incident neutron and target nucleus is then:-

$$[T - V(\underline{r},\xi) + H(\xi)] \, \Psi(\underline{r},\xi) = E\Psi(\underline{r},\xi) \qquad ..(4.6)$$

where $T = - \hbar^2/2m \, \nabla r^2$ is the kinetic energy operator of the incident neutron, and $V(\underline{r},\xi)$ is the interaction potential between the nucleus and the neutron. The total scattering wavefunction $\Psi(\underline{r},\xi)$ is expanded in terms of the complete orthonormal set of $\phi_i(\xi)$

$$\Psi(\underline{r},\xi) = \sum_i \psi_i(\underline{r})\phi_i(\xi) \qquad ..(4.7)$$

Substituting for $\Psi(\underline{r},\xi)$ in equation 4.2 and taking matrix elements with respect to $\phi_j(\xi)$ results in the equation [60]:

$$[T + H(\xi) - E]\psi_i(\underline{r}) = \sum_i <\phi_j|V(\underline{r},\xi)|\phi_i\psi_i> - \sum_{i \neq j} <\phi_j|\phi_i(E - T - H(\xi))\psi_i>$$

$$..(4.8)$$

If all reactions other than scattering are explicitly excluded from the calculation, (in equation 4.5), then the second term on the right hand side of equation 4.8 is zero. In any case, it will be small due to the small overlap between ϕ_i and ϕ_j. This term is thus neglected and the following series of coupled equations obtained:-

$$[T + H(\xi) - E]\psi_i(\underline{r}) = \sum_i <\phi_j(\xi)|V(\underline{r},\xi)|\phi_i(\xi)\psi_i(\underline{r})> \quad ..(4.9)$$

The approximation in this case arises from the neglect of all nuclear levels above a certain limit. It is assumed that excitation of these levels is small compared with that of the levels explicitly included. In order to account for these higher levels, the interaction potential, $V(\underline{r},\xi)$, is made complex. The imaginary part of $V(\underline{r},\xi)$, thus leads to absorption of neutrons, that is, to reactions which are not explicitly included.

4.2.3. Choice of Interaction Mechanism

A measure of the strength of coupling between collective states of a non-spherical nucleus may be obtained by consideration of the nuclear deformation parameter β, defined by the expression:

$$R(\theta,\phi) = R_o[1 + \beta Y_2^o(\theta,\phi)] \qquad ..(4.10)$$

where $R(\theta,\phi)$ describes points on the nuclear surface, in the reference frame which has the symmetry axis of the nucleus as the z - axis and $Y_2^o(\theta,\phi)$ is a second order spherical harmonic. This

is a special case of equation 4.17, section 4.4.1. Investigation
(61, 62) of the matrix term in equation 4.4, shows that the in-
elastic cross-section for scattering from the first excited state
of the nucleus varies as β^2 in this approximation (D.W.B.A.).
The strong coupling approximation (S.C.A.), on the other hand,
predicts a more complicated dependence on β, giving closely simi-
lar results to those of DWBA only for $\beta \lesssim 0\cdot2$. For higher values
of β, the S.C.A. cross-section falls below that of DWBA for the
same nuclear potential, and varies approximately as β for $\beta \gtrsim 0\cdot3$.
(figure 4.1). Although it has been possible [63] to obtain agree-
ment between the two approaches by using different values of the
potential $V(\underline{r},\xi)$, it has been shown [62] that in general the two
approximations are not equivalent, and the S.C.A. is preferable
when $\beta \gtrsim 0\cdot2$. The nuclei considered here, namely Mg^{24}, Si^{28}, S^{32},
Ti^{48}, Cr^{52} and Fe^{56} have values of β ranging from $0\cdot21$ [12] for
Cr^{52} to $0\cdot62$ [11] for Mg^{24}, so the strong coupling approximation
is used.

4.3. Coupled Channels Equation

To solve the series of coupled equations 4.9 it is necessary
to expand $\Psi(\underline{r},\xi)$ in a suitable representation. Since the coupling
potential $V(\underline{r},\xi)$ is normally not scalar [64] in $\underline{r}$ or ξ separately
neither the nuclear spin I nor the orbital angular momentum ℓ are
good quantum numbers. Hence the ordinary partial wave expansion
for $\psi_i(\underline{r})$, that is,

$$\psi_a(\underline{r}) = \sum_{\ell m} \frac{U_a(r)}{r} Y_\ell^m (\theta,\phi) \qquad ..(4.11)$$

fails to give separation of variables. However, since $V(\underline{r},\xi)$ is
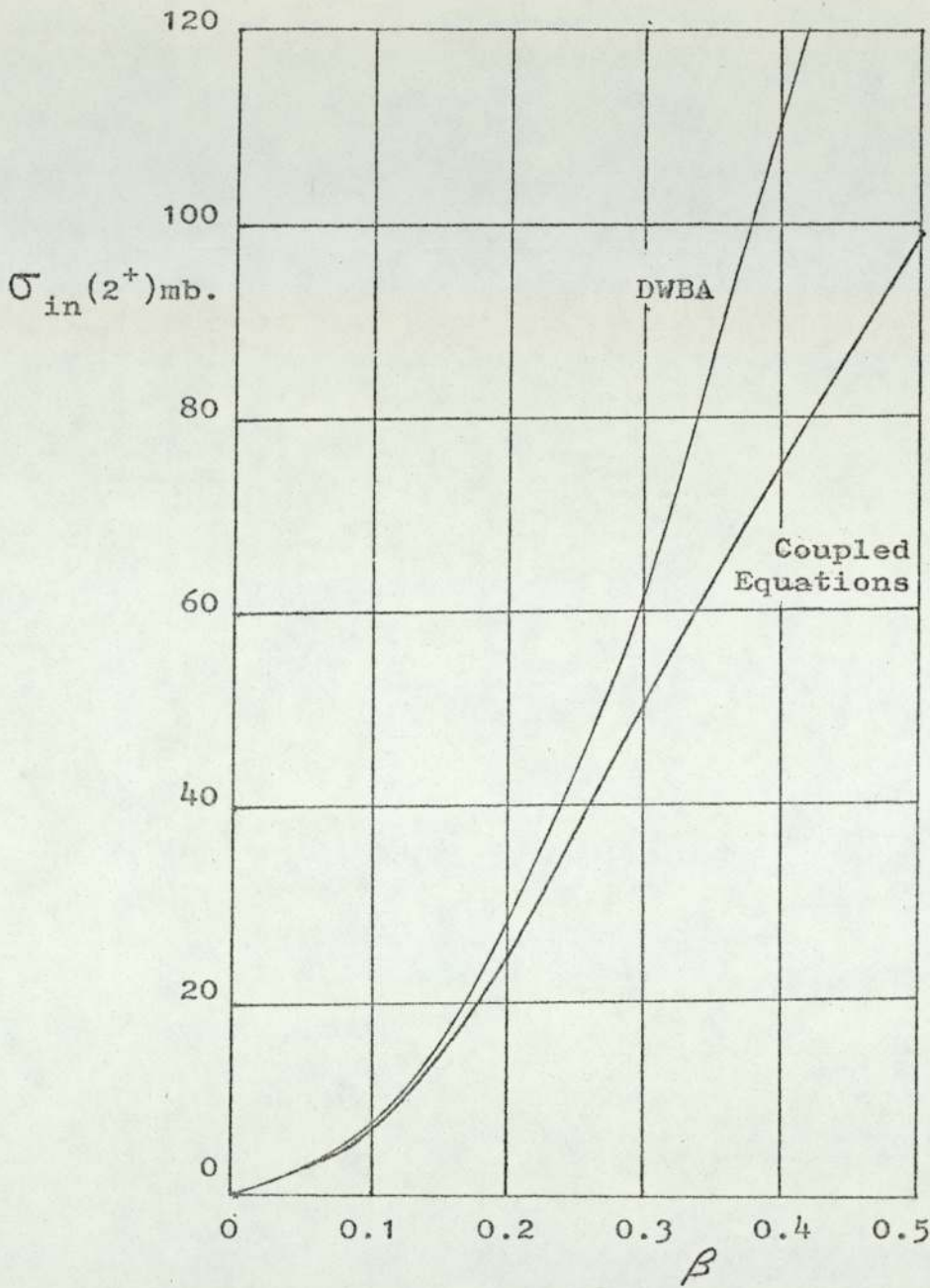
Figure 4.1 Comparison of DWBA and SCA predictions of the inelastic scattering cross-section for the reaction Ti^{48}(p,p') at 14.5 MeV.[61]

scalar in $\underline{r}$ and ξ jointly, $\underline{J}$, which is equal to $\underline{I} + \underline{\ell}$ and the parity are good quantum numbers. Then it is convenient[65] to expand in terms of eigenfunctions of the total momentum of the incident channel:

$$\Psi(\underline{r},\xi) = \sum_{JM} \Psi_{JM}(\underline{r},\xi) \qquad ..(4.12)$$

$$\Psi_{JM}(r,\xi) = \frac{1}{r} U^{J}_{z\ell}(r)\phi^{JM}_{z\ell}(\hat{\underline{r}},\xi) + \frac{1}{r} \sum_{z'\neq z,\ell'} U^{J}_{z'\ell'}(r)\phi^{JM}_{z'\ell'}(\hat{\underline{r}},\xi)$$

$$..(4.13)$$

where z labels the channel co-ordinates. When the target nucleus is in the ground state, the radial function $U^{J}_{z\ell}(r)$ contains both incoming and outgoing waves, but in an excited state, $U^{J}_{z'\ell'}(r)$ contains only outgoing waves. Using this representation in equation 4.9 and taking matrix elements with respect to $\phi^{JM}_{z\ell}$, the following equation is obtained:-

$$[\frac{d^2}{dr^2} + k^2_z - \frac{\ell(\ell + 1)}{r^2}]U^{J}_{z\ell}(r) = \frac{2\mu}{\hbar^2} \sum_{z\ell} V^{J}_{z\ell,z'\ell'}(r)U^{J}_{z'\ell'}(r)$$

$$..(4.14)$$

where the coupling potential is given by:-

$$V^{J}_{z\ell,z'\ell'}(r) = \langle\phi^{JM}_{z\ell}(\hat{\underline{r}},\xi)|V(\underline{r},\xi)|\phi^{JM}_{z'\ell'}(\hat{\underline{r}},\xi)\rangle \qquad ..(4.15)$$

Similarly, by taking matrix elements with respect to $\phi^{JM}_{z'\ell'}$:

$$[\frac{d^2}{dr^2} + k^2_{z'} - \frac{\ell'(\ell' + 1)}{r^2}]U^{J}_{z'\ell'}(r) = \frac{2\mu}{\hbar^2} \sum_{z''\ell''} V^{J}_{z''\ell'',z'\ell'}(r)U^{J}_{z''\ell''}(r)$$

$$..(4.16)$$

which describes multiple excitation of the state (z"ℓ"JM) through

the state $(z'\ell'JM)$. Besides providing a means of accurately calculating the excitation of the higher state $(z''\ell''JM)$, this process also affects the wavefunction in the $(z'\ell'JM)$ channel through the coupling to the higher state.

Thus the coupled channels formalism provides a set of coupled equations 4.14 for the wavefunctions in the elastic and inelastic channels of the reaction being considered. If the forms of the interaction potential $V(\underline{r},\xi)$ and the nuclear Hamiltonian $H(\xi)$ are known or assumed, these equations can be solved by numerical integration. Application of the appropriate boundary conditions enables the wavefunction in each channel to be calculated. Although the sum in equation 4.7 is, in priciple, finite, in practise the calculation becomes too time consuming if more than a small number of channels are considered. For this reason, the "Tamm-Dancoff" approximation is made, whereby only the first few terms of the sum are considered explicitly, the effect of the others being accounted for by the imaginary part of $V(\underline{r},\xi)$, which is now complex.

4.4. Nuclear Models

In order to solve the coupled equations of section 4.3, or indeed to use any of the other approximate methods of dealing with the neutron-nucleus interaction, a model of the nucleus must be used to obtain an analytic form for the nuclear Hamiltonian. One of these very simplified forms which is derived from one of the models, which is useful in this context, will now be described and details given of the two types of excitation spectra this model predicts.

- 104 -

All the nuclei under consideration have comparatively large permanent deformation parameters, β, in the range 0·21 to 0·62 measured by Coulomb excitation techniques [66], this implies that a suitable model for the description of low energy excitations of these nuclei may be that of rotations or vibrations of a liquid drop, since these states seem to have a strong collective nature.

4.4.1. Vibrational Excitations

Points on the nuclear surface [67] may be described by:-

$$R = R_o \left[1 + \sum_{\lambda=0}^{\infty} \sum_{\mu=-\lambda}^{\lambda} \alpha_{\lambda\mu} Y_{\lambda}^{\mu} (\theta,\phi)\right]... \quad ..(4.17)$$

Here Y_{λ}^{μ} are spherical harmonics and (θ,ϕ) are polar angles with respect to some arbitrarily chosen fixed space axes. Any collective motion of the nucleus is described by variation of the coefficients $\alpha_{\lambda\mu}$ with time. To first order in $\alpha_{\lambda\mu}$ the volume of the drop is [67]

$$V = V_o \left[1 + 3 \alpha_o / \sqrt{4\pi} \right] \quad ..(4.18)$$

Thus $\lambda = 0$ vibrations are associated with fluctuations in volume which are neglected as it is assumed that the liquid drop is in-compressible.

Considering a spherical drop which is first centred at the origin, so that $R = R_o$, then moved a distance $\alpha_1 R_o$ along the axis $\theta = 0$, the surface becomes [67]:-

$$R = R_o \left[1 + \alpha_1 \cos \theta + \sum_{\lambda=0}^{\infty} \alpha_{2\lambda} P_{2\lambda} (\cos \theta)\right] \quad ..(4.19)$$

where the $\alpha_{2\lambda}$ are all functions of α_1. Thus clearly $\lambda = 1$

vibrations correspond to a centre of mass motion, which in this
context is uninteresting.

The case $\lambda = 2$ represents quadrupole vibrations of a nucleus
which is spherically symmetric in the ground state. Assuming these
vibrations are quantized, the collective states have energies
given by:-

$$E_n = \sum_\lambda n_\lambda \, \hbar \, w_\lambda \qquad\qquad ..(4.20)$$

where n_λ is the number of phonons of order λ in the excited state.
The state with $n_\lambda = 1$ is $(2\lambda + 1)$ degenerate, and represents [68]
a $\lambda\mu$ phonon with angular momentum λ, z- component μ, and parity
$(-1)^\lambda$. The excitation spectrum predicted by this model is shown
in figure 4.2.

4.4.2 Rotational Excitations

Since $\lambda = 0$ and $\lambda = 1$ vibrations are not relevant, and $\lambda = 3$
and higher represent higher energy vibrations, only the case of
$\lambda = 2$ will now be considered. This is in accord with the use of
the Tamm-Dancoff approximation (section 4.3), which omits explicit
consideration of higher excited states.

Considering then nuclei which are permanantly deformed,
taking into account only $\lambda = 2$ deformations, then:

$$R = R_o \left[1 + \sum_{\mu=-2}^{2} \alpha_{2\mu} \, Y_2^\mu \, (\theta,\phi) \right] \qquad\qquad ..(4.21)$$

The angles (θ,ϕ) are measured relative to axes fixed in the
laboratory, so if the nucleus is rotating, the $\alpha_{2\mu}$ will be

$3\hbar w_2$ $0^+, 2^+, 4^+, 6^+$ $\dfrac{\hbar^2}{2I} 6(6+1)$ 6^+

$2\hbar w_2$ $0^+, 2^+, 4^+$

$\dfrac{\hbar^2}{2I} 4(4+1)$ 4^+

$\hbar w_2$ 2^+

$\dfrac{\hbar^2}{2I} 2(2+1)$ 2^+

0^+ 0^+

Figure 4.2   Figure 4.3

Spectrum of Vibrational   Spectrum of

Levels, from[67].   Rotational Levels.

from equation 4.29

Energy Ratio.	E_4/E_2	E_6/E_2	E_6/E_4
Theory	3.33	7.00	2.10
Mg^{24}	3.01	6.04	2.03
Si^{28}	2.60	4.74	1.825
Ti^{48}	2.33	3.39	1.454
Fe^{56}	2.46	4.00	1.645

TABLE 4.1 Comparison of Energy Ratios.

functions of time. However in the case of a nucleus of constant
shape, it is more appropriate to choose axes fixed in the nucleus
which reflect this invariance of shape, ie. the principal axes
of the nucleus. Referred to these axes, R is given by:-

$$R = R_o \left[1 + \sum_{\mu=-2}^{2} a_{2\mu} Y_2^{\mu} (\theta', \phi') \right] \qquad ..(4.22)$$

The relation [67] between the angles (θ, ϕ) and the angles (θ', ϕ')
is given by the rotation matrices $D_{\mu\mu'}^{\lambda} (\Theta, \Phi, \Psi)$, where Θ, Φ and Ψ
are the Euler angles of the body fixed axes relative to the space-
fixed axes, through the equation:-

$$Y_\lambda^\mu (\theta, \phi) = \sum_{\mu'} D_{\mu\mu'}^{\lambda} (\Theta, \Phi, \Psi) Y_\lambda^{\mu'} (\theta', \phi') \qquad ..(4.23)$$

thus;

$$a_{2\mu} = \sum_{\mu'} D_{\mu\mu'}^{2} \alpha_{2\mu} \qquad ..(4.24)$$

If the body fixed axes are the principal axes of the nucleus,
then the five coefficients $a_{2\mu}$ reduce to two independent variables
a_{22} and a_{20}. These, together with the three Euler angles, give a
complete description of the system. Rather than a_{22} and a_{20} two
new independent variables are introduced defined by:

$$a_{20} = \beta \cos \gamma \qquad ..(4.25a)$$

$$a_{22} = \tfrac{1}{2} \beta \sin \gamma \qquad ..(4.25b)$$

The constant density surface of the drop cuts its body
centred axes k (k = 1, 2, 3) at:

$$R_k = R_o \left[1 + \sqrt{\frac{5}{4\pi}}\ \beta \cos \left(\gamma - \frac{2\pi}{3} k\right)\right]\dots \qquad \dots(4.26)$$

If $k = 3$ labels the axis of symmetry, then the moment of inertia about this axis is zero. It is found that the moment of inertia about the other two axes is [67] :-

$$I = \frac{45}{16\pi}\ I_R\ \beta^2 \qquad \dots(4.27)$$

$$I_R = \frac{8\pi}{15}\ R_o^5\ \rho \qquad \dots(4.28)$$

I_R is the moment of inertia of a rigid sphere of radius R_o and constant density ρ. Since the measured values of β are much less than unity, it is concluded that only a small proportion of the nuclear "fluid" takes part in the effective rotation - in fact the rotation can be thought of as simply a "tidal wave" [69] moving across the surface of the drop.

Since there is an axis of symmetry, there are three constants of the motion: the total angular momentum J, its z - component M and its component along the symmetry axis, k. Assuming now that the rotations are quantized, so the energy levels are [67]:

$$E_J = \frac{\hbar}{2I}\ J\ (J + 1) \qquad \dots(4.29)$$

where J takes even values only [70], for symmetry considerations. This predicts a series of energy levels as shown in figure 4.3.

4.4.3. Choice of Nuclear Models

Whether a particular nucleus has a rotational or vibrational

spectrum is decided by inspection of the known energy levels. No nucleus shows a pure rotational or vibrational spectrum, because other factors alter the level positions, or introduce entirely different levels from those expected. Figure 4.4 shows possible rotational and vibrational bands, which have been extracted from the total spectra. The classification of these bands as vibrational or rotational is uncertain to some extent, as the spins of some of the various levels are not known accurately. These values are shown in brackets. For example the 6^+ level at 3·386 MeV [75] for Fe^{56} was not found by Armitage et al [76], but they report that this may be due to experimental difficulties in detecting levels of high spin. Shell model calculations by McGrory [77] predict such a level, and he quotes further experimental evidence for it.

Table 4.1 compares the ratios of excitation energies of these rotational levels, with those predicted by the model. Fair agreement is obtained, but as higher values of J are reached, the energies fall below the predicted values. This may be due to centrifugal stretching: as the nucleus rotates, centrifugal forces cause the nucleons to move further apart, increasing the size of the nucleus and hence its moment of inertia I, and correspondingly reducing E_J. This effect is observed in many rotational spectra, and was first considered by Bohr [68].

4.5. The Optical Potential

The expression for the interaction potential $V(\underline{r}, \xi)$ is that of the optical model potential, which has the general form [7]:-

$$V_{om}(r, \xi) = V_c(r) - V_o f_o(r) - iW_v f_v(r) - iW_s g_s(r) - V_{so} h(r) \underline{L} . \underline{S}$$

$$..(4.30)$$

8.12_____(6$^+$)   8.54_____6$^+$ 3.33_____6$^+$

4.12_____4$^+$ 4.62_____4$^+$ 2.29_____4$^+$

1.37_____2$^+$ 1.78_____2$^+$ 0.98_____2$^+$

_____0$^+$ _____0$^+$ _____0$^+$
Mg^{24}.ref$^{(73)}$ Si^{28}ref$^{(73)}$.   Ti^{48}ref$^{(74)}$

3.38_____(6$^+$)

2.08_____4$^+$

0.85_____2$^+$

_____0$^+$
Fe^{56}ref$^{(72)}$

2.7680_____2$^+$ 4.4588_____4$^+$
2.647 _____0$^+$ 4.2816_____2$^+$
2.3698_____4$^+$ 3.7787_____0$^+$

1.43419_____2$^+$ 2.2302_____2$^+$

_____0$^+$ _____0$^+$
Cr^{52}.ref$^{(71)}$ S^{32}.ref$^{(73)}$
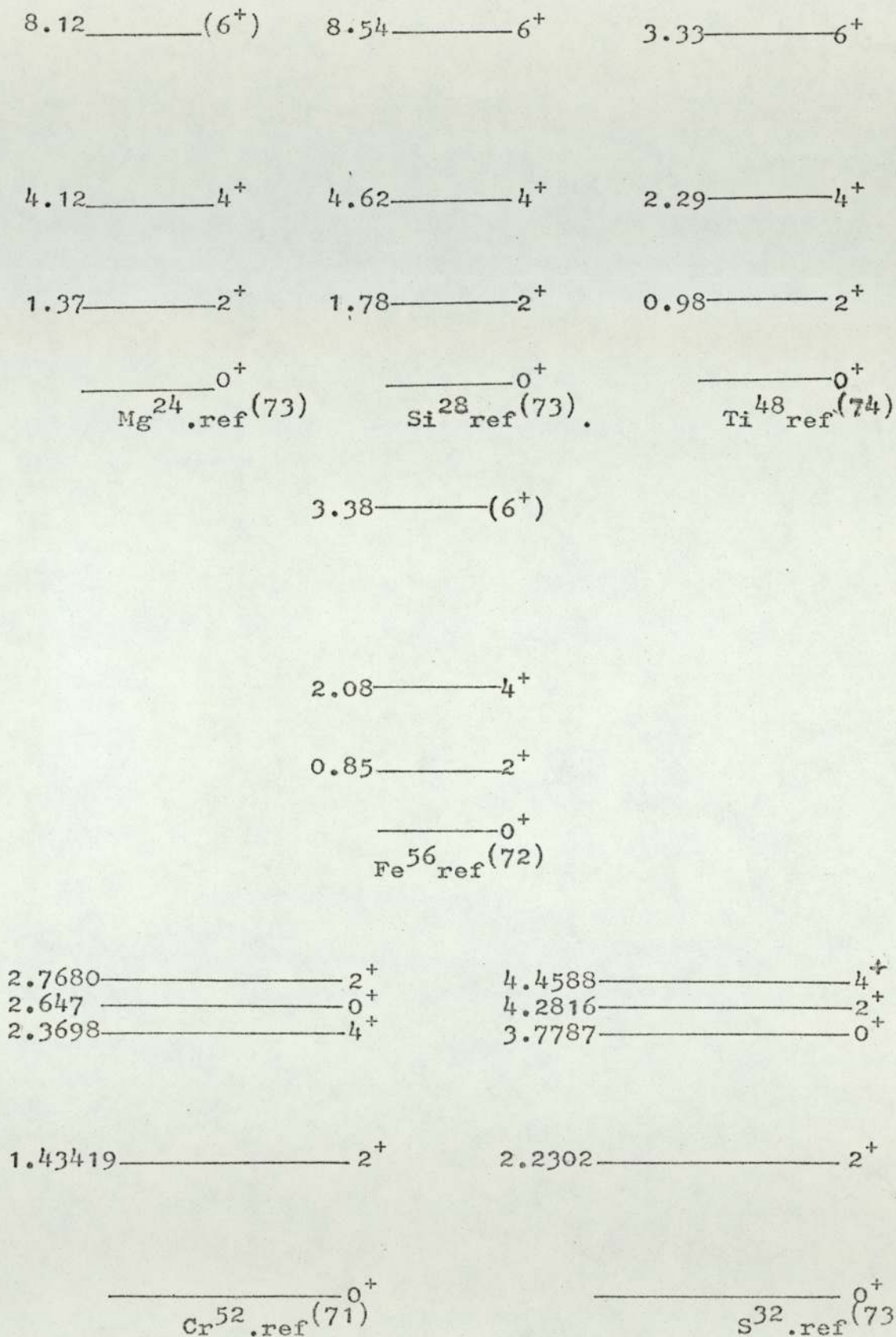
Figure 4.4   Possible Rotational and Vibrational Bands.

$V_c(r)$ is a Coulomb term, which is zero for neutron interactions. V_o is the depth of the real part of the attractive nuclear potential, while W_v and W_s represent the volume and surface absorptive parts of the potential. V_{so} is the depth of the spin-orbit term. The form factor $f(r)$ is taken to have the Saxon-Woods form:

$$f_o(r) = [1 + \exp{(r - r_o A^{1/3})} /a_o]^{-1} \qquad ..(4.31)$$

and,
$$g_s(r) = 4\,a_s \frac{d}{dr} f_s(r)\dots \qquad ..(4.32)$$

The factor $-4\,a_s$ normalizes the form factor $g(r)$ to a maximum value of unity. The form of the spin-orbit potential is also related to the Saxon-Woods derivative:

$$h(r) = -\left(\frac{h}{m_\pi c}\right)^2 \frac{1}{r}\frac{d}{dr} f(r)\dots \qquad ..(4.33)$$

These forms for the various terms of the potential are widely used as they have been found to provide good agreement with experimental results, and are also fairly convenient to deal with theoretically. The values of the parameters V_o, W_v, W_s, V_{so}, r_o, a_o etc., which are dependent on A and E (target nucleus mass number, and incident neutron energy) have been found by fitting the predicted eleastic cross-section to the experimental values [78]. The systematic adjustment of the parameters necessary to optimize the fit to the data, has been done by computer. When values for these parameters have been found the differential cross-section for inelastic scattering to the first excited state is then fitted, using in addition the nuclear deformation β. Generally the cross-section cannot be

fitted by variation of β only, so the other parameters are again
varied systematically to obtain the best fit to both elastic and
inelastic scattering data.

4.6. Density Matrix [79]

If all the identical, non-interacting components of an
assembly are described by the same wavefunction ψ, then the whole
assembly is described by $\sum_n a_n \psi_n$, where;

$$\sum_n | a_n |^2 = 1 \qquad\qquad ..(4.34)$$

The assembly is then said to be in a "pure" state. The density
matrix $\underline{\rho}$ for such an assembly is defined by;

$$\rho_{nm} = a_n a_m^* \qquad\qquad ..(4.35)$$

and $$\qquad tr(\underline{\rho}) = 1 \qquad\qquad ..(4.36)$$

Generally such complete information will not be available, and
the assembly will be in a "mixed" state. However this can be
described as a weighted mixture of the pure states, and the
density matrix elements are then;

$$\rho_{nm} = \overline{a_n a_m^*} \qquad\qquad ..(4.37)$$

The expectation value of any operator $\underline{O}$ in the assembly is
given by:

$$<\underline{O}> = \sum_{nm} \rho_{nm} O_{mn} = tr (\underline{\rho}\ \underline{O}) \qquad\qquad ..(4.38)$$

The density matrix after the scattering event is thus defined by;

$$\rho_{JJ'} = \Psi_{JM} (\underline{r}, \xi) \Psi^*_{J'M'} (\underline{r}, \xi) \qquad ..(4.39)$$

4.7. Gamma-ray Angular Distribution

For the second major part of the calculation of the gamma-ray angular distributions it is convenient to use the notation of Ferguson [80], based on that of Dirac [81]. The density matrix element between the states with angular momentum $\underline{a}$ and $\underline{a}'$, and z - component α and α' is written

$$<a\alpha \mid \rho \mid a'\alpha'>$$

which is equivalent to equation 4.39 with $J = a$ and $M = \alpha$.

The density matrix is then used to define the statistical tensor $\rho_{kk} (a, a')$ which contains, in a useful form, the angular momentum information of the system,

$$\rho_{kk}(a, a') = \sum_{\alpha\alpha'} (-1)^{a'-\alpha'} (a\alpha, a' - \alpha' | kk) <a\alpha|\rho|a'\alpha'> \qquad ..(4.40)$$

here $(a\alpha, a' - \alpha' | kk)$ is a Clebsch - Gordan coefficient describing the vector sum;

$$\underline{k} = \underline{a} - \underline{a}' \qquad ..(4.41)$$

which defines $\underline{k}$, with z - component κ.

The efficiency of the gamma-ray detector is then expressed, in the same angular momentum representation, as a tensor $\epsilon_{kk}(L, L')$

where L is the multipolarity of the gamma-radiation being detected.
The advantage of this notation is that the use of equation 4.38
leads immediately to an expression for the angular correlation
function W, of the form,

$$W = tr\ (\rho\varepsilon) \qquad\qquad ..(4.42)$$

if ρ is the statistical tensor and ε the efficiency tensor. The
correlation function W, which represents the probability of
detecting both the inelastically scattered neutron at a given
angle, and also the gamma-ray emitted by the target nucleus at
another given scattering angle. Averaging over all possible
neutron scattering angles leads to the gamma-ray angular dis-
tribution.

The efficiency tensor may be expressed in terms of the co-
ordinates of the detector, and includes effects due to the finite
size of the crystal. For the particular case of this experiment,
the detector is a cylindrical NaI crystal, with axial symmetry,
for which the efficiency tensor is [80];

$$\varepsilon_{k\kappa}(LL') = \frac{\hat{L}\hat{L}'}{\sqrt{4\pi}}\ (-1)^{L'-1}\ (L1,L'-1|k0)Q_k\ \frac{2\pi Jo}{\hat{k}}\ Y_k^{\kappa*}(\theta,\phi) \quad ..(4.43)$$

where;

$$\hat{x} = (2x + 1)^{\frac{1}{2}} \qquad\qquad ..(4.44)$$

and Q_k is an attenuation factor which corrects for the finite
size of the crystal and $2\pi Jo$ is the total efficiency of the
detector.

The reaction considered is then a nuclear state of spin $\underline{a}$ decaying to a state of spin $\underline{b}$ by emitting a gamma-ray of multipolarity L;

$$\underline{a} = \underline{b} + \underline{L} \qquad ..(4.45)$$

then the correlation function is;

$$W = \sum_{bb'LL'k_b\kappa_b k_L\kappa_L} \rho_{k_b\kappa_b}(bb')\rho_{k_L\kappa_L}(LL')\epsilon^*_{k_b\kappa_b}(bb')\epsilon^*_{k_L\kappa_L}(LL') \quad ..(4.46)$$

by analogy with equation 4.38. The tensors for the final state can be related to those of the initial state by the relation;

$$\rho_{k_b\kappa_b}(bb')\rho_{k_L\kappa_L}(LL') = \sum_{aa'k\kappa} \rho_{k\kappa}(aa')(k_b\kappa_b k_L\kappa_L|k\kappa)\hat{a}\hat{a}'\hat{k}_b\hat{k}_L x$$

$$x \left\{ \begin{array}{ccc} b & L & a \\ b' & L' & a' \\ k_b & k_L & k \end{array} \right\} <b|L||a><b'|L'||a'>* \qquad ..(4.47)$$

Substitution of equation 4.47 in equation 4.46 gives the result;

$$W = \sum \rho_{k\kappa}(aa')\epsilon^*_{k_b\kappa_b}(bb')\epsilon^*_{k_L\kappa_L}(LL')(k_b\kappa_b k_L\kappa_L|k\kappa)\hat{a}\hat{a}'\hat{k}_b\hat{k}_L x$$

$$x \left\{ \begin{array}{ccc} b & L & a \\ b' & L' & a' \\ k_b & k_L & k \end{array} \right\} <b|L||a><b'|L'||a'>* \qquad ..(4.48)$$

where the sum is over $aa'bb'LL'k\kappa k_b\kappa_b k_L\kappa_L$. This expression gives

the gamma-ray angular distribution. Since the recoil nucleus can-
not be detected, the efficiency tensor is simply;

$$\varepsilon_{k_b \kappa_b}(bb') = \hat{b}\delta_{k_b 0}\delta_{\kappa_b 0}\delta_{bb'} \qquad \qquad ..(4.49)$$

This factor must be included, because the efficiency matrix must
be expressed in the same representation as the density matrix,
and this includes the nuclear co-ordinates.

4.8. Scattering from the First Excited State

Considerable simplification of equation 4.48 can be achieved
if scattering from only the first excited state of the nucleus is
included. All the nuclei treated here are even - even, with 0^+
ground state and 2^+ first excited state. The justification for
this simplification will be considered later, in section 5.5.

In the above notation, then, a = 2, b = 0 and L = 2. Then
substitution in equation 4.48 gives;

$$W = \sum_{k\kappa k_L \kappa_L} \rho_{k\kappa}\varepsilon^*_{k_L \kappa_L}(00,k_L\kappa_L|k\kappa)5\hat{k}_L \left\{ \begin{array}{ccc} 0 & 2 & 2 \\ 0 & 2 & 2 \\ 0 & k_L & k \end{array} \right\} \qquad ..(4.50)$$

because

$$\varepsilon^*_{k_b \kappa_b} = \hat{b}\,\delta_{k_b 0}\delta_{\kappa_b 0}\delta_{bb'} = 1 \qquad \qquad ..(4.51)$$

This implies $k_b = \kappa_b = 0$. The reduced matrix elements are both
unity. Then the Clebsch - Gordan coefficient $(00,k_L\kappa_L|k\kappa)$ is
unity when $k_L = k$ and $\kappa_L = \kappa$ and zero otherwise. Hence;

$$W = 5\sum_{k\kappa} \rho_{k\kappa}\,\varepsilon^*_{k\kappa}\,\hat{k} \left\{ \begin{array}{ccc} 0 & 2 & 2 \\ 0 & 2 & 2 \\ 0 & k & k \end{array} \right\} \qquad ..(4.52)$$

Considering the 9 - j coefficient, interchanging the first and third columns gives,

$$\begin{Bmatrix} 2 & 2 & 0 \\ 2 & 2 & 0 \\ k & k & 0 \end{Bmatrix}$$

which can be expressed [(80)];

$$\frac{\delta_{oo}\delta_{kk}(-1)^{k}}{\hat{k}} \; W(2222:0k)$$

where W is a Racah coefficient. The symmetry properties of Racah coefficients means that;

$$W(2222:0k) = W(2222:k0)$$

and this has the value,

$$\frac{\delta_{22}\delta_{22}}{\hat{2}\hat{2}}(-1)^{-k}$$

Since k takes even values only,

$$W(2222:0k) = 1/5$$

Thus the 9 - j coefficient has the value $1/5\hat{k}$, so the angular distribution further simplifies to;

$$W = \sum_{k\kappa} \rho_{k\kappa} \; \varepsilon_{k\kappa}^{*} \qquad ..(4.53)$$

The angular dependence of W is contained in the factor $\varepsilon_{k\kappa}$;

$$\varepsilon_{k\kappa} = -\frac{5}{\sqrt{4\pi}} \frac{Q_{k}}{\hat{k}} (2\pi Jo)(21,2-1|k0) \; Y_{k}^{\kappa *}(\theta,\phi) \qquad ..(4.54)$$

from equation 4.43. Thus;

$$W = - \frac{5}{\sqrt{4\pi}} (2\pi J_0) \sum_{k\kappa} \frac{Q_k}{\hat{k}} (21,2-1|k0) \rho_{k\kappa} Y_k^\kappa (\theta,\phi) \quad ..(4.55)$$

The spherical harmonics $Y_k^\kappa (\theta,\phi)$ can be expressed in the form [82];

$$Y_k^\kappa (\theta,\phi) = (-1)^\kappa (\frac{2k+1}{4\pi} \frac{(k-|\kappa|)!}{(k+|\kappa|)!})^{\frac{1}{2}} P_k^\kappa (\cos \theta) e^{i\kappa\phi} \quad ..(4.56)$$

for $\kappa \geq 0$, where $P_k^\kappa (\cos \theta)$ is an associated Legendre function.
The azymuthal angle, ϕ, of the gamma-ray emission is not detected,
so W is averaged over ϕ;

$$\frac{1}{2\pi} \int_0^{2\pi} e^{i\kappa\phi} d\phi = 0 \qquad (\text{when } \kappa \neq 0) \qquad ..(4.57a)$$

$$= 1 \qquad (\text{when } \kappa = 0) \qquad ..(4.57b)$$

The associated Legendre functions $P_k^\kappa (\cos \theta)$ are related to the
Legendre polynomials by the expression [82],

$$P_k^\kappa (x) = (1-x^2)^{|\kappa|/2} \frac{d^{|\kappa|}}{dx^{|\kappa|}} P_k (x) \qquad ..(4.58)$$

Thus since $\kappa = 0$ from equation 4.57, the Legendre polynomials
may be used;

$$W = - \frac{5}{4\pi} (2\pi J_0) \sum_k Q_k (21,2-1|k0) \rho_{k0} P_k (\cos \theta) \qquad ..(4.59)$$

The values of Q_k have been tabulated [83], but for the
experimental situation relevant here, they are effectively
unity. For $k = 0$, this is exactly true, while for $k = 2$ and
4 the error is of the order of 0·5% and 1% respectively. The

fact that k has even values only, follows from the symmetry
properties of the system. Litherland and Ferguson [84] have
shown that if the final state, formed as a result of a nuclear
reaction in which a particle is incident along the z - axis, has
a definite parity, and if the incident beam and the target are
unpolarized, then only tensor parameters having even values of
k are non-zero. This follows from the symmetry of the system for
reflection in the origin.

4.9. I.N.C.H. - A Coupled-Channels Programme

The coupled-channels calculation, based on the strong coupling
approximation and equation 4.9, are performed by the programme INCH,
written by A. D. Hill of Oxford. This solves the coupled equations
by numerical integration, and hence finds the wavefunctions in the
exit channels. In the original version of INCH, these were then
used to compute differential inelastic scattering cross-sections
and polarizations.

An additional subroutine GAMMA has been written to calculate
the gamma-ray differential cross-section using equation 4.59. As
stated in a previous section, only coupling between the ground
state, 0^+, and the first excited state, 2^+, of the nucleus is con-
sidered, to simplify the treatment of the angula momenta. The
listing of GAMMA is given in appendix 1.

The complex wavefunctions in the various exit channels are
held in INCH in the arrays AMPRE (real parts) and AMPIM (imaginary
parts). The original version of INCH performed this calculation
only for $S_i = +\frac{1}{2}$ (where S is the z - component of the incident
neutron spin). However the direction of S affects the spin of

the residual nucleus after neutron scattering, so both directions of S must be considered for the gamma-ray distribution. This change was made by a few simple alterations [85] in other sub-routines.

The complex density matrix DENSRE and DENSIM is calculated from the wavefunctions in AMP by use of equation 4.37. The elements are averaged over $S_i = \pm \frac{1}{2}$ and summed over $S_f = \pm \frac{1}{2}$, since the incident neutron beam is unpolarized and the scattered neutron spin is not detected. The matrix elements are also aver-aged over THETA, the neutron scattering angle. (The range of THETA is set in the data input, in this case $10°$ to $180°$ in $2°$ steps).

The statistical tensor, TRE and TIM (real and imaginary parts), is then calculated from equation 4.40. The index of T(K) labels the values of k and κ in the following sequence $k = 0$, $\kappa = 0$; $k = 2$, $\kappa = 2$; $1....-2$; $k = 4$, $\kappa = 4....-4$. Finally equation 4.59 is used to calculate the gamma-ray angular distribution. It is convenient to express this in the form:-

$$W = a_o P_o (\cos \theta) + a_2 P_2 (\cos \theta) + a_4 P_4 (\cos \theta) \quad ..(4.60)$$

and the values of a_o, a_2 and a_4 are printed out by GAMMA.

4.10. Checks On The Use Of The AMP Arrays

To ensure that the AMP arrays have been correctly understood and derived from the rest of the programme, checks were made in GAMMA. The trace of the density matrix, and the neutron asymmetry given by:-

$$\varepsilon = \frac{dr/d\Omega(\uparrow) - dr/d\Omega(\downarrow)}{dr/d\Omega(\uparrow) + dr/d\Omega(\downarrow)} \qquad ..(4.61)$$

(where the arrows define the final neutron spin direction relative to the neutron scattering direction), have been compared with the differential cross-section and asymmetry for neutron elastic scattering as calculated in the original version of INCH. This has shown that the calculations in GAMMA are reliable - the only difference is a factor of 10 between the trace in GAMMA and the differential cross-section, which arises because the trace is in units of $fermi^2$ (10^{-30} m^2) and the cross-section is in mbarns/str (10^{-31} m^2). These routines have now been removed for economy in computing time.

4.11. Input to INCH

The programme INCH requires as data input, the matrix elements of the nuclear potential between the various states, that is the elements, $\langle \phi_j | V(r, \xi) | \phi_i \rangle$, with the notation of section 4.2.2. Since coupling between the ground state and the first excited state only is being investigated, the matrix elements are:-

$$\langle 0^+ | V | 0^+ \rangle, \qquad \langle 0^+ | V | 2^+ \rangle, \qquad \langle 2^+ | V | 2^+ \rangle$$

These have been calculated [61] for the particular cases considered here, namely rotational and vibrational models of the nucleus and a Saxon - Woods form of the terms of the potential $V(r, \xi)$.

In both cases, the term $\langle 0^+ | V | 0^+ \rangle$ is simply the original optical model potential, as described in section 4.5, that is;

$$V_{oo} = - V_o f_o(r) - i W_v f_v(r) - i W_s g_s(r) - V_{so} h(r) \underline{L}.\underline{S} \qquad ..(4.62)$$

The potential is attractive, so V_o, W_v, W_s and V_{so} are positive numbers measuring the depths of the various terms of the potential The second term, $<0^+|V|2^+>$, has been found [61] to be given by;

$$\frac{\beta}{\sqrt{4\pi}} (V_o f'_o(r) + W_v f'_v(r) + W_s g'_s(r) + V_{so} h'(r) \underline{L}.\underline{S})$$

The third term $<2^+|V|2^+>$ is;

$$- \sqrt{\frac{5}{14\pi}} \beta (V_o f'_o(r) + W_v f'_v(r) + W_s g'_s(r) + V_{so} h'(r) \underline{L}.\underline{S})$$

$$- (V_o f_o(r) + W_v f_v(r) + W_s g_s(r) + V_{so} h(r) \underline{L}.\underline{S})$$

for the rotational model, while the first bracket is missing for the vibrational model. This factorization of the terms of the potential is used in the input to INCH, where the various terms are listed as the product of a positive well - depth, in MeV, and a form factor of a standard type. For prolate deformation of the nucleus, β is positive, while for oblate deformations, β is negative. The signs of the various matrix elements thus depend on the nature of the nuclear deformation.

The derivative forms are taken to have the same parameter values of r and a, as the original form factors. Thus the list of parameters required is;

$$V_o, r_o, a_o; W_v, r_v, a_v; W_s, r_s, a_s; V_{so}, r_{so}, a_{so}; \beta.$$

As described in section 4.5, these parameters are found by fitting the experimental data of several worker [11, 86, 87] on the elastic and inelastic differential cross-sections for neutron scattering.

They depend on A (atomic weight of the scattering nucleus), and
E (energy of the incident neutron). Terms describing isotopic
spin dependence, varying as $(N - Z)/A$ are sometimes also included.
Bechetti and Greenlees [86] have found a group of "global" para-
meters, which fit nucleon scattering over a range of nuclei and
incident energy. These parameters have been used for the three
heavier nuclei under consideration; Ti^{48}, Cr^{52} and Fe^{56}, since
they are expected to be reliable for A>40, and E<50 MeV. These
parameters are given by the relations [86];

$$V_o = 56 \cdot 3 - 0 \cdot 32E - 24\xi$$

$$W_v = 0 \cdot 22E - 1 \cdot 6$$

or zero, whichever is greater.

$$W_s = 13 - 0 \cdot 25E - 12\xi$$

$$V_{so} = 6 \cdot 2$$

$$r_o = 1 \cdot 17$$

$$a_o = 0 \cdot 75$$

$$r_{v,s} = 1 \cdot 26$$

$$a_{v,s} = 0 \cdot 58$$

$$r_{so} = 1 \cdot 01$$

$$a_{so} = 0 \cdot 75$$

$$\xi = (N - Z)/A$$

The energy E is measured in MeV, potential depths are in MeV, and
distances in fermis (10^{-15} m).

For the lighter nuclei; Mg^{24}, Si^{28}, S^{32}, fluctuations in
the parameters as functions of A and E are too marked to permit
the use of a "global" set to fit all nuclei. For this reason
parameters are used which have been obtained by fitting the
scattering data of each element separately. Work on these

elements has been published by Stelson et al [12] and Clarke and Cross [11]. Using D.W.B.A., Clarke and Cross report that almost as good agreement with experiment is obtained using only a surface absorption term, or only a volume absorption term, as both together. However, they expect that if the S.C.A. were used, the resulting potential parameters would be significantly different from their values. Stelson reports the results of fitting the Mg^{24} data (elastic and inelastic neutron differential cross-sections) with both D.W.B.A. and S.C.A. The resulting potential parameters are quite similar:-

D.W.B.A. $\qquad V_o = 44 \cdot 9$ MeV, $\qquad W_s = 9 \cdot 8$ MeV, $\qquad V_{so} = 7 \cdot 0$ MeV

S.C.A. $\qquad V_o = 43.3$ MeV, $\qquad W_s = 6 \cdot 3$ MeV, $\qquad V_{so} = 7 \cdot 0$ MeV

These are the values which give the "best" fits, but it is not reported how strongly the goodness of fit depends on the parameter values, so it is not known how much the fit would be affected if, for example, the D.W.B.A. set of parameters were used in the S.C.A. The above values for the S.C.A. theory were thus used for Mg^{24}. For Si^{28} and S^{32}, no report is given of S.C.A. fits to the data. Thus the same parameters were used as for Mg^{24}.. The justification for this lies in the fact that the D.W.B.A. parameters specifically fitted to the Mg^{24} data differ very little from those obtained from a best fit to the data for several elements. It is thus expected that the S.C.A. parameters will vary little over this range. The values obtained in this way are significantly different from those predicted by the expressions of Bechetti and Greenlees [86], for example;

ref (86)	r fm	a fm	ref (11)	r fm	a fm
V_o = 51·89	1·17	0·75	43·3	1·25	0·65
W_V = 1·48	1·26	0·58	0·0	-	-
W_s = 9·5	1·26	0·58	6·3	1·25	0·47
V_{so} = 6·2	1·01	0·75	7·0	1·25	0·65

The parameters which were used are listed in table 4.2.

	V_o	r_o	a_o	W_v	r_v	a_v	W_s	r_s	a_s	V_{so}	r_{so}	a_{so}	β
Mg^{24}	43·3	1·25	0·65				6·3	1·25	0·47	7·0	1·25	0·65	0·62
Si^{28}	43·3	1·25	0·65				6·3	1·25	0·47	7·0	1·25	0·65	0·41
S^{32}	43·3	1·25	0·65				6·3	1·25	0·47	7·0	1·25	0·65	0·36
Ti^{48}	49·75	1·17	0·75	1·524	1·26	0·58	8·45	1·26	0·58	6·2	1·01	0·75	0·26
Cr^{52}	49·91	1·17	0·75	1·524	1·26	0·58	8·53	1·26	0·58	6·2	1·01	0·75	0·21
Fe^{56}	50·04	1·17	0·75	1·524	1·26	0·58	8·59	1·26	0·58	6·2	1·01	0·75	0·24

TABLE 4.2

Potentials in MeV, Lengths in Fermi

The values of β listed in table II have been found from various sources. Stelson [12] and Clarke and Cross [11] agree on the value of β for Mg^{24}, so this value is used. For Si^{28} and S^{32}, there are slight differences, which appear to be within the range of experimental error. A value between these two is thus taken in each case. For Cr^{52}, the only value based on neutron data is that of Stelson, so this is used. No values for β based on neutron data have been published for Ti^{48} and Fe^{56}, so the values found by Buck [61] for 14 MeV proton data are used. Comparison of the

proton work [61] with the neutron results [12] shows that the values of β found for several isotopes are comparable, within the quoted errors.

5. EXPERIMENTAL AND THEORETICAL RESULTS

5.1. Magnesium

5.1.1. Interpretation of Energy Spectrum

A typical energy spectrum of the gamma-rays produced by neutron bombardment of magnesium is shown in figure 5.1. Background has been subtracted from this and all following spectra. The error bars show statistical uncertainties only. The spectra are recorded in the energy range $0 \cdot 95$ MeV to $3 \cdot 2$ MeV for magnesium. There is an energy interval of 41 KeV/channel. Peaks are resolved at $1 \cdot 37$ MeV and $1 \cdot 82$ MeV and there is evidence of peaks of higher energy, in the approximate range $2 \cdot 6$ MeV to $3 \cdot 2$ MeV.

Figure $5 \cdot 2$ shows the level scheme of Mg^{24}, as reported by Endt and Van der Leun [73]. This enables the peak at $1 \cdot 37$ MeV to be identified as that due to the transition from the first excited state, (2^+), to the ground state. This transition gives rise to a gamma-ray of energy $1 \cdot 36859$ MeV. Mg^{24} has an isotopic abundance of $78 \cdot 6\%$ [88].

The $1 \cdot 82$ MeV peak cannot be easily identified from the Mg^{24} level scheme; a possible transition is that from the $6 \cdot 01$ MeV, (4^+), level to the 2^+ level at $4 \cdot 24$ MeV, which gives rise to a $1 \cdot 77$ MeV gamma-ray. However, this transition forms only 7% of the gamma-ray transitions from the level, and in view of the energy discrepancy, is unlikely to explain the presence of this line. This gamma-ray peak is most probably due to the presence of the isotope Mg^{26}, which has an abundance of $11 \cdot 29\%$, in natural magnesium. Transitions in this nucleus from the first excited state, (2^+), to the ground
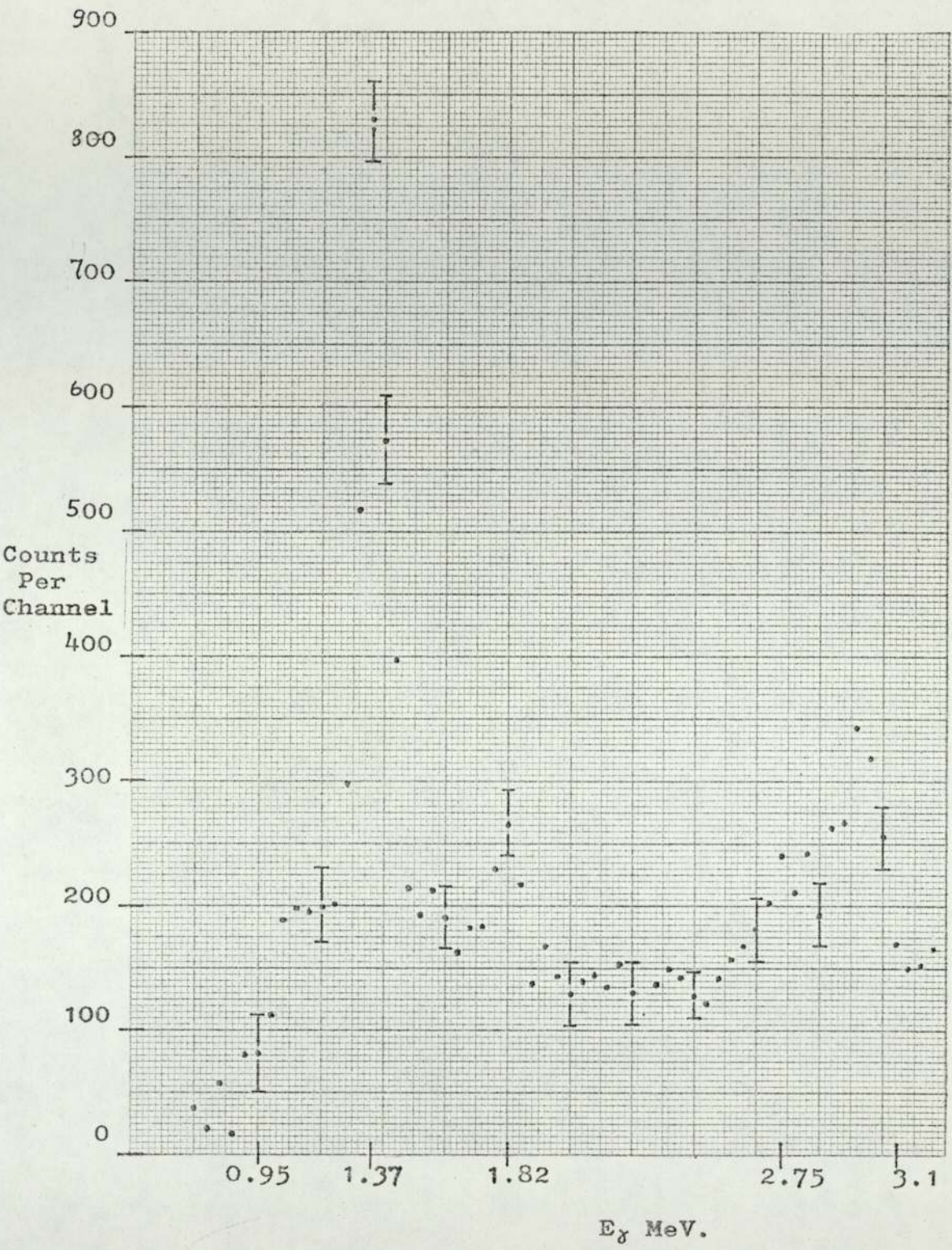
Figure 5. 1   Spectrum of Gamma-Ray Energies from
Magnesium.

6.4318 _____ 17% 83% 0⁺

6.0103 _____ 7% 93% 4⁺

5.2360 _____ 1.7% 98.3% 3⁺
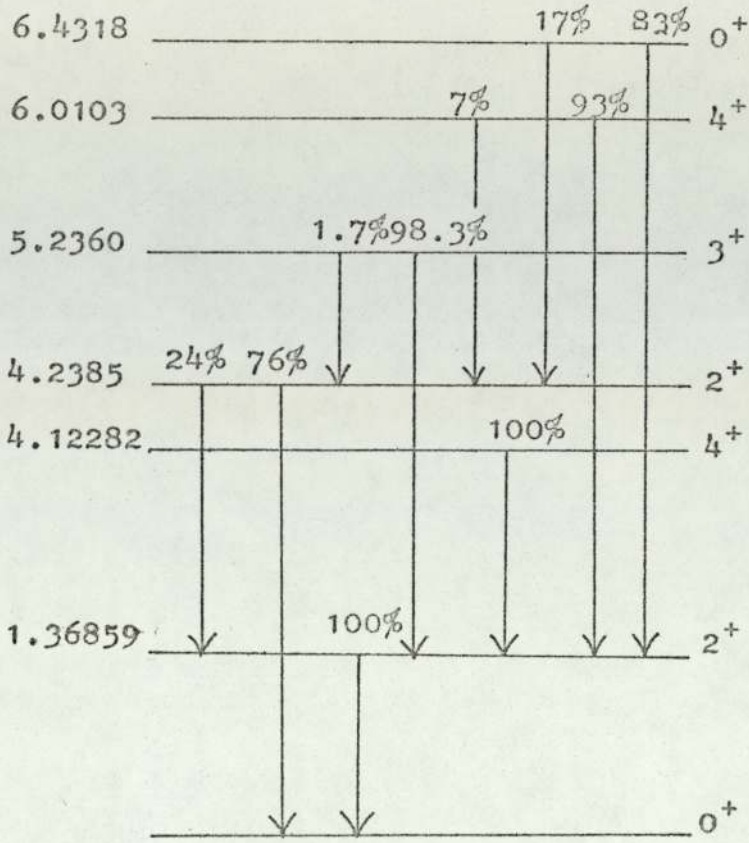
Figure 5.2
Level Scheme and
Branching Ratios(73)
of Mg²⁴.

4.2385 _____ 24% 76% 2⁺
4.12282 _____ 100% 4⁺

1.36859 _____ 100% 2⁺

0⁺

Mg²⁴

2.8656 _____ 39% 61% 9/2⁺
2.7961 _____ 100% 1/2⁺
2.7885 _____ 15% 85% 1/2⁻

Figure 5.3
Level Scheme and
Branching Ratios(73)
of Na²¹.

1.7456 _____ 6% 94% 7/2⁺

0.3505 _____ 100% 5/2⁺

3/2⁺

Na²¹
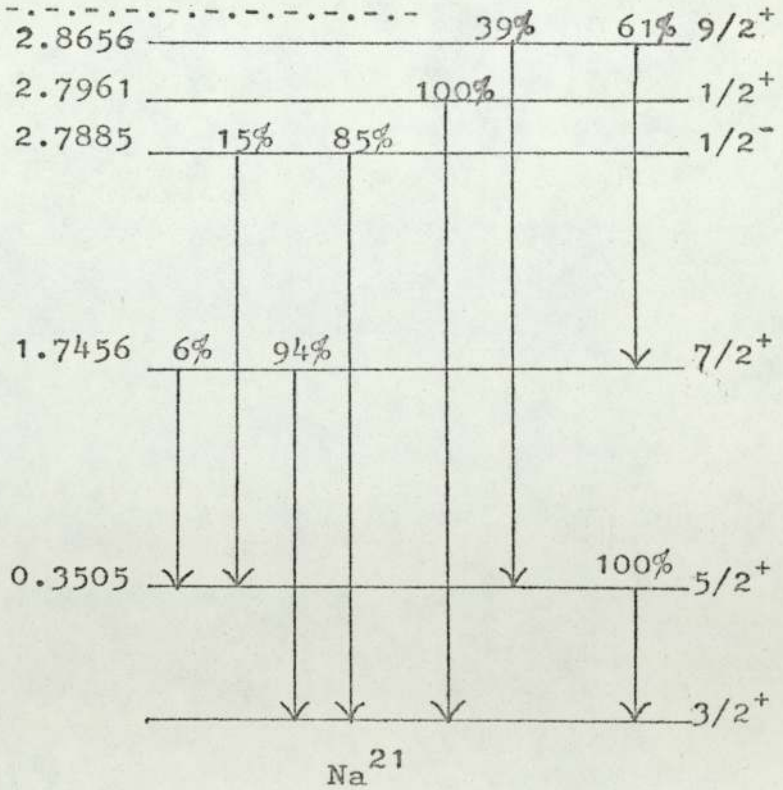
state, (0^+), yield gamma-rays of energy 1·80873 MeV [73]. This
level scheme is not shown, as no other gamma-rays which could be
attributed to transitions in Mg^{26} have been identified.

No evidence is found for gamma-rays resulting from transitions
in Mg^{25}, which has an isotopic abundance of 10·11%.

The higher energy peaks are less clearly identifiable, as
there appear to be several peaks which are not resolved from each
other.   At these gamma-ray energies ($\sim$ 3 MeV), pair production
is an important process in the interaction of the gamma-rays with
the crystal.   This process, leading to the production of the two
0·511 MeV annihilation gamma-rays, may result in the appearance
of first and second escape peaks, in addition to the photopeak,
as either one or both of these quanta escape detection in the
crystal.   This complicates the spectra, both by the appearance of
extra peaks, and by reducing the intensity of the full energy peaks.

From the level scheme, figure 5.2, the gamma-ray energies which
may be expected in this region, resulting from transitions in Mg^{24},
are 2·75 MeV and 2·86 MeV.   The double escape peaks due to higher
energy gamma-rays, 3·87 MeV and 4·24 MeV, could give rise to peaks
at 2·85 MeV and 3·22 MeV.   In this spectrum (figure 5.1), the 2·75
MeV peak due to the 4^+ to 2^+ transition is resolved, but there is
no conclusive evidence for the escape peaks due to partial detection
of this gamma-ray energy.   While there is evidence for this peak in
the spectra at other scattering angles, it is not as well resolved
as shown here.   The other gamma-rays may be present but are not
well resolved.

The gamma-ray energy spectrum resulting from (n,xγ) reactions
in magnesium has been reported by Engesser and Thompson [23].

They find the same gamma-ray energies as reported here, and also evidence for inelastic scattering in Mg^{25} which yields a 1.61 MeV gamma-ray. Nyberg - Ponnert et al [89] have also measured the gamma-ray spectrum produced by 14 MeV neutron bombardment of magnesium with a GeLi detector. They also report the same gamma-ray energies as found here, but find no evidence of scattering in Mg^{25}, in agreement with the present work. Contributions due to other reactions; (n,α), (n,p) and (n,d) are also detected, but are below the discriminator level of the present work.

5.1.2.   The (n,α) Reaction

The 1.37 MeV gamma-ray peak has been attributed to transitions in Mg^{24} produced by neutron inelastic scattering. However there may be a contribution to this peak from the reaction Mg^{24} (n,α) Ne^{21*}, see figure 5.3. Transitions in Ne^{21} from the second excited state, $(7/2^+)$, to the first $(5/2^+)$ excited state result in gamma-rays of energy 1.3951 MeV [73]. The difference between the positions of these two photopeaks being less than 1 channel, they will not be resolved. To find the fraction of gamma-rays in this peak which are due to the (n,α) reaction, the cross-section for the emission of the 1.3951 MeV gamma-ray must be compared with that for inelastic scattering from Mg^{24}, as an examination of the decay scheme, figure 5.2, shows that almost all of the excited states of Mg^{24} decay to the first excited state, resulting in the emission of the 1.37 MeV gamma-ray. The (n,α) cross-section for natural magnesium or the isotope Mg^{24} does not appear to have been measured. However, the cross-section for the production of the 0.352 MeV gamma-ray from Na^{21} produced in the (n,α) reaction on Mg^{24} has been measured as 7.8 ± 1.3 mb/str. at a scattering angle of 80° [89]. This implies an upper limit to the

cross-section for production of the 1·3951 MeV gamma-ray of the same value, if all of the 0·352 MeV gamma-rays result from a cascade process from the 1·7456 MeV level. It seems unlikely, however, that the cross-section for excitation of this $7/2^+$ level is higher than that of the lower, $5/2^+$ level, so the true cross-section for the production of the 1·3951 MeV gamma-ray is probably much less than this figure. In fact, the work of Nyberg - Ponnert [89] shows no gamma-ray of this energy, although their resolution is high enough to distinguish this from the 1·367 MeV gamma-ray. The value of the differential cross-section at 80° for the 1·367 MeV peak was reported [89] as 41·7 ± 6·2 mb/str. The (n,α) reaction is thus neglected in the analysis of this peak.

Gamma-rays from activation of the sample, for example from the (n,p) reaction, have been shown to produce a negligible contribution to the energy spectrum (section 3.12). The gamma-ray energy spectra are thus assumed to result entirely from inelastic scattering in magnesium.

5.1.3.   The Angular Distribution

Analysis of the gamma-ray spectra, as described in the previous chapter, yields the differential cross-section for the production of the 1·37 MeV gamma-ray. The result of this calculation is shown in figure 5.4. The error bars represent the experimental uncertainties described later. The solid line represents a least squares fit to the experimental data points, of an expression of the form;

$$\frac{d\sigma}{d\Omega} = a_o + a_2\, P_2\,(\cos\theta) + a_4\, P_4\,(\cos\theta) \qquad \text{..(3.39)}$$

The least squares fit was performed by computer, as described in

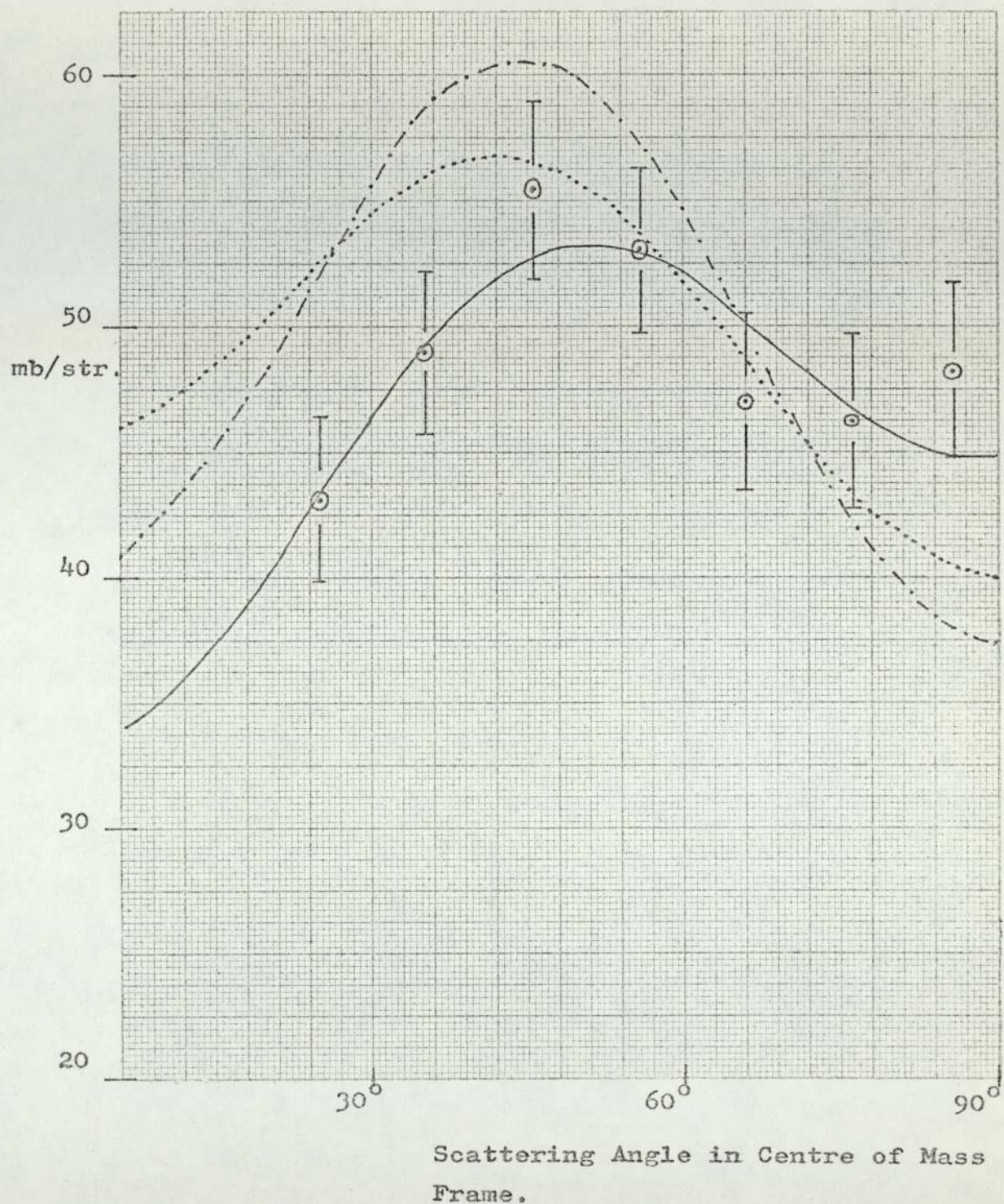Figure 5.4   Differential Cross-Section for Production
              of the 1.37 MeV. Gamma-Ray from Magnesium.
              _____ Present Work
              .... Ref[21]
              .—.—.. Ref[58]

section 3.14, the value of χ^2 per point being 1·10.

Also shown in figure 5.4 are the differential cross-sections
of the 1·37 MeV gamma-ray as reported by Martin and Stewart [21]
and Abbondano et al [58].   The angular distribution of this
gamma-ray has also been reported by Benetskii [19,20] but the
shape of the curve only is given, with arbitrary units. For this
reason, this result is not included in figure 5.4. However, the
general shape of the curve, measured from 45° to 130° is similar
to those shown, and is symmetric about 90°. The previously pub-
lished curves, in figure 5.4, show approximately the same shape
as the present result, although both report higher values at low
angles and lower values at higher angles than the present work.
However, no errors in the coefficients of the curves are quoted,
so is difficult to determine if these differences are significant.
The coefficients of the expansions of the various curves in Legendre
polynomials are shown in table 5.1.

a_0 mb/str.	a_2 mb/str.	a_4 mb/str.	Reference
48·18	-2·32	-12·54	Present Work
49·3	8·9	-12·7	ref. [21]
49·970	10·040	-20·040	ref. [58]

TABLE 5.1.

Coefficients of Legendre Polynomials.

5.1.4. Experimental Errors

The differential cross-section measurements shown in figure
5.4. are calculated, as previously described, from the formula;

$$\frac{d\sigma(\theta)}{d\Omega} = \frac{P(\theta)}{\epsilon(E_\gamma).S(\theta).\phi(\theta).F_1.F_2.N!\overline{x}} \qquad ..(3.38)$$

The experimental uncertainties in most of these factors have already been mentioned. For completeness, they are listed in table 5.2. The error in the peak count, $P(\theta)$, includes only statistical uncertainties. The exact value of these are different at each value of θ, the figure shown is an average. The errors are added quadratically, and the total is plotted in figure 5.4 as the error bars on the experimental points.

Factor	Percentage Error
$P(\theta)$	3·5
$\epsilon(E_\gamma)$	5·0
$S(\theta)$	3·0
$\phi(\theta)$	<0·1
F_1	0·5
F_2	0·5
$N!$	1·0
$\overline{x}$	3·0
TOTAL	7·5

TABLE 5.2.

Experimental Errors.

5.1.5. Total Cross-Section

Table 5.3 shows the various values of the total cross-section, and the differential cross-section at $90°$, for production of the

1.37 MeV gamma-ray by Mg^{24}, which have been published. The values of the total cross-section range from 500 ± 100 mb to 628 ± 66 mb. In view of the experimentsl errors, these results are compatible The values of the differential cross-sections at 90° are more widely varying, ranging from 26.2 ± 6.5 mb to 44.6 ± 3.3 mb. These differences are greater than the experimental errors, although the two latest measurements [21, 58] are in good agreement with the present work, and with each other.

$\frac{d\sigma}{d\Omega}$ (90°) mb/str.	σ_τ mb	Reference	Remarks
44.6 ± 3.3	605 ± 15	Present work	
	590 ± 95	(20)	NaI detector, annular geometry, no T. of F. disc.
40.2	619 ± 60	(21)	NaI det., T. of F. discrimination.
26.2 ± 6.5		(22)	NaI detector, no other details given.
30.9 ± 3.1		(23)	NaI det., no T. of F. disc.
	550 ± 100	(25)	NaI det., T of F. disc., with pulsed beam.
38.4 ± 4.0	628 ± 66	(58)	NaI det., T. of F. disc.
28	500 ± 100	(90)	Stilbene detector, pulse-shape disc., poor resolution.

TABLE 5.3

Values of Cross-section for Production of the

1.37 MeV Gamma-ray from Mg^{24}.

5.2. Chromium

5.2.1. Interpretation of Energy Spectrum

A typical energy spectrum of gamma-rays from 14 MeV neutron interactions in chromium is shown in figure 5.5. This was accumulated at a scattering angle of 40°, (laboratory frame). Background has been subtracted from the spectrum. The spectrum is bounded at the lower end by the discriminator level, set at 1·00 MeV. Only one peak is clearly resolved in the spectrum at 1·43 MeV.

Figure 5.6 shows the level scheme of Cr^{52} as reported by Rapaport [71]. From this the peak at 1·43 MeV is identified as due to transitions from the first excited state (2^+), to the ground state, which result in gamma-rays of energy 1·4342 MeV. Cr^{52} has an isotopic abundance of 83·76%.

Several of the gamma-rays which might be expected from an examination of the level scheme, for example 0·9356 MeV from the 4^+ to 2^+ transition and 0·7440 MeV from the 6^+ to 4^+ transition are not detected as they are below the discriminator level. Other possible gamma-ray energies are 1·214 MeV, 1·332 MeV, and 1·531 MeV. There is no evidence for the presence of any of these peaks, although this may be due to the much stronger intensity of the 1·43 MeV peak.

There is some evidence for the detection of gamma-rays at 2·7 MeV to 3·0 MeV, although no peaks are resolved in this region. The level scheme of Cr^{52} offers no explanation of the possible origin of gamma-rays of these energies. Other isotopes of chromium, Cr^{50}, Cr^{53} and Cr^{54} are also present in the sample of the natural element, with abundances of 4·41%, 9·54% and 2·61% [88] respectively. Examination
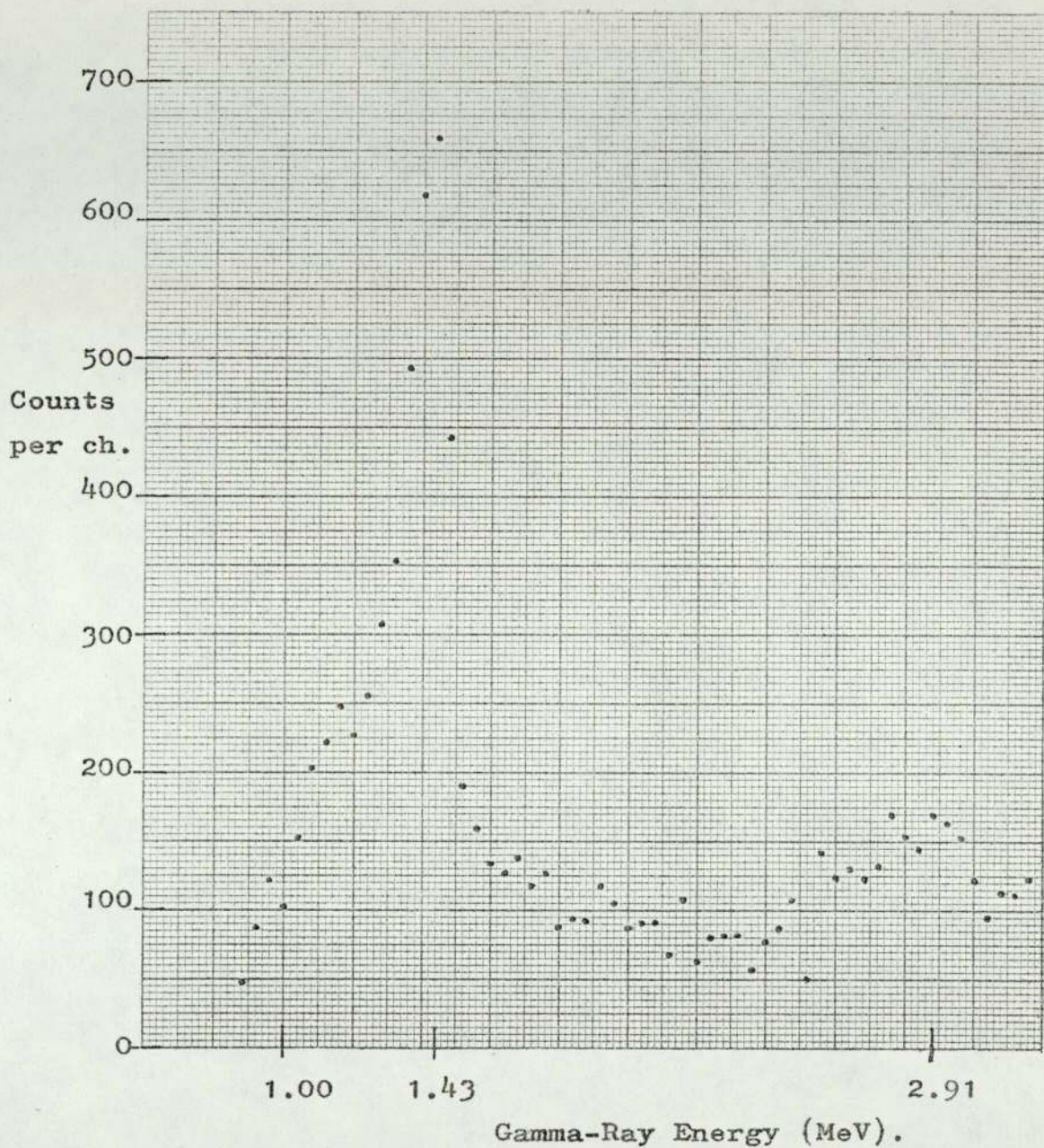
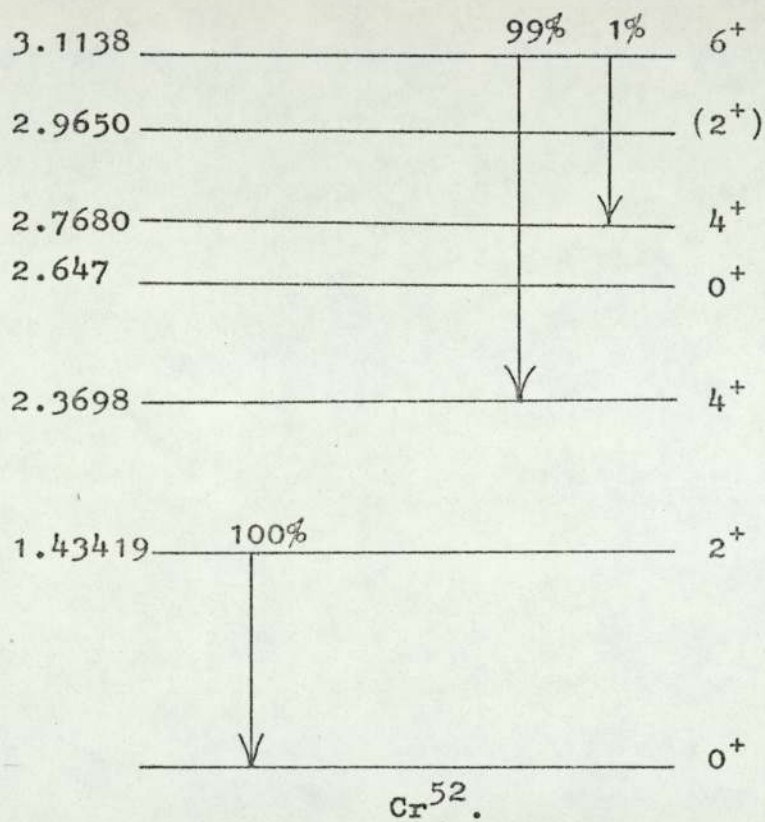Figure 5.5   Spectrum of Gamma-Ray Energies from
Chromium.

Figure 5.6   Level Scheme and some Branching Ratios[71] of Cr^{52}.

of the energy levels of these isotopes shows no transitions which
would give rise to gamma-rays of energy greater than 2 MeV, in the
intensity required to explain this region of the spectrum. However,
it is noted that very little information is given about branching
ratios, so it is possible that these gamma-rays may result from
transitions between higher levels in these isotopes, or in Cr^{52},
for which information is not available at present.

5.2.2. The (n,α) and (n,2n) Reactions

It is possible that the (n,α) and (n,2n) reactions in Cr^{52}
may result in the emission of gamma-rays which cannot be resolved
by the system from the 1·43 MeV peak:

$$Cr^{52} \ (n,\alpha) \ Ti^{49}$$
$$Cr^{52} \ (n,2n) \ Cr^{51} \xrightarrow{e.c.} V^{51}$$
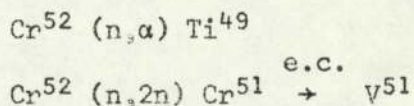
Ti^{49} is stable and Cr^{51} decays by electron capture to V^{51} with a
half-life of 27·8 days. Thus if Ti^{49} and Cr^{51} are produced in an
excited state, they will emit gamma-rays in decaying to the ground
state. Ti^{49} may emit the gamma-ray energies 1·31 and 1·378 MeV,
and Cr^{51}, 1·36 and 1·55 MeV.

The (n,α) cross-section for chromium does not appear to have
been measured at a neutron energy of 14 MeV, although for neutron
energies averaged over a fission-spectrum, the cross-section is
reported as only 0·35 mb [91]. The (n,2n) cross-section is 280 mb
[87], but the excitation of the Cr^{51} nucleus after the reaction
is not reported.

Both of these reactions are neglected, for the following

reason. Measurements of the total cross-section for the production
of the 1·43 MeV gamma-ray from Cr^{52} have been reported by Abbondano
et al [58] and Breunlich et al [92]. The former used a NaI scintil-
lator as the gamma-detector and hence the system was unable to
resolve the gamma-rays mentioned above from the 1·43 MeV peak. The
latter used a GeLi detector, which was able to resolve this peak
from the others. The results they report (table 5.5) are, however,
in good agreement, within the experimental errors. Assuming that
neither result is subject to systematic error, this suggests that
the (n,α) and $(n,2n)$ reactions are negligible in their contribution
to the 1·43 MeV gamma-ray peak. This is thus attributed to inelastic
scattering only.

5.2.3. The Angular Distribution

The differential cross-section of the 1·43 MeV gamma-ray cal-
culated from equation 3.38 is shown in figure 5.7. Again the solid
line represents a least-squares fit to the experimental data points
of the Legendre polynomial expansion. The differential cross-section
is represented by;

$$\frac{d\sigma}{d\Omega} = 79\cdot75 \pm 2\cdot47 - (25\cdot57 \pm 4\cdot80)\, P_2(\cos\theta) - (28\cdot82 \pm 8\cdot13)\, P_4(\cos\theta)$$

The value of χ^2 per point is 0·92.

Also shown in figure 5.7 is the differential cross-section for
production of the 1·43 MeV gamma-ray from Cr^{52}, as published by
Abbondano et al [58]. The shape of the two angular distributions
are quite different, and there is no obvious explanation for this
discrepancy.
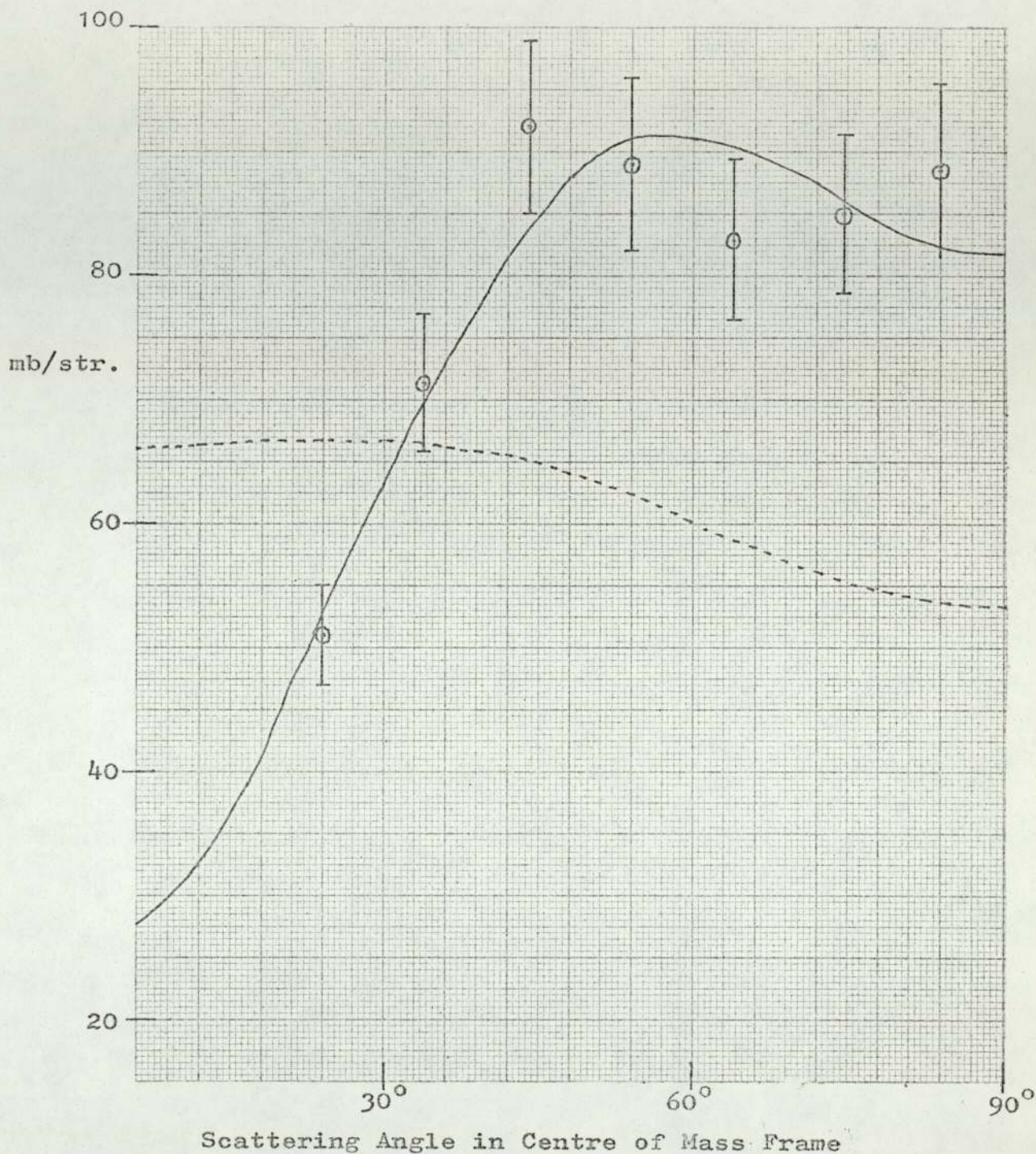
Figure 5.7 Differential Cross-Section for Production
            of the 1.43 MeV Gamma-Ray from Chromium.

—————— Present Work.

- - - - - - ref$^{(58)}$.

5.2.4. Experimental Errors

The experimental errors in the factors in the formula 3.38, are shown in table 5.4. They are substantially the same as for the magnesium results.

Factor	Percentage Error
$P(\theta)$	3·1
$\varepsilon(E_\gamma)$	5·0
$S(\theta)$	3·2
$\phi(\theta)$	<0·1
F_1	0·5
F_2	0·5
N'	2·0
$\bar{x}$	3·2
TOTAL	7·72

TABLE 5.4.

Experimental Errors.

5.2.5. Total Cross-section

Table 5.5 shows the values of the total cross-section, and of the differential cross-section at 90°, which have been published by various authors. The two previous measurements of the total cross-section agree within the experimental errors, but are substantially smaller than the present result. The values of the differential cross-sections are spread widely, and again the

present result is the highest, but in this case the two other
published results are significantly different from each other.

$\frac{d\sigma}{d\Omega}$ (90°) mb/str.	σ_τ mb	Reference	Remarks
81·7 ± 6·3	1002 ± 31	Present work	
23·6 ± 8		(22)	NaI detector, no other details.
53·5 ± 4·0	757 ± 56	(58)	NaI det. T. of F. disc.
	727 ± 100	(92)	GeLi detector.

TABLE 5.5.

Values of the Cross-section for Production of the
1·43 MeV Gamma-ray from Cr^{52}

5.3.   Iron

5.3.1.   Interpretation of Energy Spectrum

Figure 5.8 shows a gamma-ray energy spectrum resulting from
14 MeV neutron reactions in iron.   It was accumulated at a labora-
tory scattering angle of 40°, and background has been removed.
The lower boundary of the spectrum is set by the discriminator level
of 0·7 MeV.   Several peaks are resolved, the most intense being at
0·84 MeV.   Other peaks are seen at 1·24, 1·81, 2·13 and 2·78 MeV.

The level scheme of the nucleus Fe^{56}, (isotopic abundance
91·52% [88]), is shown in figure 5.9, as reported by Rao [72].
From this, several gamma-ray peaks may be identified immediately.
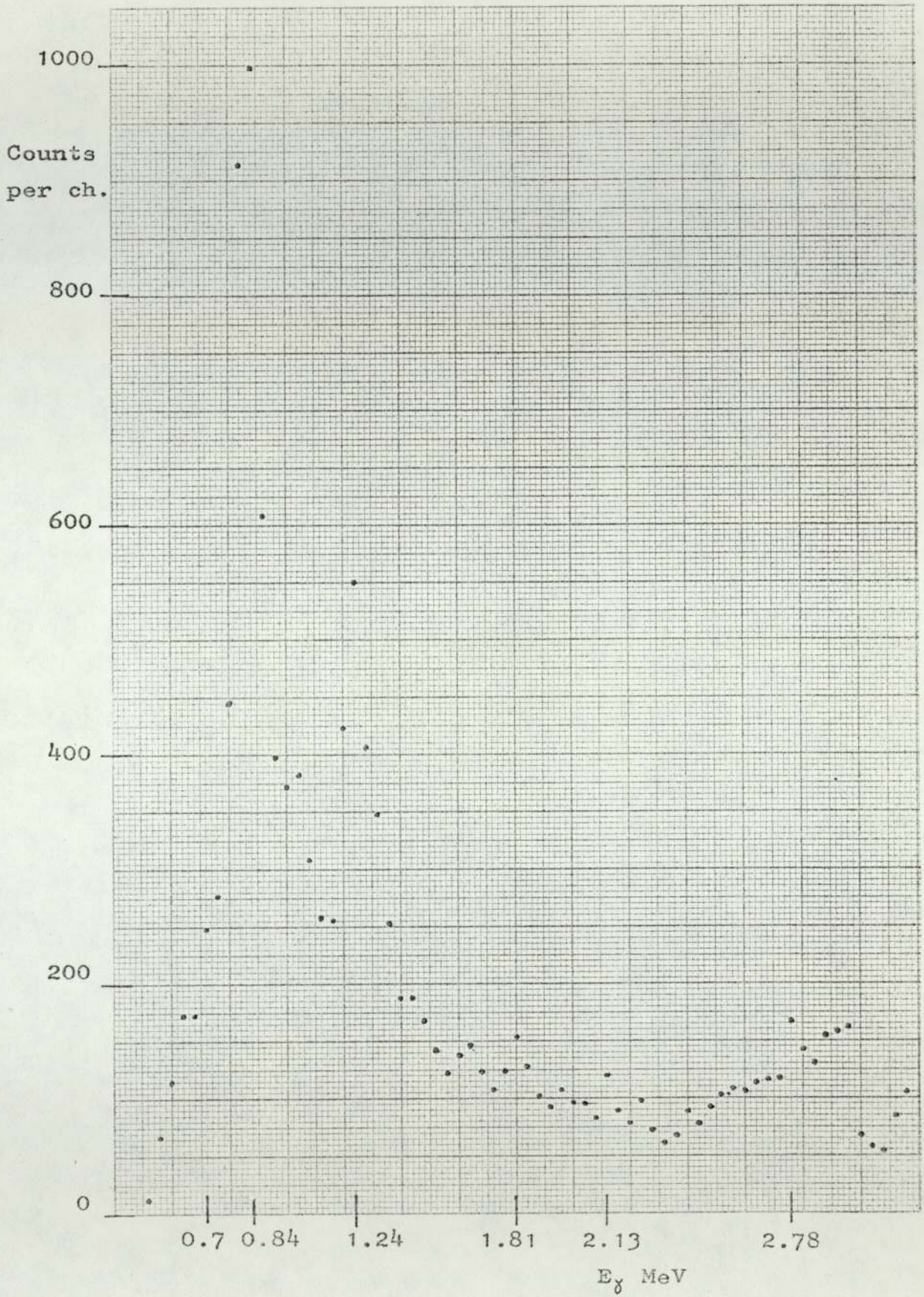The most intense peak, at 0·84 MeV, is due to transitions from

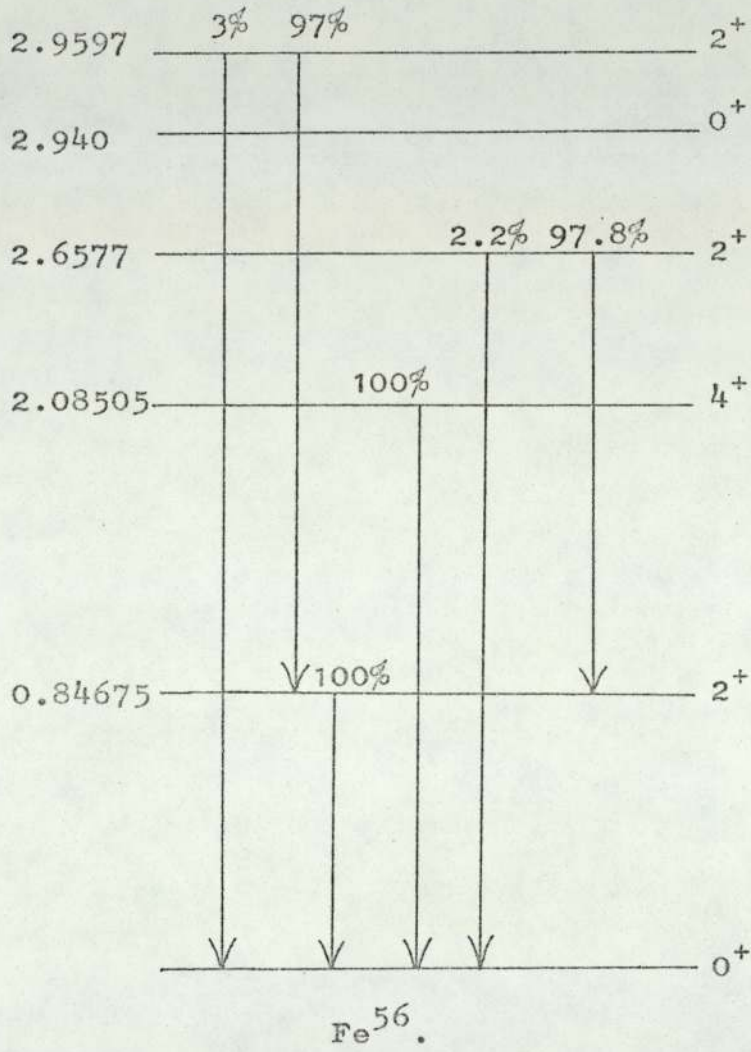Figure 5.8   Spectrum of Gamma-Ray Energies from
Iron.

Figure 5.9   Level Scheme and Branching Ratios[72]
          of Fe^{56}.

the first excited state, (2^+), to the ground state, which result in the emission of gamma-rays of energy 0·84675 MeV. The peak second in intensity, at 1·24 MeV, is due to transitions between the second excited state, (4^+), at 2·08505 MeV, and the first excited state, which yield gamma-rays of energy 1·2383 MeV.

There is also clear evidence for the presence of a peak at 1·81 MeV, due to transitions between the third and first excited states, $(2^+$ to $2^+)$. This third level, at 2·6577 MeV decays with 97·8% probability [55] to the first excited state, yielding the 1·8110 MeV gamma-ray, and with 2·2% probability to the ground state, emitting a gamma-ray of energy 2·6577 MeV. There is no evidence for the presence of a peak at 2·66 MeV, but in view of the low yield, this is not surprising. There appears also to be a peak at 2·11 MeV, probably due to transitions from the fourth and fifth levels, at 2·940 and 2·9597 MeV, to the first excited state. The peak at 2·78 MeV is probably the first escape peak of the gamma-ray of energy 3·253 MeV produced in transitions from the 4·099 MeV level to the first excited state.

The other naturally occuring isotopes of iron are Fe^{54} and Fe^{57}, with abundances 5·84% and 2·17% respectively. The isotope Fe^{57} can be expected to yield predominantly gamma-rays of energy below 0·7 MeV. Since these are below the discriminator level, this isotope is not expected to contribute to the spectrum. The isotope Fe^{54} yields gamma-rays of energy 1·409 MeV [55] from the transition from the first excited state to the ground state, $(2^+$ to $0^+)$. There is some evidence for this gamma-ray, but it is not clearly resolved from the Compton edge of the 1·24 MeV peak, and from the 0·84 MeV peak.

The gamma-rays mentioned above have also been reported by Jönsson et al [93], who measured the gamma-ray spectrum from neutron bombardment of iron, using a GeLi detector. They also report several gamma-rays from 1·3 MeV to 1·8 MeV, and at 2·5 MeV, which are not resolved by the present system, due to the poorer energy resolution of the NaI detector used in this work.

5.3.2. Other Reactions

Although the observed spectrum has been accounted for by considering only inelastic neutron scattering in Fe^{56}, other reactions may yield gamma-rays in the range of the spectrum. The (n,2n) reaction may result in the emission of gamma-rays of energy 0·805, 0·930, 1·21, and 1·316 MeV [55] among others, from the decay of higher states of Fe^{55}, formed in this reaction, to the ground state. Fe^{55} decays to Mn^{55} by electron capture, with a half-life of 2·6 years. Thus if, after formation, the Fe^{55} nucleus is in an excited state, it will probably decay to the ground state with the emission of gamma-rays, before it decays to Mn^{55}. The peaks due to detection of the gamma-rays of 0·805 and 0·930 MeV will be one and two channels respectively from the centre of the 0·84 MeV peak, and hence will not be resolved from it.

Jönsson et al [93] have found evidence of the 0·930 MeV gamma-ray, but no evidence of the 0·805 and 1·21 MeV gamma-rays. The other peaks they report due to (n,2n) reactions are at 0·412 MeV, (below the discriminator level of the present work), and at 1·316 MeV, which would not be resolved by the present system from the 1·24 MeV peak. The number of counts in the 0·84 MeV peak should thus be corrected for a possible contribution due

to the 0·930 MeV peak from Fe^{55}. Jönsson et al report the differential cross-section at 80° for the production of the 0·930 MeV gamma-ray as $4·4 \pm 0·4$ mb compared with $74·4 \pm 0·7$ mb for the 0·84 MeV gamma-ray. These values are averages of the differential cross-section over the range 50° to 110° due to the large angular acceptance of the detector. The angular distribution of the 0·930 MeV gamma-ray is thus not known. The present work yields a value of the differential cross-section for the 0·84 MeV gamma-ray at 80° of $63·9 \pm 4·2$ mb. The disagreement between this value and that of Jönsson is not unexpected in view of the angular uncertainties of the latter work. Because of this, and the small value of the cross-section for the 0·930 MeV gamma-ray relative to that of the 0·84 MeV gamma-ray, no correction was made for the (n,2n) contribution. This reaction does, however, constitute a source of systematic error in the differential cross-section, of the same order as the experimental uncertainties. These cross-sections have also been reported by Engesser and Thompson [23], who find the differential cross-section at 90° for 0·85 and 0·92 MeV gamma-rays as $56·9 \pm 5·8$ mb and $11·7 \pm 3·9$ mb respectively. However, these researchers used a NaI crystal as the gamma-ray detector, and in their spectrum, the 0·92 MeV peak is not completely resolved. Since Jönsson et al used a GeLi detector with greatly superior energy resolution, their values are prefered.

Another reaction which should be considered is, Fe^{56} (n,d) Mn^{55}. The stable isotope, Mn^{55} may yield gamma-rays of 0·983 MeV and 0·857 MeV in transitions from the second excited state, $(9/2^-)$, to the ground state, $(5/2^-)$, or the first excited state, $(7/2^-)$. Again, these could not be resolved from the 0·84 MeV peak by the present system. However, neither of these gamma-ray

energies are reported by either Jönsson or Engesser and Thompson.
The size of the (n,d) cross-section may be estimated by subtracting
from the total cross-section for non-elastic reactions in Fe^{56}, the
sum of all other non-elastic reactions which have been measured.
This gives an upper limit to the (n,d) cross-section. The total
non-elastic cross-section is 1·36 ± 0·03 barns [87], while cross-
sections for the (n,2n), (n,p), (n,np), (n,α) and (n,n') reactions
are respectively 440 ± 90 [87], 112 ± 6[87], 78 ± 40[62], 60[89] and 620 ±
160 [94] mb. Thus an upper limit for the (n,d) reaction is 36 ±
190 mb, and this is seen to be negligible in comparison with
inelastic scattering. It is thus seen that the gamma-ray spectra
result mainly from neutron inelastic scattering in the most
abundant isotope Fe^{56}.

5.3.3. The Angular Distribution

The angular distribution found from analysis of these spectra
is shown in figure 5.10, for production of the 0·84 MeV gamma-ray
by Fe^{56}. The solid line again represents a least-squares fit to
the experimental data points, which is described by the equation;

$$\frac{d\sigma(\theta)}{d\Omega} = (64\cdot83 \pm 1\cdot67)-(9\cdot22 \pm 3\cdot49)P_2(\cos\,\theta)-(19\cdot10 \pm 5\cdot75)P_4(\cos\,\theta)$$

The value of χ^2 per point is 0·556.

Also shown in figure 5.10 are the angular distributions as
measured by Martin and Stewart [21] and Abbondano et al [58].
There is reasonable agreement between the present results and
those of Abbondano, although the present work finds a greater
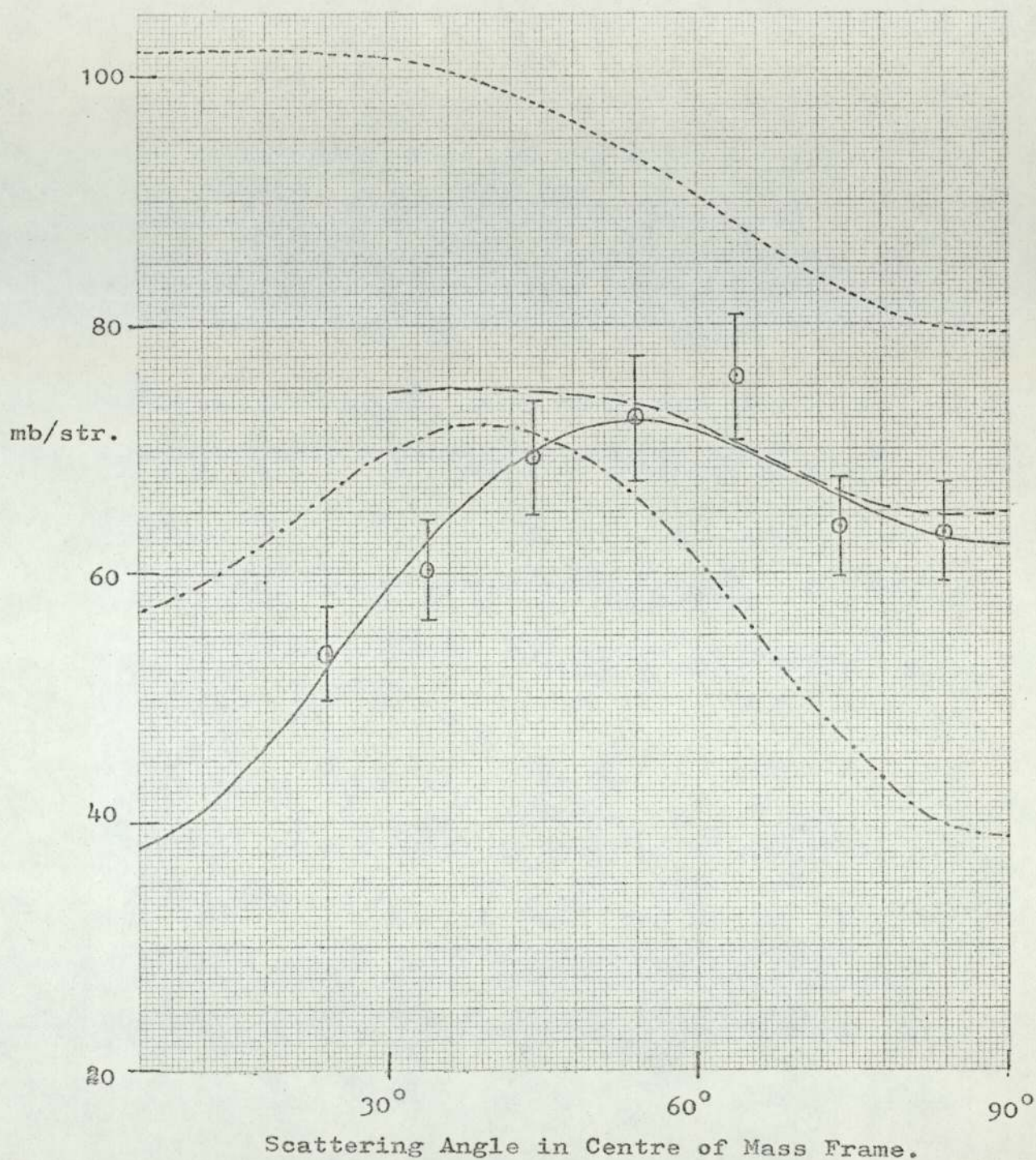amount of scattering at higher angles. The angular distribution

Figure 5.10 Differential Cross-Section for Production
           of the 0.84 MeV. Gamma-Ray from Iron.

——————— Present Work
— — — — — ref[21]
— · — · — ref[58]
— — — — ref[95]

reported by Martin and Stewart does not agree with either of
the other measurements, in shape or in absolute value. Haouat
et al [95] have also measured the angular distribution of the
0·84 MeV gamma-ray. Although they have fitted a Legendre poly-
nomial expansion to their results, they report only the graphical
form of the resulting curve, not the values of the coefficients.
The representation of their results in figure 5.10 is thus subject
to greater error than are the other curves. There is nevertheless,
quite good agreement with the present results. The discrepancies
between these various measurements cannot be attributed to differ-
ences in technique, as two [21, 58] used substantially the same
technique as the present work, namely time of flight discrimination
with the associated particle method, achieving detection of gamma-
rays by means of a NaI crystal. Hacuat et al [95], however, used
the pulsed beam method for time of flight discrimination, and a
GeLi gamma-ray detector with a NaI anticoincidence shield. In
spite of this difference in techniques, these results show the
best agreement with the present work. Table 5.6 lists the values
of the coefficients of the Legendre polynomial expansion, where
these have been reported.

a_0 mb/str	a_2 mb/str	a_4 mb/str	Reference
64·83 ± 1·67	-9·22 ± 3·49	-19·10 ± 5·75	Present work
90·6	17·8	- 6·6	(21)
57·420	20·750	-22·040	(58)

TABLE 5.6.

5.3.4. Experimental Errors

The experimental errors in the factors of equation 3.38, which is used to calculate the differential cross-section, are listed in table 5.7. As before, they are added quadratically to obtain the total error, which is represented by the error bars in figure 5.10.

Factor	Percentage Error
$P(\theta)$	3·0
$\epsilon(E_\gamma)$	5·0
$S(\theta)$	2·2
$\phi(\theta)$	<0·1
F_1	0·5
F_2	0·5
$N^\imath$	2·2
$\bar{x}$	2·5
TOTAL	7·1

TABLE 5.7.

Experimental Errors.

5.3.5. Total Cross-section

The total cross-section and the differential cross-section at 90°, for the production of the 0·84 MeV gamma-ray in Fe^{56}, published by various workers, are shown in table 5.8.

σ_τ mb	$\frac{d\sigma}{d\Omega}$ (90°) mb/str	References
814 ± 21	62·28 ± 4·42	Present work
1138 ± 135	79·2	(21)
	30·2 ± 9·1	(22,98)
	56·9 ± 5·8	(23)
	52 ± 8	(24)
	74·4 ± 0·7	(93)
	49·0 ± 13·0	(94)
660 ± 80		(19)
1228 ± 150		(96)
1268 ± 150		(97)
721 ± 76	45·6 ± 5·0	(58)

TABLE 5.8.

Values of the Cross-section for Production of the

0·84 MeV Gamma-ray from Fe^{56}.

As previously described, the value of σ_τ for the present work
is $4\pi a_0$. The values of σ_τ in the above table fall into two groups,
those of Abbondano et al [58], Benetskii [19], and the present work,
which are probably compatiable within the experimental uncertainties,
but which differ significantly from the second group, the work of
Martin and Stewart [21, 97], and Bezotosnyi et al [96]. It is not
clear whether Bezotosnyi measured the angular distribution of the
gamma-ray, or if the total cross-section was obtained by measuring
the differential cross-section at one angle, and multiplying by 4π.
The discrepancy between these two groups does not appear to be due
to differences in technique, as time of flight discrimination,

using the associated particle method was used by members of both groups; [59, 21, 97] and the present work. Benetskii [19] monitored the alpha-particle flux, and Bezotosnyi et al [96] do not report on the details of the experimental method.

The values of the 90° differential cross-section are spread over a wide range from $30\cdot2 \pm 9\cdot1$ mb/str [22, 98] to $79\cdot2$ mb/str [21]. The most accurate value appears to be $74\cdot4 \pm 0\cdot7$ mb/str [93], but this value is averaged over the scattering angles 50° - 110° so it does not represent accurately the value of the differential cross-section at 90°. The values published in references [23, 24, 94, 58] and the present work are probably compatible within the experimental errors.

5.4. Comparison of Theory and Experiment

For the comparison of the angular distributions, as predicted by the coupled channels theory, with the experimental results, all of the angular distributions have been normalized by setting the value of a_o to unity. This means that the areas under all the curves are equal, being given by 2π, as only the range 0° to 90° is shown. Comparison of the shapes of the angular distributions is thus separated from the comparison of the absolute values of the cross-sections.

Figures 5.11 to 5.16 show the normalized angular distributions for Mg^{24}, Si^{28}, S^{32}, Ti^{48}, Cr^{52}, and Fe^{56}, resulting both from the theory, as described in chapter 4, and from the experimental measurements. For the nuclei Mg^{24}, Cr^{52} and Fe^{56} the experimental data is that of the present work, while for the nuclei Si^{28}, S^{32} and Ti^{48}, the experimental results of Connell [17] are used. These

Scattering Angle in Centre of Mass Frame

Figure 5.11 Normalised Angular Distribution for the
1.37 MeV gamma-ray from Mg^{24}.

—————— Theoretical Result.

— — — — — — Experimental Result.

Figure 5.12 Normalised Angular Distribution for the
1.78 MeV gamma-ray from Si^{28}.
—————— Theoretical Result.

- - - - - - Experimental Result.

Figure 5.13   Normalised Angular Distribution for the
             2·24 MeV gamma-ray from S^{32}.

—————————   Theoretical Result.

- - - - - -   Experimental Result.

Figure 5.14   Normalised Angular Distribution for the
             0·99 MeV gamma-ray from Ti^{48}.

─────────────   Theoretical Result.

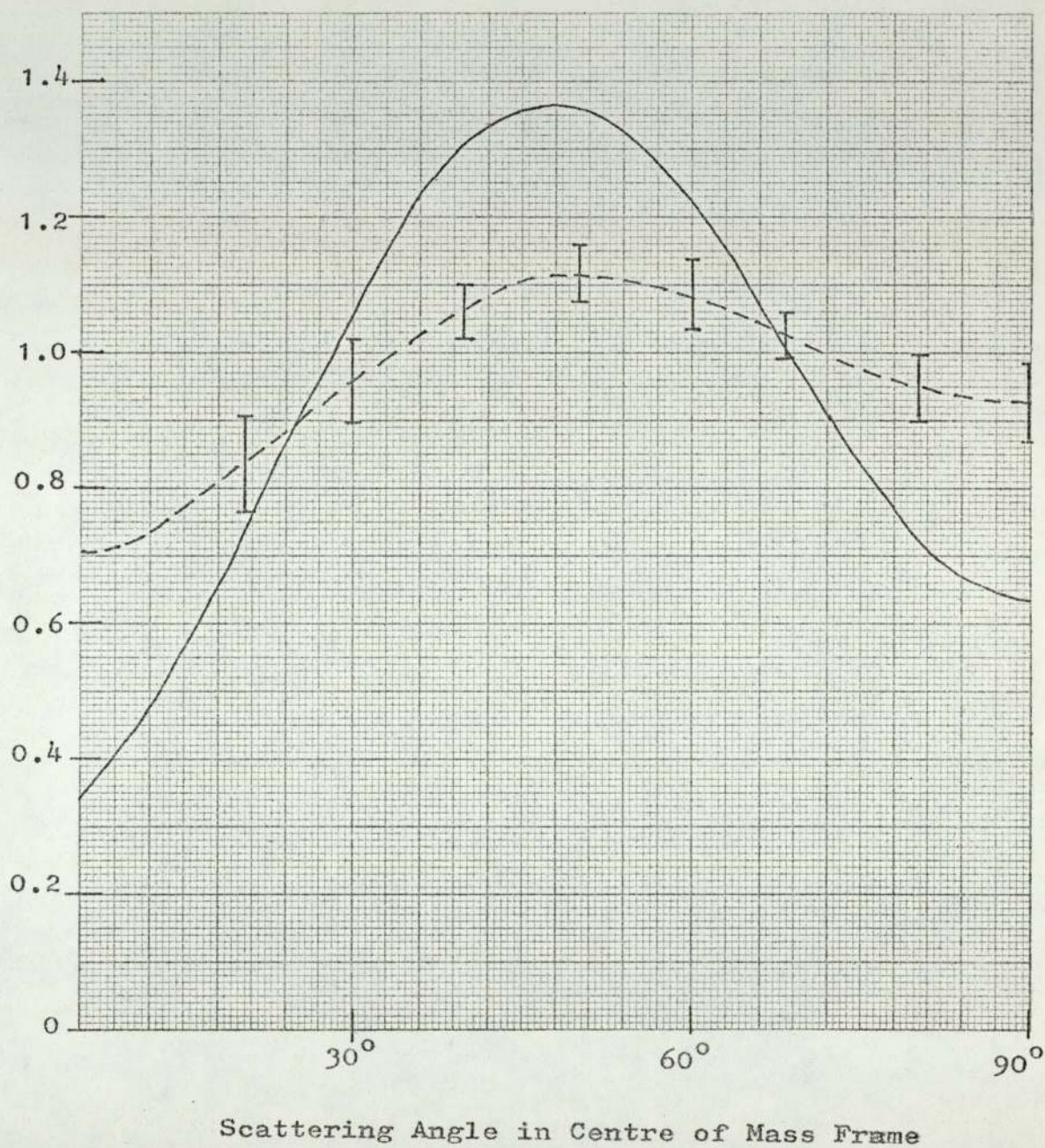─ ─ ─ ─ ─ ─   Experimental Result.

Figure 5.15 Normalised Angular Distribution for the
1.43 MeV gamma-ray from Cr^{52}.

—————————— Theoretical Result.

— — — — — — Experimental Result.
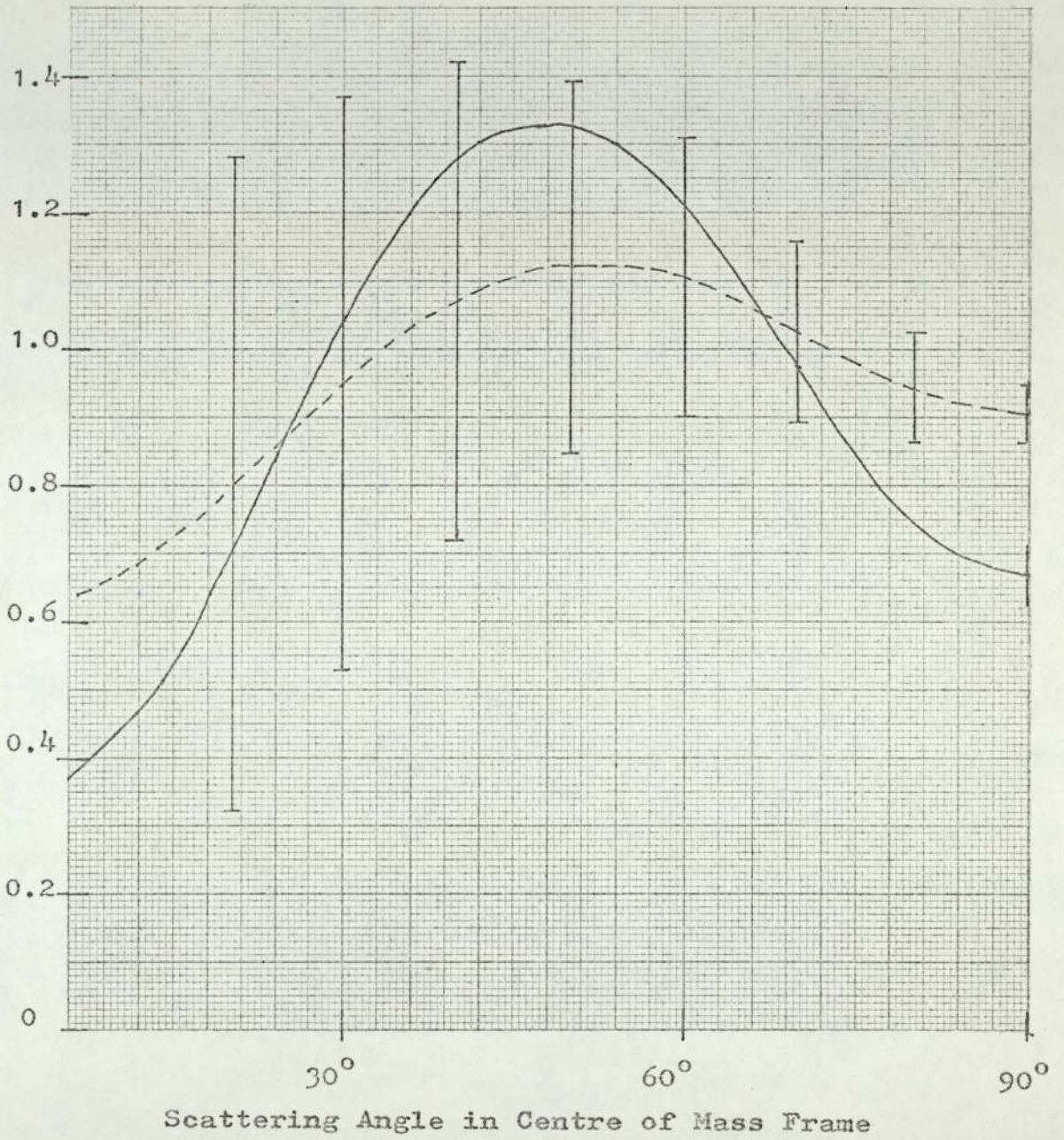
Figure 5.16   Normalised Angular Distribution for the
              0.84 MeV gamma-ray from Fe^{56}.

———————————   Theoretical Result.

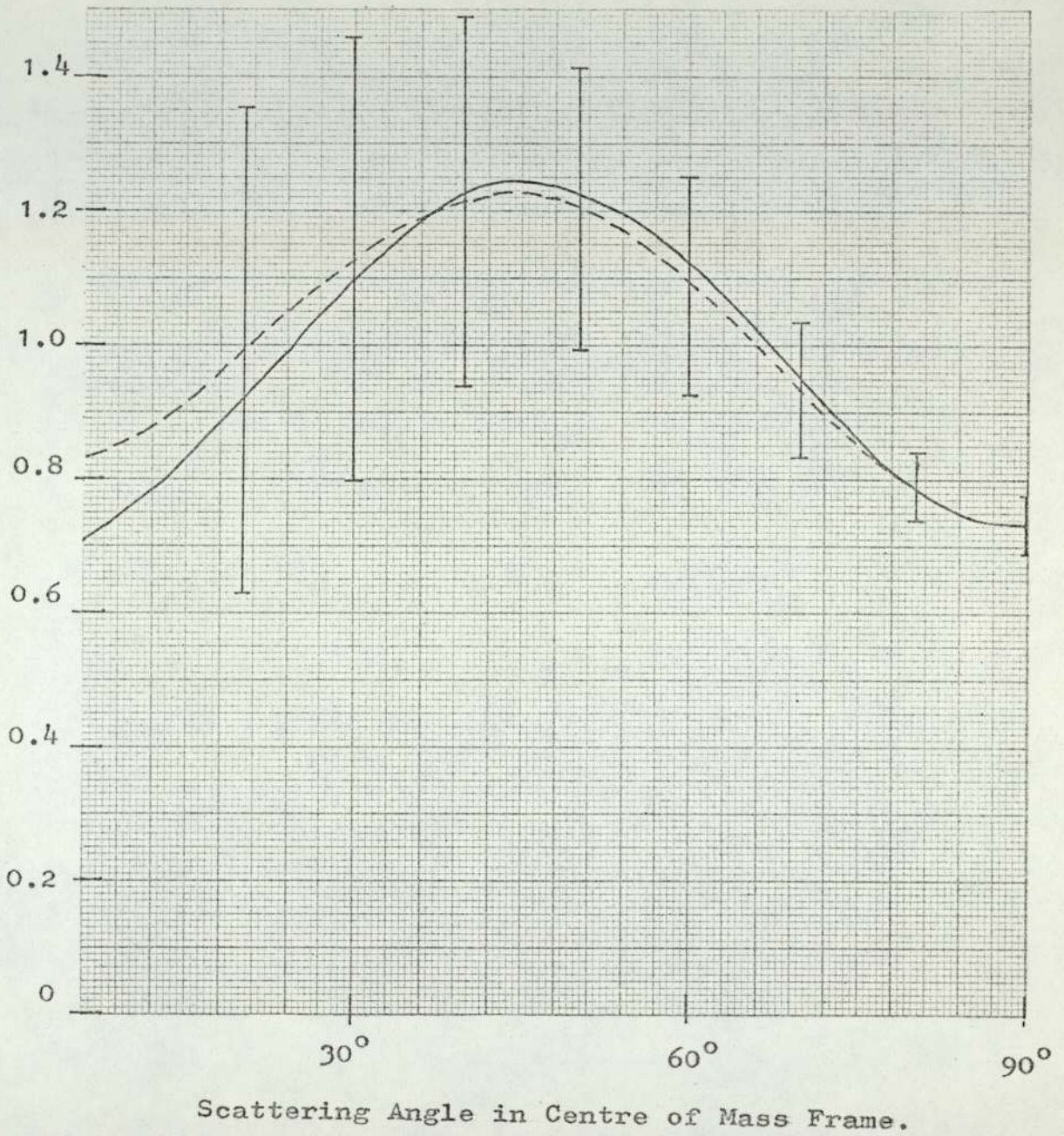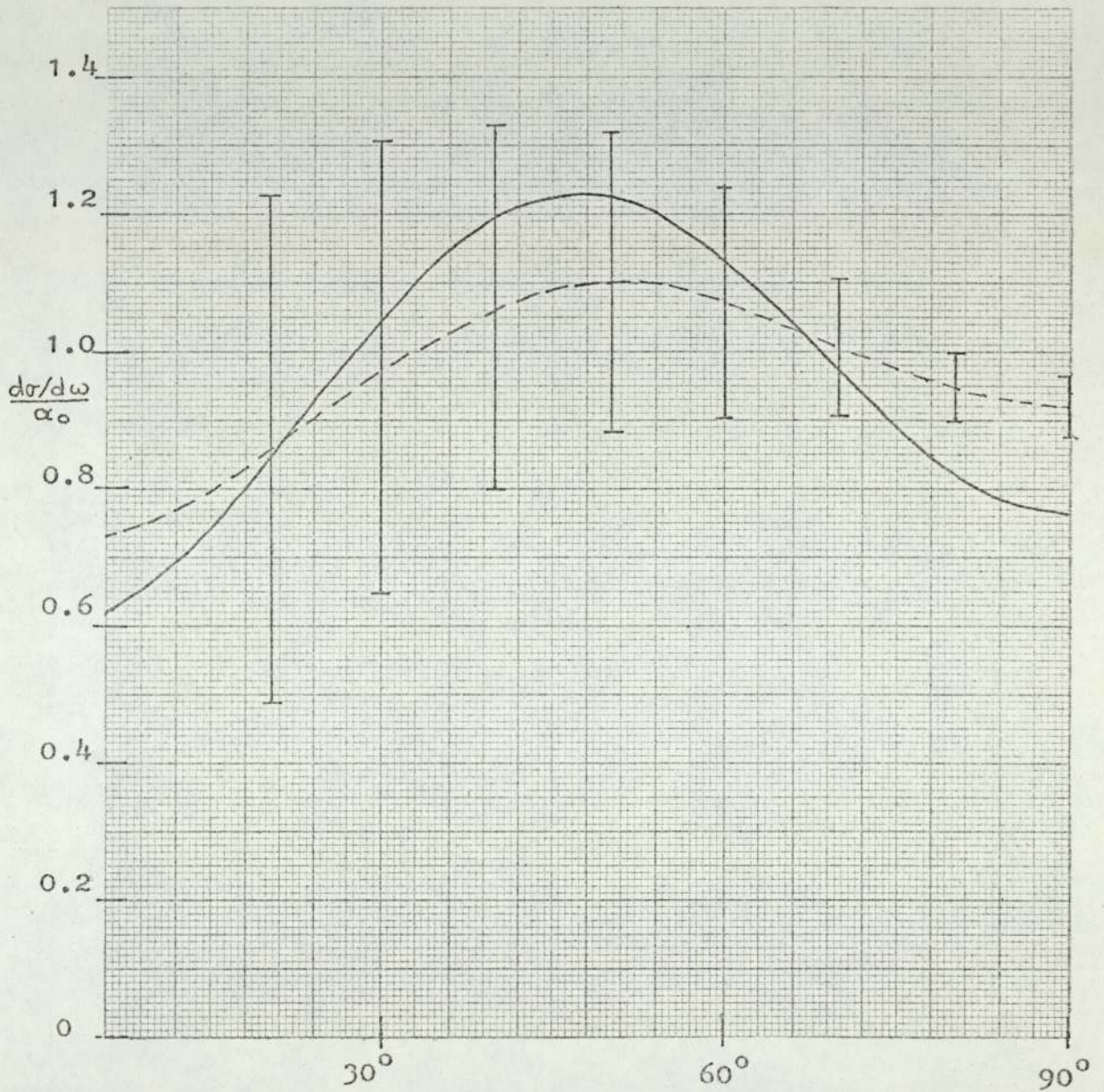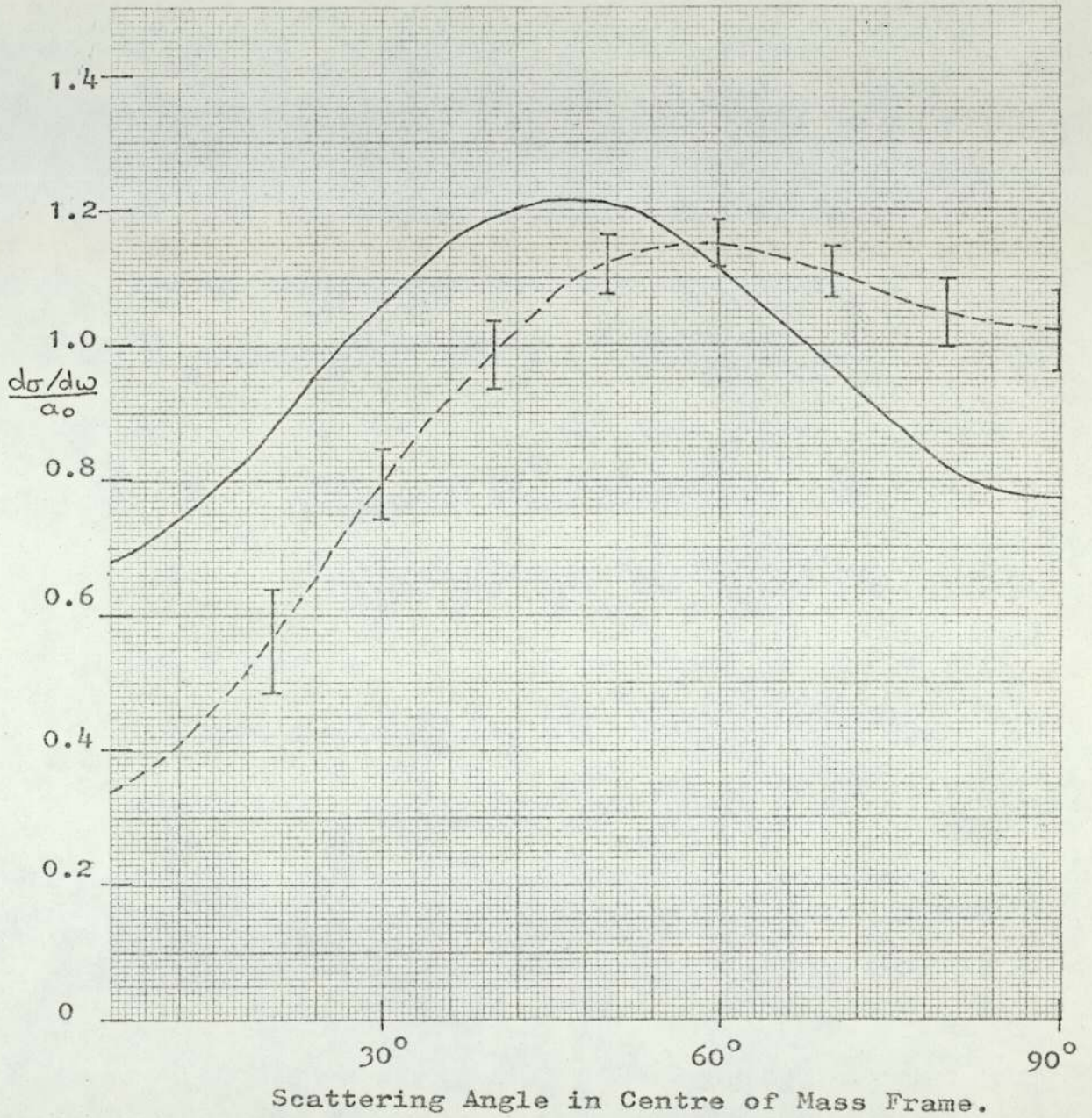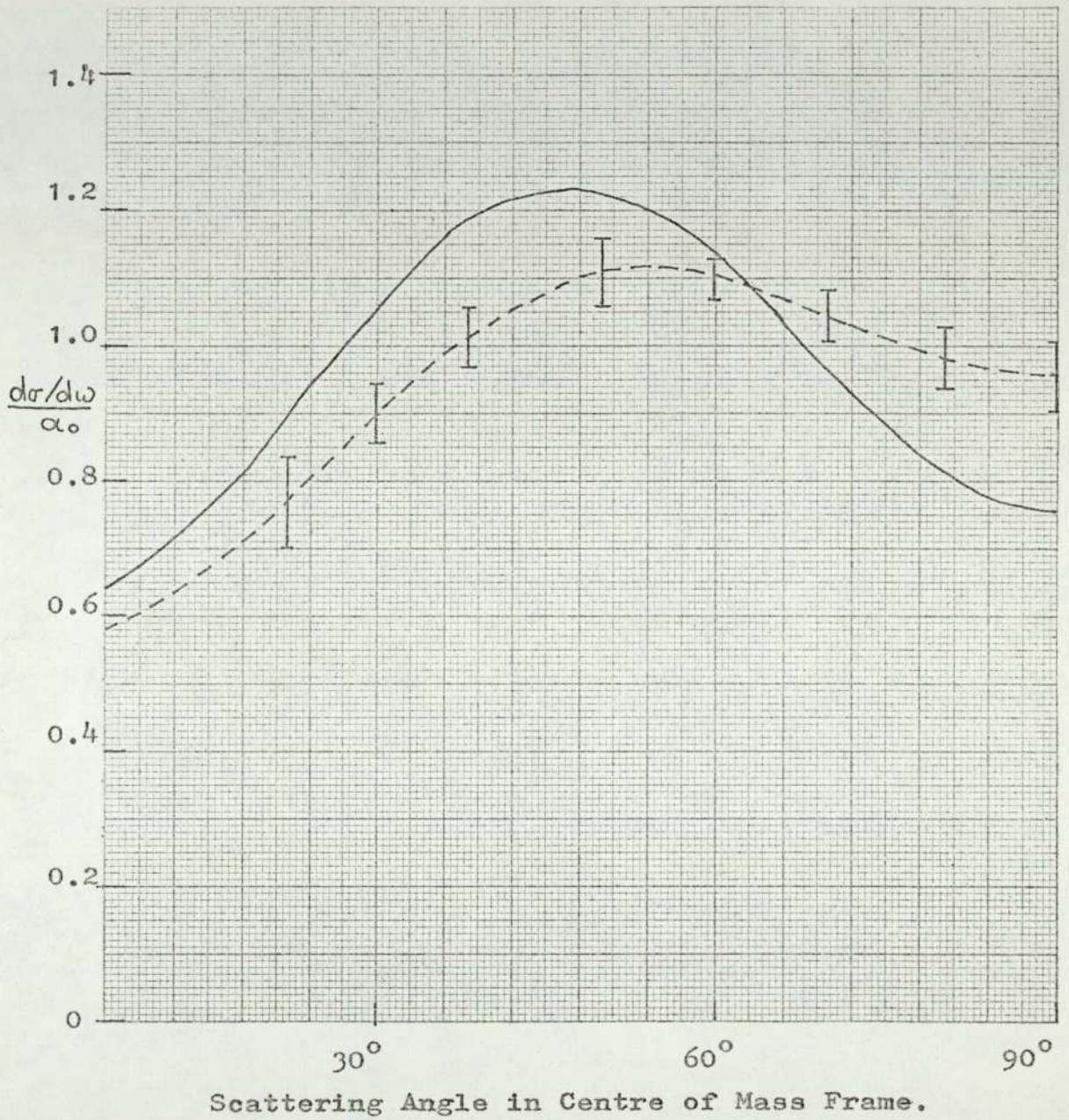— — — — ·—   Experimental Result.

latter results were expressed in the form of a cosine series;

$$\frac{d\sigma(\theta)}{d\Omega} = b_o + b_2 \cos^2\theta + b_4 \cos^4\theta \qquad ..(3.40)$$

as described in section 3.14. To normalize these results, the co-
efficient a_o is calculated from the equation [80],

$$a_o = b_o + \frac{b_2}{3} + \frac{b_4}{5} \qquad ..(5.1)$$

The error bars on these angular distributions 5.11 to 5.16 are
found from the uncertainties in the coefficients "a" or "b".
Following from equations 3.39 and 3.40 , the errors in the
differential cross-section at a scattering angle θ, $(\delta(\theta))$,
are given by either,

$$\delta(\theta) = (\delta a_o + (\delta a_2 P_2(\cos \theta))^2 + (\delta a_4 P_4(\cos \theta))^2)^{\frac{1}{2}} \qquad ..(5.2)$$

or,

$$\delta(\theta) = (\delta b_o^2 + \delta b_2^2 \cos^4\theta + \delta b_4^2 \cos^8\theta)^{\frac{1}{2}} \qquad ..(5.3)$$

where δx is the error in the coefficient x. The large error
bars at low scattering angles, in figures 5.12 to 5.14, illustrate
the difficulties inherent in the $\cos^2\theta$ expansion, and are due to
the increasing value of $\cos\theta$ as θ approaches zero. This effect
is also present in the Legendre polynomial expansion, although
it is much less marked. In both cases, the comparatively large
errors in this region of low scattering angle may also reflect
the fact that no measurements have been taken below 30°, so the
curves here are extrapolated from the region where they have
been determined.

It can be seen that the agreement in the shapes of the angular
distributions is good in some cases, for example, S^{32} and Ti^{48},
while it is less good for the other nuclei. In general, the
theoretical curves show more asymmetry than the experimental
results, if this is defined as the difference between the maximum
and minimum of the curve, divided by their sum. Also, the theoretical
curves predict less scattering at higher angles than is found experi-
mentally. The overall shapes of the experimental curves are, never-
theless, reasonably well represented by the theoretical curves, so
it may be concluded that the coupled channels approach, even in the
first approximation shown here, produces a moderately good prediction
of the experimentally measured angular distributions.

It is not immediately obvious why the agreement between theory
and experiment is better in some nuclei than others, since they all
have the same spin and parity values. Further investigation of the
effect of higher levels in the nuclei concerned may explain this,
although in view of the uncertainties in the experimental results,
the close agreement in the case of S^{32} may be fortuitous.

5.4.1. Absolute Values of the Cross-sections

The absolute values of the total cross-sections are shown in
table 5.9, for production of the gamma-ray of the energy listed,
by the corresponding nucleus. It can be seen immediately that the
experimentally measured values are much higher than those predicted
theoretically, in some cases, by a factor of 40. This is, however,
expected, since the coupled channels calculation took into account
only scattering from the first excited state. The relevant gamma-
ray is however, also produced by cascades; the nucleus may be excited

to a higher level by the neutron scattering event and it then
decays through various intermediate levels to the first excited
state. This then decays to the ground state producing the gamma-
ray concerned. The resulting measurement of the cross-section is
thus much greater than that predicted by the coupled channels cal-
culation. These theoretical values have been quoted to three signi-
ficant figures, although in fact they are probably reliable only to
within ± 50%, due to uncertainties in the parameters of the nuclear
potential which are input to the programme INCH. No attempt was
made to improve this, because, as shown above, these figures are
not directly comparable with the experimental results.

Nucleus	(σ_τ) exp mb	$4\pi a_o$ mb	E_γ MeV
Mg^{24}	605 ± 15	107	$1 \cdot 37$[a]
Si^{28}	434 ± 63	$45 \cdot 1$	$1 \cdot 779$[b]
S^{32}	318 ± 36	$53 \cdot 1$	$2 \cdot 24$[b]
Ti^{48}	1039 ± 107	$31 \cdot 9$	$0 \cdot 990$[b]
Cr^{52}	1002 ± 31	$23 \cdot 2$	$1 \cdot 43$[a]
Fe^{56}	814 ± 21	$31 \cdot 4$	$0 \cdot 84$[a]

TABLE 5.9.

Experimental Values of Total Cross-section
Compared with Theoretical Predictions.

(a) = present work
(b) = Connell [17]

5.4.2. Rotational and Vibrational Models

Figure 5.17 shows the various predictions of the coupled channels

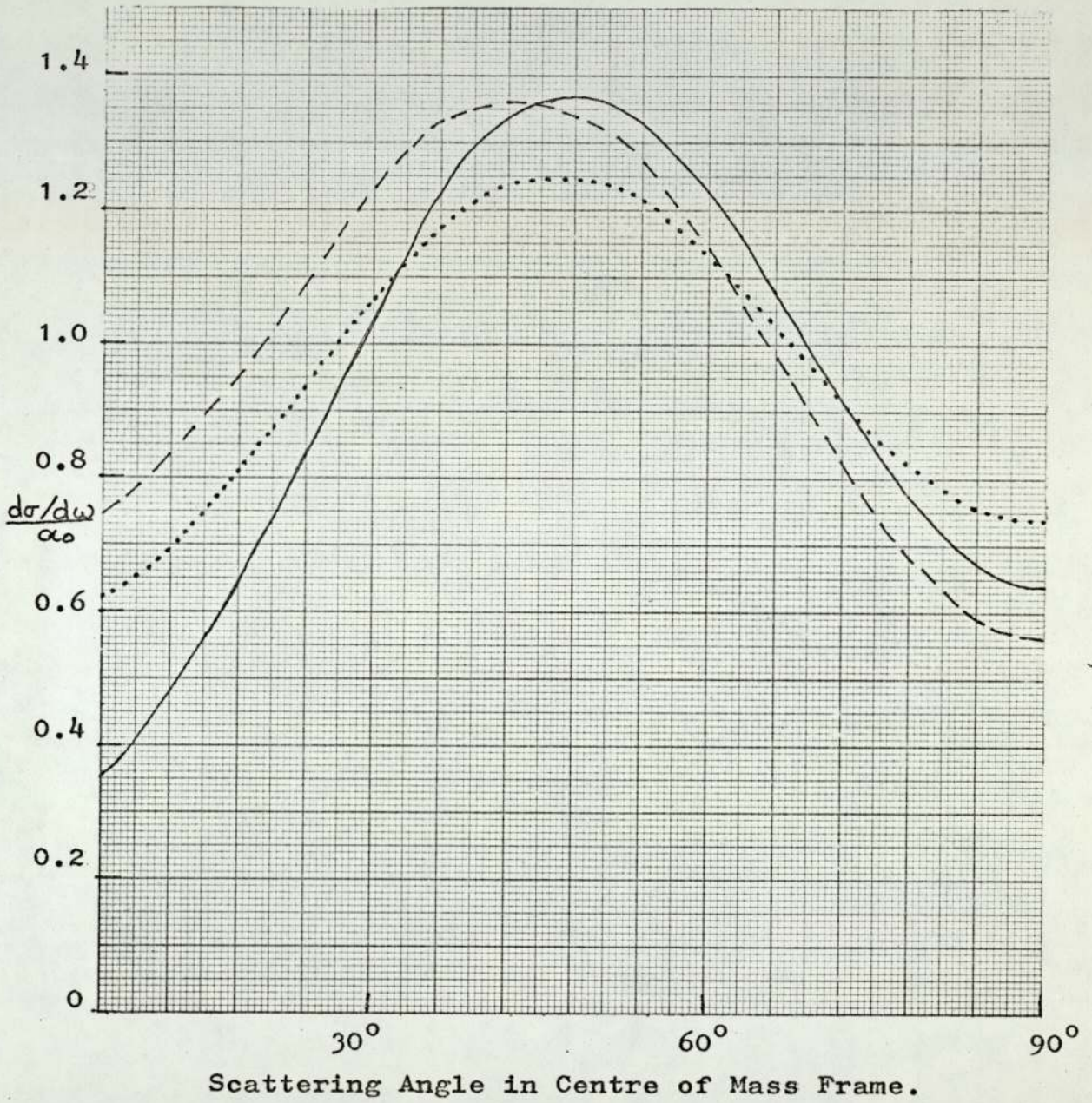Figure 5.17   Normalised Angular Distribution for the
1.37 MeV gamma-ray from Mg^{24}.

——————   Rotational model $\beta = +6.2$

— — — —   Rotational model $\beta = -6.2$

··············   Vibrational model $\beta = 0$

calculation for the cases $\beta = \pm 0 \cdot 62$ and $\beta = 0$. This latter case corresponds to a vibrational model of the nucleus, that is, it assumes the nucleus has no permanent deformation. The two former cases correspond to the rotational model with prolate and oblate deformations respectively. The results shown here are in general agreement with the results of Karban et al [9], where the predictions have been made for proton scattering on Ni^{58}. The curves are not greatly different, and, with the present experimental errors, it would not be possible to distinguish them. This is in agreement with the general finding that inelastic scattering is not very sensitive to the details of the nuclear models.

5.5. Conclusions and Suggestions for Further Work

The first part of the research project, which was to improve the performance of the experimental system, has been completed by increasing both the time and energy resolution. The result of this has been an increase in sensitivity of the system by a factor of 10, although this has to some extent been offset by deterioration in the performance of the SAMES generator. The new system has then been used to measure the differential cross-sections for the pro- duction of various gamma-rays, using natural samples of magnesium, chromium and iron.

The second part of the research project was then to use direct interaction theory, in the form of the coupled channels method, to predict these angular distributions. These predictions were then compared with the experimental data. This comparison shows that the general trends of the angular distributions are quite well predicted, dispite the fact that a significant simplification has been made, namely, that the effect of cascade from higher levels

has been neglected.

This work may be continued in one of two ways. It may be possible to redesign the system so that the angular distribution measured corresponds to that predicted theoretically. It is difficult to imagine how the system could be adapted to measure exactly the differential cross-section which is predicted by the present form of the theory. This would involve the use of many neutron detectors, surrounding the scattering sample at all angles, in an attempt to detect the inelastically scattered neutron which had excited the nucleus to the first excited state. The energy of this neutron is well defined, being the difference between the incident neutron energy and the excitation energy of the first level, so if it were detected, a time of flight system, with the good time resolution which is available with the plastic scintillators used for neutron detection, would enable this neutron energy to be selected accurately. However, the difficulty arises in detecting every neutron which excites the first level; as these neutrons may scatter into any angle, including backwards into the incident beam, and into the gamma-ray detector, it seems impossible, from the geometry of the situation, to detect all, or even a representative fraction of them.

A more conventional angular correlation technique using one neutron detector and one gamma-ray detector, might be used to measure the correlations between neutrons of the required energy, scattered through an angle θ_n, and the corresponding gamma-rays scattered through an angle θ_γ. These two angles do not necessarily have to be in the same plane. This correlation function may easily be predicted by the present theoretical technique; it is only

necessary to omit the averaging over the neutron angle of scattering, and express explicitly the dependence on this angle. The problem here is one of low count rate, which would make the experimental measurements extremely tedious, if not impossible. Currently available neutron detectors of the plastic scintillator type have an efficiency of about 10% [99] in the range of neutron energy of interest. If both gamma-ray detector and neutron detector subtend the same solid angle at the sample, then the count rate in the relevant photopeak of the gamma-ray spectrum, P_γ, is approximately 1·4 times the count rate in the corresponding peak, P_n, in the neutron time of flight spectrum. This assumes that the differential cross-sections for the two processes are equal, which is true when averaged over all angles, but may not be true at a particular pair of angles θ_n and θ_γ. To estimate the expected count rate for correlated events, assume the gamma-ray is emitted randomly with respect to the scattered neutron direction. Then for every neutron detected, the corresponding gamma-ray will be detected with a probability $\Omega/4\pi$, where Ω is the solid angle subtended by the detector at the sample. The correlation count rate is then;

$$W(\theta_n, \theta_\gamma) = P_n\, P_\gamma\, \frac{\Omega}{4\pi} \qquad\qquad ..(5.4)$$

A typical value of P_γ in the present work is $0·74\ \text{sec}^{-1}$, then;

$$W(\theta_n, \theta_\gamma) = 4·5 \times 10^{-4}\ \text{sec}^{-2}$$

Although improvements in the time resolution of the system might increase this a little, the only way to achieve a significant improvement in this count rate is to increase the strength of the neutron source by a factor of about 30. This would increase the

correlation count rate by about 10^3 as the source strength is a factor in both P_γ and P_n. The SAMES generator cannot be modified to produce this increased output, so this correlation technique is unlikely to be successful with the present facilities. This type of experiment might, however, be successfully carried out using the Dynamitron accelerator facility at the Radiation Centre, University of Birmingham.

The other approach to the continuation of this work is to seek to extend the coupled channels calculation to include a larger number of the levels of the nucleus which are excited by neutron inelastic scattering. It should be possible to include those levels which are identifiable as members of a rotational or vibrational band, based on the ground state, or on some higher level. But this approach is limited to the lower levels, for as higher excitations are reached, the classification of levels into the various bands becomes very uncertain, and it becomes clear that the nuclear potential is no longer well represented by these simplified models. Thus the matrix elements of the interactions, between the various excited states, which are required as input to INCH, cannot be calculated.

Perhaps the most promising method would be a combination of the two approaches mentioned above. Extending the coupled channels calculation to include the next two or three levels of the nucleus could probably be achieved without distorting interactions posing a serious problem. This would lead to the prediction of the correlation function between neutrons of various energies (scattered off one of several levels), and gamma-rays, also of various energies, but always including that corresponding to the transition from the

first excited state to the ground state, produced either directly or in cascade. Such experimental data would, however, be extremely complex, and ambiguities might arise in the analysis of it.

It can be seen from the above discussion that the application of direct interaction theory to the production of gamma-rays from neutron inelastic scattering is an extremely complex problem, due to the large number of states involved. However, the failure of compound nucleus theory [17], and the comparative success of an approximate method of predicting the angular distributions by direct interaction theory shown here, indicates that this approach is correct and is worth continuing further to obtain a fuller description of the inelastic scattering process.

* * * * * *

References

1. N. Bohr, Nature 137 344 (1936).

2. S. C. Mathur et al, Nuclear Physics 81 468 (1965).

3. L. Cranberg, Physical Review 159 969 (1967).

4. R. W. Benjamin et al, Nuclear Physics 79 241 (1966).

5. A. Gallmann et al, Nuclear Physics 88 654 (1966).

6. N. K. Glendenning, Physical Review 114 1297 (1959).

7. P. Marmier and E. Sheldon, Physics of Nuclei and Particles II

8. T. Tamura, Reviews of Modern Physics 37 679 (1965).

9. O. Karban et al, Nuclear Physics A147 461 (1970).

10. P. D. Greaves et al, Nuclear Physics A149 1 (1972).

11. R. L. Clarke and W. G. Cross, Nuclear Physics 53 177 (1964).

12. P. H. Stelson et al, Nuclear Physics 68 97 (1965)

13. E. Sheldon and D. M. Van Patter, Reviews of Modern Physics 38 143.

14. P. Marmier and E. Sheldon, ibid. page 1128.

15. H. Feshbach, Reviews of Modern Physics 36 1076 (1964).

16. Nuclear Structure Study with Neutrons. Int. Conf. Antwerp (1965).

17. K. A. Connell, University of Aston in Birmingham, Thesis (1972).

18. D. T. Stewart and P. W. Martin, Nuclear Physics 60 349 (1964).

19. B. A. Benetskii, Tr. Fiz. Inst. Akad Nauk. 33 123 (1965).

20. B. A. Benetskii et al, Soviet Physics JETP 18 No. 3 (1964).

21. P. W. Martin and D. T. Stewart, Journal of Nuclear Energy A/B 19 447 (1965).

22. A. P. Arya et al, Bull. Am. Phys. Soc. 12 124 (1967).

23. F. C. Engesser and W. E. Thompson, Jour. Nucl. Energy 21 487 (1967).

24. B. I. Sukhanow and N. P. Tkach, Sov. Jour. Nucl. Phys. 11 17 (1970).

25. W. M. Deuchers and D. Dandy, Proc. Phys. Soc. 75 855 (1960).

26. D. A. Gedcke and C. W. Williams, High Resolution Time Spectroscopy ORTEC report (1968).

27. D. E. Baynham, University of Aston in Birmingham, Thesis (1971).

28. J. B. Marion and F. C. Young, Nuclear Reaction Analysis (1968).

29. W. Whaling, Handbuch der Physik $\underline{34}$ 193.

30. Rosenfeld et al, UCRL-8030.

31. J. Benveniste and J. Zenger, UCRL-4266 (1954).

32. H. Argo et al, Phys. Rev. $\underline{87}$ 612 (1952).

33. J. Phillips, Phys. Rev. $\underline{90}$ 532 (1953).

34. R. Day, Phys. Rev. $\underline{102}$ 767 (1956).

35. K. Nishimura, Nucl. Phys. $\underline{70}$ 421 (1965).

36. Mullard 58AVP Photomultiplier Notes.

37. R. Post and L. Schiff, Phys. Rev. $\underline{80}$ 1113 (L) (1950).

38. E. Gatti and V. Svelto, Nucl. Inst. Meth. $\underline{43}$ 248 (1966).

39. A. Rupaal, Nucl. Inst. Meth. $\underline{49}$ 145 (1967).

40. E. Gatti and V. Svelto, Nucl. Inst. Meth. $\underline{30}$ 213 (1964).

41. J. Braunsfurth and H. Körner, Nucl. Inst. Meth. $\underline{34}$ 202 (1965).

42. R.C.A. Photomultiplier Manual PT-61.

43. Mullard 58AVP Photomultiplier Specifications (1970).

44. Morton, Nucleonics $\underline{10}$ No. 2 39 (1952).

45. E. Gatti and V. Svelto, Nucl. Inst. Meth. $\underline{4}$ 189 (1959).

46. W. McDonald and D. Gedcke, Nucl. Inst. Meth. $\underline{55}$ 1 (1967).

47. Present et al, Nucl. Inst. Meth. $\underline{31}$ 71 (1964).

48. Schwarzschild, Nucl. Inst. Meth. $\underline{21}$ 1 (1963).

49. Hyman, Rev. Sci. Inst. $\underline{36}$ (2) 193 (1965).

50. W. Burcham, Nuclear Physics - an Introduction (1963) Longmans.

51. Nuclear Enterprises Catalogue.

52. Covell, Anal. Chem. $\underline{31}$ 1785 (1959).

53. G. Grodstein and J. Hubble, NSRDS-NBS-29 (1969).

54. Storm and Israel, LA-3573 (1967).

55. C. Lederer et al, Table of Isotopes 6th ed. (1968) Wiley.

56. L. Schiff, Quantum Mechanics 3rd ed. (1968) McGraw Hill.

57. W. Meyerhof, Elements of Nuclear Physics (1967) McGraw Hill.

58. U. Abbondano et al, Jour. Nucl. Energy $\underline{27}$ 227 (1973).

59. A. Messiah, Quantum Mechanics Vol II (1962) North Holland.

60. W. Tobocman, Theory of Direct Nuclear Reactions (1961) O.U.P.

61. B. Buck, Phys. Rev. 130 712 (1963).

62. A. Stamp and J. Rook, Nucl. Phys. 53 657 (1964).

63. F. Perey and G. Satchler, Phys. Lett. 5 212 (1963).

64. N. Austern, Selected Topics in Nuclear Theory I.A.E.A. (1963).

65. D. F. Jackson, Nuclear Reactions (1970) Methuen.

66. H. Ejiri, INSJ-104 Phenomenological Discussion of Energy Levels
    etc. (1967).

67. J. M. Irvine, Nuclear Structure Theory (1972) Pergamon.

68. A. Bohr, Math. Fys. Medd. 26 No. 14 (1952).

69. J. Eisenberg and W. Greiner, Nuclear Models; Nuclear Theory Vol. 1.

70. J. M. Reid, The Atomic Nucleus (1972) Penguin.

71. J. Rapaport, Nuclear Data Sheets B3-5, 6-87 (1970).

72. M. N. Rao, Nuclear Data Sheets B3-3, 4-43 (1970).

73. P. M. Endt and C. Van Der Leun, Nucl. Phys. A214 1 (1973).

74. J. Rapaport, Nuclear Data Sheets 4 351 (1970).

75. P. Hinrichsen et al, Nucl. Phys. A101 81 (1967).

76. B. Armitage et al, Nucl. Phys. A133 241 (1969).

77. J. McGrory, Phys. Lett. 21 64 (1966).

78. P. E. Hodgson, Nuclear Reactions and Nuclear Structure (1971)
    Clarendon Press.

79. Brink and Satchler, Angular Momentum.

80. A. J. Ferguson, Angular Correlation Methods in Gamma-Ray Spectro-
    scopy.

81. P. A. M. Dirac, Principles of Quantum Mechanics (1947) O.U.P.

82. F. Mandl, Quantum Mechanics 2nd ed. (1957) Butterworths.

83. A. R. Rutledge, AEC-CRP-851 (1959).

84. A. E. Litherland and A. J. Ferguson, Can. Jour. Phys. 39 788.

85. J. Lowe, private communication.

86. Bechetti and Greenlees, Phys. Rev. 182 1190 (1969).

87. J. R. Stehn et al, BNL-325 TID-4500 2nd ed. (1964).

88. Handbook of Chemistry and Physics 44th ed. (1963) Chemical Rubber
       Company.

89. K. Nyberg-Ponnert et al, Physica Scripta 4 165 (1971).

90. Bocharew and Nefedow, Sov. Jour. Nucl. Phys. 1 574.

91. AJ-AEC-13007 Annual Tech. Prog. Rep. G.F.Y. (1971).

92. W. Breunlich et al, Z. Naturforsch 26a 451 (1971).

93. B. Jönsson et al, Arkiv För Fysik 32 (20) 295 (1969).

94. Goldberg AFWG-TR-60-30 BNL 400 2nd ed. (1962).

95. Haouat et al, Comm. à l'Energie Atomique. Study of $Fe^{56}(n,n'\gamma)$
       Reaction.

96. V. M. Bezotosnyi et al, Sov. Jour. Nucl. Phys. 3 (5) 632 (1966).

97. P. W. Martin and D. T. Wtewart, Can. Jour. Phys. 46 1657 (1968).

98. Campbell, Bull. Am. Phys. Soc. 12 473.

99. D. Holland, private communication.

APPENDIX   1

```
   SUBROUTINE GAMMA(AMPRE,AMPIM,THETA)
   DIMENSION AMPRE(60),AMPIM(60),DENSRE(5,5),DENSIM(5,5)
  1,RHORE(5,5),RHOIM(5,5) ,TRE(15),TIM(15)
   DO 3 J=1,5
   DO 2 JI=1,5
   DENSRE(J,JI)=0.0
   DENSIM(J,JI)=0.0
   DO 1 I=1,4
   M=J+(I-1)*5
   N=JI+(I-1)*5
   DENSRE(J,JI)=DENSRE(J,JI)+AMPRE(M)*AMPRE(N)+AMPIM(M)*AMPIM(N)
  1 DENSIM(J,JI)=DENSIM(J,JI)+AMPIM(M)*AMPRE(N)-AMPRE(M)*AMPIM(N)
   IF(THETA.GT.11.0)  GO TO 6
   RHORE(J,JI)=0.0
   RHOIM(J,JI)=0.0
  6 RHORE(J,JI)=RHORE(J,JI)+DENSRE(J,JI)*SIN(THETA*0.0174533)
   RHOIM(J,JI)=RHOIM(J,JI)+DENSIM(J,JI)*SIN(THETA*0.0174533)
   IF(THETA.LT.179.0) GO TO 2
   RHORE(J,JI)=RHORE(J,JI)/86.0
   RHOIM(J,JI)=RHOIM(J,JI)/86.0
  2 CONTINUE
  3 CONTINUE
   IF(THETA.LT.179.0) GO TO 23
   DO 12 K=1,15
   TRE(K)=0.0
   TIM(K)=0.0
   IF (K-1) 14,14,15
 14 L=0
   M=0
   GO TO 16
 15 CONTINUE
   IF (K-6) 17,17,18
 17 L=2
   M=4-K
   GO TO16
 18 L=4
   M=11-K
 16 DO 19 J=1,5
   DO 13 JI=1,5
   TRE(K)=TRE(K)+CLEBGN(2.0,3.0-J,2.0,JI-3.0,L*1.0,M*1.0)*RHORE
  1(J,JI)*(-1)**(JI-1)
 13 TIM(K)=TIM(K)+CLEBGN(2.0,3.0-J,2.0,JI-3.0,L*1.0,M*1.0)*RHOIM
  1(J,JI)*(-1)**(JI-1)
 19 CONTINUE
 12 PRINT 21,TRE(K),TIM(K)
 21 FORMAT(' TRE=',E16.5,' TIM=',E16.5)
   AO=TRE(1)*0.177917
   A2=-TRE(4)*0.10632608
   A4=-TRE(11)*0.19020188
   PRINT 24, AO, A2, A4
 24 FORMAT(' AO=',E16.5,' A2=',E16.5,' A4=',E16.5)
 23 CONTINUE
   RETURN
   END
```